

UNIVERSIDADE DE SÃO PAULO
INSTITUTO DE FÍSICA

Simulação Monte Carlo do processo de aquisição de imagens
de um tomógrafo de dupla energia

Lorena Paola Robayo Puerto

Orientador(a): Prof. Dr. Paulo Roberto Costa

Dissertação de mestrado apresentada ao Instituto
de Física como requisito parcial para a obtenção do
título de Mestre em Ciências.

Banca Examinadora:
Prof. Dr. Paulo Roberto Costa (IFUSP)
Prof. Dr. Sérgio Shiguemi Furuie (Poli USP)
Prof. Dra. Ana Maria Marques da Silva (PUCRS)

São Paulo

2018

FICHA CATALOGRÁFICA
Preparada pelo Serviço de Biblioteca e Informação
do Instituto de Física da Universidade de São Paulo

Robayo Puerto, Lorena Paola

Simulação Monte Carlo do processo de aquisição de imagens de um tomógrafo de dupla energia. São Paulo, 2018.

Dissertação (Mestrado) – Universidade de São Paulo. Instituto de Física. Depto. de Física Nuclear

Orientador: Prof. Dr. Paulo Roberto Costa
Área de Concentração: Física Nuclear.

Unitermos: 1. Tomografia computadorizada por raios X; 2. Tomografia de dupla energia; 3. Decomposição baseada nas projeções; 4. Imagens de concentração de material; 5. Imagens monoenergéticas.

USP/IF/SBI-045/2018

UNIVERSITY OF SÃO PAULO

Institute of physics

**Monte Carlo Simulation of the Image Acquisition process of a
Dual Energy Computed Tomography Device**

Lorena Paola Robayo Puerto

Advisor: Prof. Dr Paulo Roberto Costa

Dissertation submitted to the Institute of Physics of
the University of São Paulo in partial fulfilment of the
requirements for the degree of Master of Science.

Examination Committee:

Prof. Dr. Paulo Roberto Costa (IFUSP)

Prof. Dr. Sérgio Shiguemi Furuie (Poli USP)

Prof. Dr. Ana Maria Marques da Silva (PUCRS)

São Paulo

2018

Acknowledgments

I want to thank Paulo Costa my advisor for given me the opportunity to work in an amazing group, for all the corrections of this text and for being so patient with me during these years. I want to thank Denise for the idea of my master project, and for the support and kindness during the clinical measurements. I would like to thank the professors and members of the Radiation Dosimetry and Medical Physics Group for all the affection and so many good moments we shared.

I want to thank CNPq for the financial support, under the project 155106/2015–5. I also thank the InRad for the possibility of making the measurements in the device Discovery CT 750 HD in the mark of the project 099/2017.

I really thank Chico and Nancy for the support in technical aspects and for the gentleness. I would like to thank Marcos and the staff of the mechanical workshop that always helped me confectioining the pieces I needed. I thank Fábio Pádoa for the constant support with the server usage and the repair of my computer. I thank the secretaries of the nuclear department for being so sympathetic and attentive.

I really thank the professors of the Institute of physics for their dedication and quality teaching. I especially thank Professor Vito Vanin for his excellent course of Statistical analysis of data for experimental physics. I am grateful to professor José M. Fernández-Varea for taking the time to help me solve my doubts about PENELOPE, for the kindness and motivation he gave me during the realization of the present work.

I am very grateful to Alejandro Lopez for helping me so much and for all the conversations we had about PENELOPE which led me to a deeper comprehension of the code and the possibilities of it. I am also grateful to Leandro Mariano for the all the support he gave me with Matlab®, which helped me so much. I thank Audrew Frimaio and Denise for providing me the materials to prepare the physical phantom.

I want to thank the friends I made during this master for so many great moments. Alejandro, Carlos, Louise and Josilene thanks for all the good moments, jokes laughs and love. I thank Eduardo for the patience and for all the support he gave me during the last months, when things seemed difficult.

I thank all my friends who always cheered me, especially Loren for following closely my process. I really thank my family that always encourages me to follow my dreams and gives the support I need. I thank my little brother for showing me all single detail of his stuff and paintings, and for sharing so in spite of the distance, it really helped me to feel closer to him.

RESUMO

A Tomografia Computadorizada de Energia Dupla (DECT em inglês) é um dos campos das imagens tomográficas que mais evoluiu nos últimos anos. O DECT usa dois espectros para irradiar pacientes e é capaz de diferenciar tecidos com base na sua composição elementar. Apesar de serem semelhantes aos dispositivos padrão de tomografia, para essa modalidade é necessário o desenvolvimento de ferramentas específicas que permitam o estudo de suas propriedades de imagem. O objetivo deste trabalho era construir um sistema simulado de Tomografia Computadorizada (TC) com a capacidade de produzir imagens semelhantes às obtidas em dispositivos DECT reais. O TC simulado também permitiria explorar as propriedades das imagens de materiais de teste antes de sua construção física. Este trabalho apresenta a simulação do processo de aquisição de imagens de um dispositivo DECT que funciona a partir da troca rápida de kV, o GE Discovery CT 750 HD. A geometria simulada foi baseada num dispositivo atualmente disponível no InRad (Instituto de Radiologia da Faculdade de Medicina da Universidade de São Paulo). As simulações foram realizadas usando o código Monte Carlo PENELOPE/penEasy para simular o transporte de radiação através dos materiais e detectores. Também é apresentada uma comparação entre as imagens obtidas no dispositivo real e nas simulações. Para isso, foi preparado um objeto simulador cilíndrico contendo concentrações de materiais equivalentes a iodo e cálcio. As imagens de tal objeto simulador foram adquiridas no equipamento GE Discovery CT 750 HD. Um objeto simulador equivalente foi modelado e as suas imagens foram simuladas com o código PENELOPE/penEasy. As imagens foram adquiridas e reconstruídas de acordo com as possibilidades do equipamento clínico de tomografia. Imagens de concentração de material e imagens monoenergéticas foram obtidas a partir do dispositivo CT clínico e das simulações. O algoritmo BMD (Basis Material Decomposition em Inglês) baseado nas projeções foi implementado usando os coeficientes de atenuação mássicos da água e do iodo. Consequentemente, imagens de concentração dos materiais água e iodo foram obtidas. A concentração medida nos cilindros de iodo foi equivalente às esperadas tanto no dispositivo real quanto nas imagens simuladas. Foram observados artefatos de endurecimento de feixe nas imagens de concentração de material. Imagens monoenergéticas foram obtidas para diferentes energias. Tais imagens foram obtidas a partir da superposição das imagens de concentração de água e iodo, que foram ponderadas pelos seus respectivos coeficientes de atenuação mássicos. Verificou-se que para as imagens monoenergéticas simuladas e reais em altas energias a imagem de concentração da água é a componente dominante, produzindo imagens que apresentaram as cavidades de iodo como menos atenuantes do que a água. Por outro lado, para energias baixas, a componente dominante nas imagens monoenergéticas foi a imagem de concentração do iodo. O CNR foi analisado nas imagens monoenergéticas como função da energia. As curvas do CNR dos dispositivos simulado e real exibiram semelhanças em sua forma, mas com escala diferente devido à diferença no ruído. Foi possível concluir que o modelo DECT simulado apresenta resultados qualitativos semelhantes aos obtidos no dispositivo real. O sistema de TC simulado permite explorar as características das imagens com diferentes materiais e composições. Ele também pode ser usado como uma ferramenta didática para melhorar a compreensão da diferenciação de materiais em tomografia espectral e DECT.

Palavras-chave: Tomografia Computadorizada de Dupla Energia; decomposição baseada nas projeções; imagens de concentração de material; imagens monoenergéticas

ABSTRACT

Dual Energy (DE) Computed Tomography (CT) is one of the fields of tomographic images that has evolved rapidly during the last years. DECT uses two X-ray spectra to irradiate patients. It is capable to differentiate materials based on its elementary composition. Despite being similar to standard CT devices, DECT devices require the development of specific tools that allow the study of their image properties. The objective of this work was to build a modelled CT system capable of producing images similar to those obtained in real DECT devices. The modelled CT would also allow exploring the image properties of test materials before their physical construction. This work presents the simulation of the acquisition process of a DECT device that works with rapid kV switching, the GE Discovery CT 750 HD. The simulated geometry was based on a device currently available at the InRad (Institute of Radiology of the Faculty of Medicine of the University of São Paulo). The simulations were carried out using the PENELOPE/penEasy Monte Carlo code, which simulates radiation transport through the materials and detectors. A comparison between the images obtained in the real device and from simulations is also presented. To do so, a real phantom was prepared to be imaged and an equivalent system was simulated. The phantom contained inserts with concentrations of iodine and calcium. The images were acquired and reconstructed according to the possibilities of the real CT device. Standard, material concentration and virtual monoenergetic images were acquired from both, the real CT device and simulations. The Projection-Based BMD method was implemented using the mass attenuation coefficients of water and iodine. Then, material concentration images of water and iodine were obtained. The iodine concentrations estimated from the images agreed with the expected values in both real device and simulated images. Beam hardening artefacts were observed in the simulated material concentration images. Monoenergetic images were obtained for different energies. Such images were obtained as a superposition of the concentration images of water and iodine, weighed by their respective mass attenuation coefficient. It was verified that in the simulated and real device images, at high energies, the water concentration image predominated in the monoenergetic images, producing images that presented the iodine cavities as less attenuating than water. In contrast, at low energies, the predominant component of the monoenergetic images was the iodine concentration image. Contrast Noise Ratio (CNR) was analysed in the monochromatic images as a function of energy. Simulated and real device CNR curves exhibited similarities in their shape but with a different scale due to their difference in noise. It was possible to conclude that the simulated DECT model presented qualitative results similar to the obtained in the real device. The modelled CT system permits exploring the image features with different materials and compositions. It could also be used as a didactic tool to improve the understanding of material differentiation in spectral or DECT.

Keywords: Dual Energy Computed Tomography, Basis Material Decomposition (BMD); Projection-Based decomposition; material concentration images; monoenergetic images

LIST OF TABLES

Table 1. Main historical events of the early CT systems. Table adapted from Kalender (Kalender, 2011)	4
Table 2. Summary of the principal features of each Dual and Spectral Energy CT device, described in this section (McCollough, 2015).	26
Table 3. Main features of the servers available in the Group of Radiation Dosimetry and Medical Physics of the University of São Paulo.	34
Table 4. Characteristics of the GE Discovery CT 750 HD device (GE Company, 2015), and the modelled CT.	35
Table 5. Features of the used spectra, such spectra are used as input for the simulations.	38
Table 6. Parameters obtained from the calibration of the HU using the phantom Catphan 600.	43
Table 7. Chemical features of the dilutions contained in the simulated phantom of Figure 27.	44
Table 8. Material density and element concentration of the phantom cylinders. The Labels presented coincide with the ones shown in Figure 29. The Short Name column presents the names used for future reference.	46
Table 9. $CTDI_{100,c}/CTDI_{100,p}$ ratios resulting from the present simulations for 80, 100, 120 and 140 kV, ratios obtained by Kramer et al. (Kramer et al., 2017) and the percentage differences of both.	51
Table 10. Measured mean HU for the standard images obtained from both simulations and real device images, and t and t_{crit} to compare the values.	58
Table 11. Measured effective iodine concentration in the inserts of the iodine concentration images of Figure 42 and Figure 43. The expected concentration coincides with the “Concentration” column in Table 8. The t -values (Appendix C) were computed comparing the Real and Simulated concentrations with the expected values. The uncertainty of the expected values was considered in the t -values calculation.	62

LIST OF FIGURES

Figure 1. Simplified scheme of the measurement process for a fan-beam CT. The attenuation profile is generated from the intensity profile. Figure adapted from Kalender (Kalender, 2011).	5
--	---

Figure 2. Schematic representation of an X-ray tube. The cathode filament is heated to approximately 2400 K. The electrons escape from the filament and are accelerated by the electric field between the cathode and anode. Reaching the anode, the electrons interact with the anode material generating a cone-shaped X-ray beam. Figure adapted from Buzug (Buzug, 2008).....6

Figure 3. a.) Diagram of the events for production of the *bremstrahlung* radiation. The process 1 represents a frontal collision, which generates the photons with maximum energy. Processes 2 and 3 present the dependence of the interaction with distance. The farther the electron passes from the nucleus, the weaker the interaction and energy of the emitted photons. b.) Diagram of the emission of characteristic radiation. First (1) the incident electron interacts with the K-shell electron and a vacancy is created (2). Then an electron from an external shell occupies the vacancy (3) and a characteristic photon is emitted (4). Figures adapted from Bushberg et al. (Bushberg et al., 2011).....7

Figure 4. Normalized spectrum obtained with 80 kV and filtration of 6 mm Al. The continuous component corresponds to the *bremstrahlung* radiation. The sharp peaks present the different characteristic transitions that take place in tungsten when the tube voltage is 80 kV. The anode angle was 10, the spectrum was generated using the modified TBC model (P. Costa et al., 2007).7

Figure 5. Principal components of the scanning geometry of a CT. The dimensions shown are in mm. Figure adapted from Kalender (Kalender, 2011).8

Figure 6. Geometric arrangement of the detectors in a CT. It is possible to see how the detector blocks are positioned in the angular direction, the figure also presents a photograph of a detector element with its electronic module. Figure adapted from Bushberg et al. (Bushberg et al., 2011).....9

Figure 7. Representation of the image reconstruction via *Backprojection*. Different results are obtained using the a) simple *Backprojection* and b) the Filtered *Backprojection*. Figure adapted from Oppelt and Kalender (Oppelt, 2005; Kalender, 2011)..... 12

Figure 8. Graphs of the Ramp, Shepp-Logan, Hamming and Hann filters. Figure adapted from Demirkaya et al. (Demirkaya, 2008)..... 13

Figure 9. Usual CT values for various body tissues. Figure adapted from Kalender (Kalender, 2011). 14

Figure 10. Example of regions and sizes usually used to measure the CNR and the SNR. Figure adapted from Bushberg et al. (Bushberg et al., 2011)..... 15

Figure 11. DECT images with material decomposition confirm the presence of monosodium urate (MSU) in green, in the knee region. Figure adapted from Nicolaou et al. (Nicolaou et al.2011)..... 16

Figure 12. Mass attenuation coefficient as a function of incident photon energy for water and bone. The vertical dotted section represents the energy range of X-rays for diagnostic radiology. Figure adapted from Buzug (Buzug, 2008).	19
Figure 13. Schematic configurations of Spectral and Dual Energy CT devices. a.) Sequential acquisition CT. b.) Dual Source CT. c.) Tube kV Switching CT. d.) Dual Layer CT. e.) Photon Counting CT. Adapted from Heismann et al. (Heismann et al., 2012).....	20
Figure 14. Example of the X-ray spectra that can be used in Dual Source CT with the two tubes running at 80 and 140 kV. The 140 kV spectrum is acquired with an additional filter which reduces the overlap of the spectra. It is also possible to increase the mAs of the low energy spectrum, corresponding to 80 kV, which in this case, is the double of the other. Spectra obtained using the modified TBC model (P. Costa et al., 2007).....	21
Figure 15. Spectra obtained for 80 and 140 kV. Spectra generated using 2 mAs and the same filter of 4mm Al. Spectra obtained using the modified TBC model (P. Costa et al., 2007).....	22
Figure 16. Scheme of the operation mode of the Discovery CT 750 HD. Red arrows represent the reconstructions sequence. The interleaved sinogram is split in the projections corresponding to each kV. From such projections, standard images can be reconstructed. Projections of materials of interest as iodine and water are also obtained performing the Projection-Based BMD on the standard sinograms. From these material projections, material concentration images can be reconstructed. Finally, virtual monoenergetic images can be obtained from the material concentration images. Figure adapted from Chandra & Langan (Chandra & Langan, 2011).....	23
Figure 17 Schematic representation of the dual layer detector system (few elements shown). There are shown the two photodiodes of each pair of detectors. Figure adapted from Vlassenbroek (Vlassenbroek, 2011).	24
Figure 18. Sensitivity spectra of the two layers, the considerable overlap limits spectral contrast. Figure adapted from Johnson and Kalender (Johnson & Kalender, 2011).....	25
Figure 19. Scheme representing the sections of this chapter, the objectives and main methods implemented in each section. Sections 2.1 and 2.2 present the methodology of the simulations performed. The only section that presents the methodology concerning measurements in a real CT device and simulations is the 2.3. Section 2.4, explains the exhibition units and intervals of the images presented in this work.....	31
Figure 20. Summarized image reconstruction processes of the images used in the present work. The name of the images and sinograms obtained after each reconstruction are presented inside the green boxes. Detailed information about the	

acquisition process and reconstruction is found in section 1.3 and in Figure 16. Almost all the scheme is referred to the Projection-Based BMD of section 1.3.1. The box enclosed by the discontinuous red line represents processes correspondent to the Image-Based BMD of section 1.3.2.....32

Figure 21. Schematic representation of the simulation process using PENELOPE/penEasy.....33

Figure 22. Scheme of the components of the modelled CT device, (1) depicts the elements of the source before the phase space plane (2) depicts the imaged object and the detector array.....35

Figure 23. Measured spectrum and spectrum obtained using the modified TBC model for a tube voltage of 140 kV. The measured spectra were available thanks to the courtesy of Dr. Ricardo Terini.38

Figure 24. Design of the simulated bowtie filter, all the presented dimensions are in millimetres. The simulated bowtie filter material was aluminium.....39

Figure 25. Representation of the geometric arrange used to study how the bowtie filter affects the energy deposited in the detectors. The energy deposited in the detectors belonging to the phantom shadow was analysed while the bowtie filter position was varied, especially the energy deposited of the outer or most external detectors (red arrow). The angle of the detector is measured with respect to the central line that passes through the centre of the detector arrangement. The green lines present the angle of a specific detector. This figure presents just the phantom and the detectors, the entire geometric model is found in Figure 22.40

Figure 26 (a) CTDI cylindrical phantom used to compute the $CTDI_{100,c}$ at the centre and $CTDI_{100,p}$ at the 4 positions at 1 cm from the surface; (b) 3D view showing the cylindrical bodies with 10 cm length and 8 mm of diameter used to compute the CTDI.....40

Figure 27. Representation of the iodine distribution in the water phantom, water is placed in the blue region and the iodine concentrations in the green ones. Three concentrations of iodine were simulated, I-45 mg/cm³, I-30 mg/cm³ and I-15 mg/cm³ and two cylinder sizes, 1 and 2 cm diameter.43

Figure 28. Left: Real device with the phantom positioned in the centre on the gantry CT. Right: modelled CT system.....45

Figure 29. Real phantom (Costa, 1993) and its equivalent simulated phantom. The inserts are placed in a water phantom. The labels A-F represent each material and its composition as in Table 8.45

Figure 30. Acquisition modes and type of images acquired in the GE Discovery CT 750 HD. For the Monoenergetic and the Material images, the pairs of materials between parentheses represent the materials used to perform the BMD method.....47

Figure 31. Representation of the regions of interest used to measure the mean value and standard deviation on both simulated and real images. Material labels A-F are shown as well as the region defined for water.....48

Figure 32. **a.)** Energy deposited in the detectors as a function of the fan angle (Figure 25). The energy deposited is obtained for different bowtie filter positions (1 cm, 3 cm, 5 cm, and 7 cm) and without a filter. **b.)** Response of the three most external detectors for each bowtie filter position (1 to 15 cm), the no-filter data is plotted at 0 cm position.....50

Figure 33. Sinograms obtained for an angular step of 1 degree and for both 80 kV and 140 kV spectra. The curves corresponding to each iodine insert are visible.52

Figure 34. Standard images reconstructed for the 80 and 140 kV spectra. Beam hardening artefacts are present in both images, especially in the image of 80 kV. Image size: 160x160 pixels. L/W: 650 HU/1850 HU. On the left, the representation of the phantom and its iodine concentrations is reprinted from Figure 27.53

Figure 35. Material sinograms for water and iodine reconstructed from the 80 and 140 kV projections (Figure 33). The material sinograms were obtained following the theory presented in the section 1.3.1.54

Figure 36. Reconstructed concentration images for water (L/W 0.82 mg cm⁻³/ 0.37 g cm⁻³) and iodine (L/W 23 mg cm⁻³/42 mg cm⁻³) using the Projection-Based BMD. On the left, the representation of the phantom and its iodine concentrations is reprinted from Figure 27.54

Figure 37. Reconstructed material concentration images of water (L/W: 0.94 g cm⁻³/ 0.09 g cm⁻³) and iodine (L/W: 26 mg cm⁻³/ 25 g cm⁻³). The images were generated using the Image-Based BMD method. On the left, the representation of the phantom and its iodine concentrations is reprinted from Figure 27.55

Figure 38. Reconstructed monoenergetic images for 48 keV (L/W: 500 HU/2000 HU), 62 keV (L/W: 0 HU/1500 HU), 80 keV (L/W: -250 HU/1250 HU) and 140 keV (L/W: -500 HU/1000 HU). Images obtained using the Projection-Based BMD method. On the left, the representation of the phantom and its iodine concentrations (Ultravist®) is reprinted from Figure 27.56

Figure 39. Standard images obtained with the real CT scanner, the images were obtained in axial mode with a slice thickness of 5 mm. The images were obtained with the same exposition 270 mAs. The image size is 512x512 pixels, L/W: 596 HU/2002 HU. On the left, the representation of the inserts and material concentrations is reprinted from Figure 29.57

Figure 40. Simulated standard images for 80 kV and 140 kV spectra (L/W: 596 HU/2002 HU). The beam hardening artefacts in the 80 kV image of the two

highest concentrations of iodine are smooth but perceptible. On the left, the representation of the inserts and material concentrations is reprinted from Figure 29. 58

Figure 41. Regions inside the images corresponding to the four slices at 140 kV, the inserts represented are the A, C and D. The variation in the grey level of the insert D among the slices is appreciable. The grey level of the insert C, which contains iodine, is less variable among the slices. L/W: 1300 HU / 2100 HU..... 59

Figure 42. Material concentration images obtained from the real device. The decomposed materials were water (L/W: 966 mg cm⁻³/313 mg cm⁻³) and iodine (L/W: 128 mg cm⁻³/306 mg cm⁻³). On the left, the representation of the inserts and material concentrations is reprinted from Figure 29. 60

Figure 43. Material concentration images obtained from the simulations for water (L/W: 0.925 g cm⁻³/ 0.275 g cm⁻³) and iodine (L/W: 23 mg cm⁻³/ 43 mg cm⁻³). On the left, the representation of the inserts and material concentrations is reprinted from Figure 29..... 61

Figure 44. Material concentration images obtained from the real device. The decomposed materials were water (L/W: 966 mg cm⁻³/313 mg cm⁻³) and calcium (L/W: 208 mg cm⁻³/ 518 mg cm⁻³). On the left, the representation of the inserts and material concentrations is reprinted from Figure 29. 64

Figure 45. Material concentration images obtained from the simulations. The decomposed materials were water (L/W: 0.94 g cm⁻³/0.14g cm⁻³) and calcium (L/W: 27 mg cm⁻³/ 27 mg cm⁻³). On the left, the representation of the inserts and material concentrations is reprinted from Figure 29. 64

Figure 46. Monoenergetic images for 70, 80 and 140 keV (L/W: 594 HU/2005 HU). The images were obtained using the real device. The images were reconstructed using the Projection-Based BMD method, for the materials water and iodine. On the left, the representation of the inserts and material concentration distributed in the phantom is reprinted from Figure 29. 66

Figure 47. Monoenergetic images for 48 keV (L/W: 1000 HU/3000 HU), 62 keV (L/W: -655 HU/2345 HU), 70 keV (L/W: -1150 HU/2350 HU), 80 keV (L/W: -930 HU/3070 HU) and 140 keV (L/W: -932 HU/5060 HU). The images were obtained from simulations and reconstructed using the Projection-Based BMD method. On the left, the representation of the inserts and material concentration is reprinted from Figure 29. 67

Figure 48. CNR as a function of the energy of the virtual monochromatic images obtained from the real device..... 69

Figure 49. CNR as a function of the energy of the virtual monochromatic images obtained from simulations..... 69

ACRONYMS

BMD – Basis Material Decomposition

CNR – Contrast to Noise Ratio

CT – Computed Tomography

DECT – Dual Energy Computed Tomography

FBP – Filtered BackProjection

FOV – Field Of View

GE – General Electric

HU – Hounsfield units

InRad – Institute of Radiology of the University of São Paulo

MRI – Magnetic Resonance Imaging

M.Sc. – Master of Science

NIST – National Institute of Standards and Technology

PET – Positron Emission Tomography

PMMA – Poly (Methyl Methacrylate)

QA – Quality Assurance

SNR – Signal to Noise Ratio

SPECT – Single Photon Emission Tomography

SUMMARY

Resumo.....	iii
Abstract	iv
List of Tables	v
List of Figures	v
Acronyms	xi
Introduction	1
1 Theory.....	4
1.1 Computed tomography basic principles	4
1.1.1 Characteristics of the radiation	5
1.1.2 Scanning geometry	8
1.1.3 Filtered Backprojection (FBP).....	9
1.1.4 Hounsfield units (HU)	13
1.1.5 Image quality parameters.....	14
1.2 Dual Energy Computed Tomography	15
1.2.1 Basic principles of DECT	17
1.2.2 Devices for Spectral CT and DECT	19
1.3 DECT Algorithms	27
1.3.1 Projection-Based BMD	28
1.3.2 Image-Based BMD	29
1.3.3 Density and Atomic Number Reconstruction	29
2 Materials and Methods.....	31
2.1 Modelled CT system.....	34
2.1.1 Source Model	36
2.1.2 Acquisition of the projections.....	41
2.2 Water-Iodine phantom.....	43
2.3 Real phantom comparison.....	44
2.3.1 Features of the acquired images.....	46
2.4 Image display options.....	47
3 Results and Discussions.....	49

3.1	Modelled CT geometry	49
3.2	Simulations using the water-iodine phantom.....	52
3.2.1	Projection-Based BMD	53
3.2.2	Image-Based BMD.....	54
3.2.3	Monoenergetic images.....	55
3.3	Real phantom comparison.....	57
3.3.1	Standard images	57
3.3.2	Material concentration Images	60
3.3.3	Monoenergetic images.....	65
4	Conclusions.....	71
	References	74
	Appendixes.....	79
A.	CT image characterization.....	79
A.1	Methodology	79
A.1.1	Reconstructed images of bone and water	81
A.2	Results	81
A.2.1	Characterization of CT images: Contrast and Noise	81
A.2.2	Reconstructed images of bone and water	87
A.3	Uncertainties of CNR and SNR.....	91
B.	Chemical features of the simulated materials.....	92
B.1	Simulated water-iodine phantom	92
B.2	Real phantom.....	94
C.	T-test.....	96
D.	Monoenergetic images.....	98

INTRODUCTION

Medical X-ray imaging started with the discovery of the X-rays in 1895, by Conrad Roentgen. For this discovery, he received the Nobel Prize in 1901. X-rays are the basis of imaging techniques such as radiography, fluoroscopy, mammography, angiography and Computed Tomography (CT) (Bradley, 2008). In the last years, Dual Energy Computed Tomography (DECT) has been introduced to clinical practice.

Even though the potential of the dual energy methods is known since the decade of the 70s, their capabilities were not available in the first-generation clinical devices (Marin, 2014). Nowadays, DECT technology enables the use of the advantages of this imaging modality without image quality loss or increase of absorbed dose. There are three different architectures of DECT machines that have been implemented in clinical practice: dual source CT, dual-layer detector CT, and rapid kV switching CT.

The main difference between standard CT with DECT is the use of two X-ray spectra obtained at different tube voltages. The use of two radiation spectra allows the decomposition of two properties of the materials. Depending on the approach used, it is possible to estimate material concentration, density and atomic number (Heismann et al., 2012). Virtual monoenergetic images are also generated by DECT methods. The virtual monoenergetic images are used to improve the structure attenuation compared to standard CT images. Schneider et al. (Schneider et al., 2014) performed a DECT angiography comparison of the image quality of head and neck vessels. They found that monoenergetic images at the optimal energy provide better vessel attenuation and Contrast to Noise Ratio (CNR) compared to 120 kV polyenergetic images.

The American Association of Physicists in Medicine (AAPM) presented, in its 1977 report concerning the use of phantoms for QA(Quality Assurance) for standard CT (AAPM, 1977), that the increase in the utilization of a specified device requires the definition of specific tests to ensure its correct performance. The standard CT quality is evaluated by measuring different properties in phantoms. The use of phantoms attempts to quantify properties like noise, spatial resolution, patient dose, artefacts and linearity, among others (AAPM, 1977, 2008, 2011, 2014; Vieira, 2016)

Despite being similar to a standard CT machine, DECT devices required the development of specific tools which allow the study of the image properties of this CT modality. There are different approaches of DECT phantoms currently available (Gammex, 2015, 2017). Such phantoms present materials with specific concentrations of iodine, calcium, blood, adipose tissue and other materials.

On the other hand, Monte Carlo Simulation has been constantly used in Medical Physics. For instance, Monte Carlo methods have been used as a tool for the simulation of radiation dose in radiotherapy treatment planning using CT images (Verhaegen, 2005; Fu, 2017; Sarrut, 2016). In radiology, Monte Carlo has also been used in diverse studies such as the simulation of a X-ray tube (Bazalova, 2007). A great amount of studies in radiology are focused in CT dose estimations (Sechopoulos, 2008; Ferreira, 2010; McMillan, 2016; Ming, 2017; Kramer, 2017). Landry et al. modelled a Dual Source CT and simulated the acquisition of its images (Landry, 2011), etc. In this Master project, the rapid kVp switching device was modelled and images of various phantoms were simulated.

The main objective of this M.Sc. work was to build a modelled CT system with the capability of simulate images similar to those obtained in real DECT devices. The modelled CT would allow exploring the image properties of test materials before its physical construction.

The specific objectives of the present work were to:

- Construct a modelled CT similar to the real device;
- Validate image properties and image quality parameters;
- Explore material differentiation properties of the DECT methods;
- Characterize properties of the simulated material concentration and virtual monoenergetic images
- Compare the images acquired using the modelled CT and the real device.

The present work is organized into four chapters as follows:

Chapter 1 presents the theory of standard CT and DECT. It starts with a brief description of the standard CT and the main concepts necessary for this work. Section 1.2 presents the physical principles necessary to understand the DECT. The specific devices that use DECT or spectral CT features are also shown in section 1.2. The mathematics and main features of the DECT reconstruction algorithms are presented in 1.3.

Chapter 2 describes the methodology and specifications of the simulations and measurements that took place during the development of this work. In section 2.1, the main features used for the CT simulation are presented. The geometry of the phantom containing iodine concentrations and the methods used to analyse its images are presented in section 2.2. Section 2.3 presents the features of the real and simulated phantoms that were used for the comparison between images of the actual device and

the simulations. Section 2.4 explains the units used in this work when displaying the images.

Chapter 3 presents the results and discussion of the present study: Modelled CT system (section 3.1), Simulations using the water–iodine phantom (section 3.2) and the comparison between the results obtained with the real and simulated phantom (section 3.3).

Chapter 4 presents the conclusions of the present work and possible future studies. This chapter contains a summary of the results obtained in the characterization of the CT device, the simulation of CT images, and the comparison of simulated and real images.

1 THEORY

This chapter presents the basic principles underlying the Dual Energy and Standard Computed Tomography (DECT) methods. Section 1.1 presents a general description of the standard Computed Tomography technology and some basic concepts necessary to understand the present work. Section 1.2 introduces the basic principles that made feasible the DECT as well as the devices which incorporate this technology. The mathematical formulation of the DECT methods is outlined in section 1.3.

1.1 Computed tomography basic principles

X-ray computed tomography is an imaging modality based on the measurement of the attenuation profiles of X-rays which cross an object or patient. As its name indicates, computed tomography requires computer processing. In fact, the improvement of computer technology made this imaging modality possible. It also required the development of specific mathematical and physical tools for the acquisition and reconstruction processes. Table 1 summarizes the main historical events that conducted to the development of clinical CT devices. A large number of technical and technological advances in CT have been implemented since 1972, such as different acquisition modes, detector arrangement, source operation, reconstruction algorithms, etc. (Bushberg et al., 2011; Buzug, 2008; Kalender, 2011).

Table 1. Main historical events of the early CT systems. Table adapted from Kalender (Kalender, 2011)

Year	Event
1895	W.C. Roentgen discovers the X-rays
1917	J. H. Radon develops the mathematical fundamentals of the reconstruction algorithm for cross-sectional images from transmission measurements.
1963	Description of a technique for calculating the absorption distribution in the human body by A.M. Cormack.
1972	Conduction of the first clinical CT examinations by G.N. Hounsfield and J. Ambrose.
1975	Introduction of the first whole-body CT scanner in clinical use.
1979	Hounsfield and Cormack received the Nobel Prize in Physiology or Medicine

Figure 1 presents the basic scheme of a CT acquisition. The X-ray tube emits a photon beam which interacts with a collimator (the collimator prevents the irradiation

of undesired areas of the imaging object or patient). Following, the beam interacts with the patient. Then, after being attenuated by the patient, the beam produces an intensity profile in the detector array, which is positioned opposite to the X-ray tube. The attenuation profiles are obtained and recorded for all angles (the attenuation profile for a specific angle is called projection). Afterwards, the projections are processed using a reconstruction algorithm. The set of projections recorded for all angles is also called sinogram (Buzug, 2008).

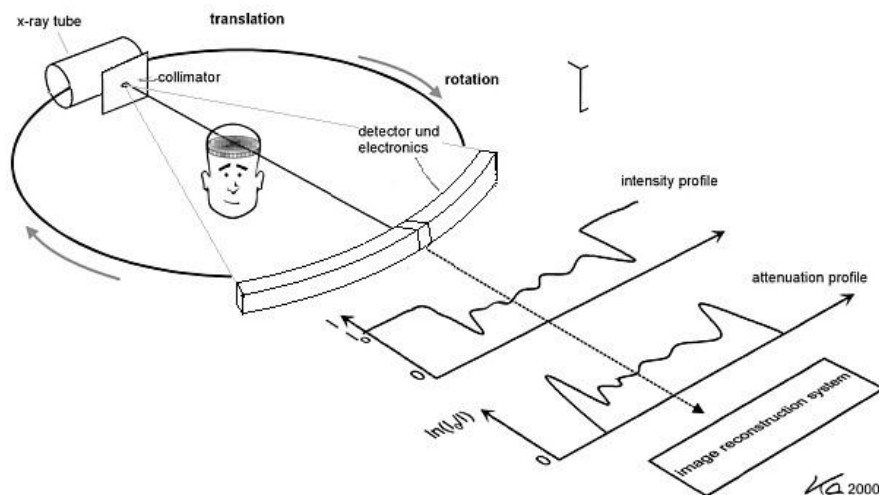


Figure 1. Simplified scheme of the measurement process for a fan-beam CT. The attenuation profile is generated from the intensity profile. Figure adapted from Kalender (Kalender, 2011).

1.1.1 Characteristics of the radiation

X-ray radiation is widely used in many medical imaging modalities such as CT, radiography, mammography, angiography, etc. Figure 2 presents some of the main elements required for the X-ray production in an X-ray tube. A filament of tungsten is heated to allow the emission of electrons by overcoming its binding energy (Buzug, 2008). The electrons are subjected to an electric field produced by a differential potential, U_a . Under the influence of the electric field, the electrons gain kinetic energy as they travel from the cathode to the anode. Then, electrons lose kinetic energy, one of the products of such energy loss are X-rays. The electron energy loss results from its deceleration produced by the interaction with the anode material (Buzug, 2008). In diagnostic radiology (excluding mammography and dentistry) the X-ray tube voltages used to accelerate electrons are in the range of 20 and 150 kV (Bushberg et al., 2011). The tube voltage U_a defines the electric field and the maximum energy of the output photons. A photon of maximum energy is generated when all the kinetic energy of the electron is converted into radiation in a single interaction.

As the electrons reach the anode, its gained kinetic energy is transformed into other forms of energy. More than the 99% of the energy coming from the collisions

produces a rise in the temperature at the target material (Oppelt, 2005). The temperature increase requires a refrigeration system for the anode. A small part of the electron kinetic energy is converted into X-ray photons. Such photons are generated by the *bremstrahlung* and characteristic emission processes (Bushberg et al., 2011).

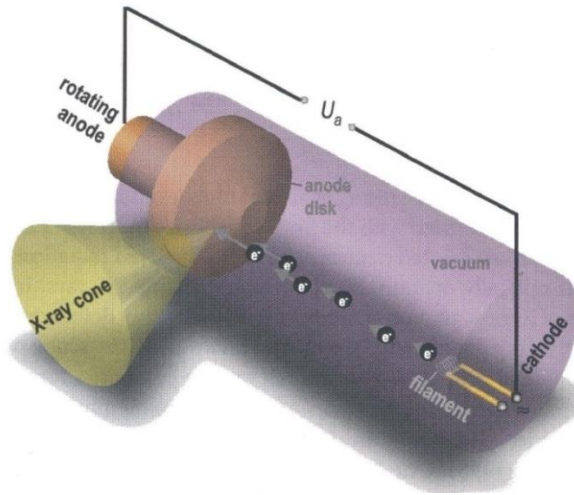


Figure 2. Schematic representation of an X-ray tube. The cathode filament is heated to approximately 2400 K. The electrons escape from the filament and are accelerated by the electric field between the cathode and anode. Reaching the anode, the electrons interact with the anode material generating a cone-shaped X-ray beam. Figure adapted from Buzug (Buzug, 2008).

The energy of the *bremstrahlung* radiation depends on the interaction distance between the electron and the nucleus of the atoms composing the target (anode). Figure 3a presents three examples of *bremstrahlung* production. When the collision with the nucleus is frontal, the total electron energy is transferred to the emitted photon. Such frontal collision represents the event when the emitted photon has the maximum energy (electron 1 in Figure 3a). If the electron passes at a short distance from the nucleus, the attractive force is intense. This intense interaction causes a great variation in the direction of the electron and consequently a moderate (less than the maximum) energy photon is emitted (electron 2 in Figure 3a). At greater distances from the nucleus (electron 3 in Figure 3a) the Coulomb force is weak, and a low energy photon is produced (Bushberg et al., 2011).

Characteristic radiation is also produced, which is distinctive of the target material. Each electron shell of an atom has a defined binding energy. Figure 3b presents the general scheme of a characteristic emission. An incident electron, with energy greater than the K-shell binding energy, interacts with the electron in the K-shell, generating a vacancy. Then, an electron from an external shell fills the generated vacancy. A characteristic photon is emitted as a consequence of the vacancy filling. The characteristic transitions that produce photons with greater energy are those in which the vacancy belongs to the K-shell (Bushberg et al., 2011).

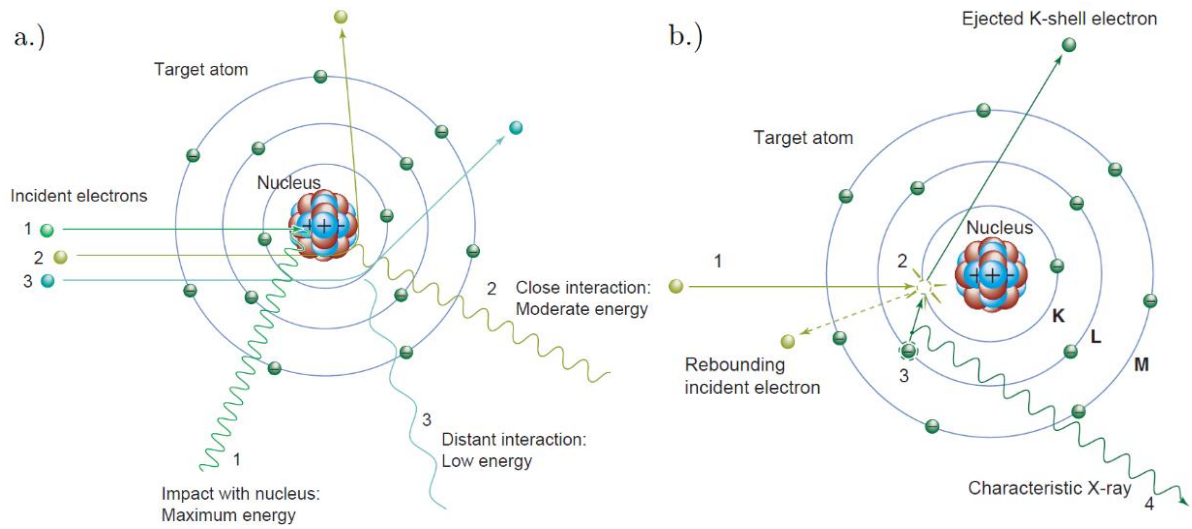


Figure 3. a.) Diagram of the events for production of the *bremsstrahlung* radiation. The process 1 represents a frontal collision, which generates the photons with maximum energy. Processes 2 and 3 present the dependence of the interaction with distance. The farther the electron passes from the nucleus, the weaker the interaction and energy of the emitted photons. b.) Diagram of the emission of characteristic radiation. First (1) the incident electron interacts with the K-shell electron and a vacancy is created (2). Then an electron from an external shell occupies the vacancy (3) and a characteristic photon is emitted (4). Figures adapted from Bushberg et al. (Bushberg et al., 2011).

In the X-ray spectrum shown in Figure 4, it is possible to differentiate the two main radiation components: *bremsstrahlung* and characteristic lines. The *bremsstrahlung* radiation can be recognized as the continuous component of the spectrum. The characteristic radiation is presented as the sharp peaks. The spectrum of Figure 4 was generated using 80 kV with 6 mm of added Al filtration (P. Costa et al., 2007).

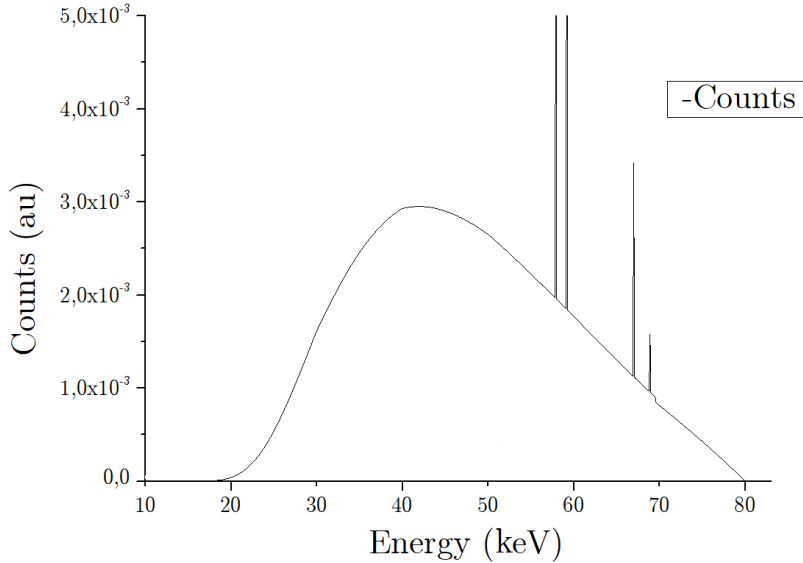


Figure 4. Normalized spectrum obtained with 80 kV and filtration of 6 mm Al. The continuous component corresponds to the *bremsstrahlung* radiation. The sharp peaks present the different characteristic transitions that take place in tungsten when the tube voltage is 80 kV. The anode angle was 10, the spectrum was generated using the modified TBC model (P. Costa et al., 2007).

1.1.2 Scanning geometry

CT devices are machines containing heavy mechanical, electrical and electronic components that allow the correct operation of the system. Figure 5 presents the geometric arrangement of the principal physical components of a CT device. The dimensions of the CT components shown in Figure 5 may vary among devices. The upper component is the X-ray tube, where the X-rays are produced. The shaped filter and the collimators of the beam are placed limiting the X-ray beam region. The gantry opening contains the field of measurement where the patient or object of interest is positioned. The centre of the field of measurement coincides with the rotation centre. Finally, the detector array is composed of fixed and adjustable collimators and the detector material. After the detector array, there are placed all the electronics necessary to store the projection data to its posterior computational analysis.

Collimators are an important element in the CT machines. Figure 5 shows some of them in both frontal and lateral views. The main function of collimators is to limit the spatial distribution of the radiation. The first collimation of the X-ray beam is provided by the own coating of the X-ray tube. The fixed collimator limits the maximum beam aperture of a scan. The adjustable collimator is positioned closer to the gantry opening to minimize penumbra regions (Kalender, 2011). A collimator in front of the detectors is used to reduce the influence of the scattered radiation in the detected signal. The optional collimators are positioned along the z-axis and aligned to the focal spot.

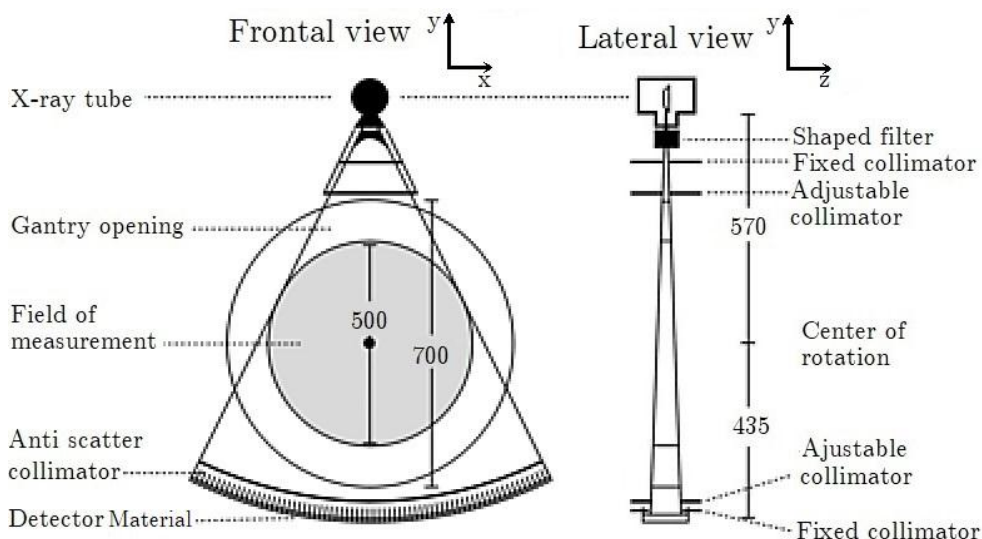


Figure 5. Principal components of the scanning geometry of a CT. The dimensions shown are in mm. Figure adapted from Kalender (Kalender, 2011).

One of the important parts of modern commercial CT scanners is the shape filter or bowtie filter. This filter imposes a variable angular filtration along the fan angle. It seeks to homogenize the X-ray detector intensity when imaging a patient. A

dose reduction is achieved as a consequence of the larger filter thickness near the periphery of the fan beam (Kramer et al., 2017).

State-of-the-art clinical CT devices use detector blocks that are easily removable for fast repair as shown in Figure 6. The detectors use scintillator crystals or ceramics as detecting material (Kalender, 2011). The crystals are mounted in modules and the space between the detectors is filled with an opaque material to avoid optical crosstalk. The photodiodes are positioned between the scintillator crystals and the electronic module. The latter, electronic module, lays below the crystals and photodiodes. It supplies the electric power to the photodiodes and receives the electronic signals to be processed. The electronic modules process the signals of the detectors and convert them to digital numbers (Bushberg et al., 2011). The sensitive materials of the detectors, photodiodes and electronic elements vary among vendors, but their general operation is similar.

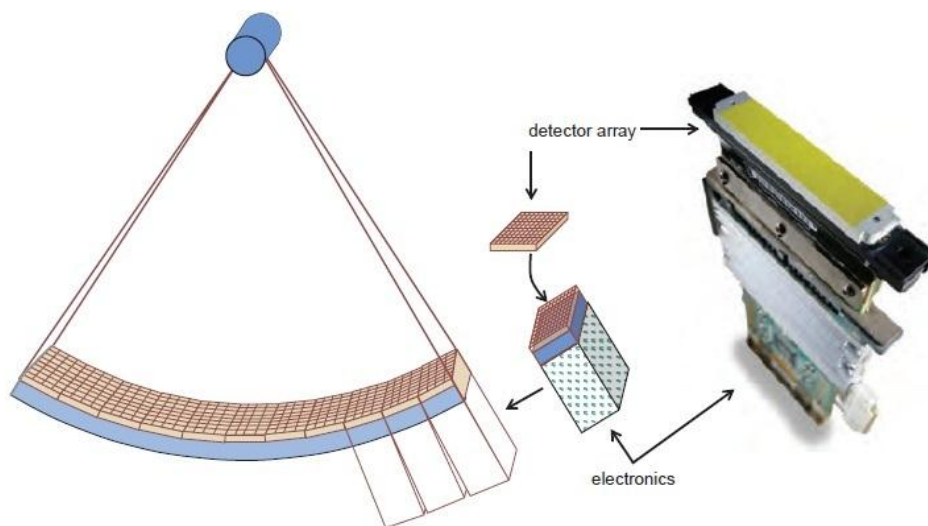


Figure 6. Geometric arrangement of the detectors in a CT. It is possible to see how the detector blocks are positioned in the angular direction, the figure also presents a photograph of a detector element with its electronic module. Figure adapted from Bushberg et al. (Bushberg et al., 2011).

1.1.3 Filtered Backprojection (FBP)

This section describes the basic concepts of the Filtered Backprojection (FBP) algorithm used for the reconstruction of projection data. A detailed description can be found in the CT specialized literature (Buzug, 2008; Kalender, 2011; Oppelt, 2005). More sophisticated variants of the FBP algorithm, such as FDK method were studied by Caldas et al. (Caldas, E. 2008; Caldas et al., 2010)

The FBP is an algorithm that solves a spatial function when its projections have been measured. Once the projections have been acquired, the method back projects them to find the spatial distribution of the desired function. The standard form of a projection for a specific angle is presented in equation (1).

$$P(L) = \int_L f(x, y) |ds| \quad (1)$$

It presents the integral projection, along the straight-line L , which can be solved using the Radon inverse transform. This transform is the basis of the *Backprojection* method (Buzug, 2008; Deans S., 1993; Radon J., 1917). The function $f(x, y)$ is a spatial function and $P(L)$ presents the integral of the function $f(x, y)$ along a straight-line L .

The following paragraphs present the procedures and equations necessary to describe the CT detectors measurements as equation (1).

In a simplistic representation, the intensity, I_j , measured by the detector j , in the presence of an attenuator object can be written as equation (2) (Buzug, 2008).

$$I_j = g_j I_0 e^{-\int_L \mu(l) dl} \quad (2)$$

I_j represents the intensity measured when the photon beam crosses a series of materials with attenuation coefficient $\mu(l)$, l represents the position along the line L . The term g_j represents the detector gain. I_0 represents the intensity measured without attenuator object.

To obtain the attenuation profile it is necessary to compare the intensity measured in the presence of the object, I_j , with the reference intensity measured in the absence of the attenuator material, I_r . I_r is also related to I_0 as

$$I_r = g_r I_0 \quad (3)$$

where g_r represents the detector gain. Equation (4) defines the projection data measured by the detector j .

$$P_j = \ln \left(\frac{g_j I_r}{g_r I_j} \right) = \int_L \mu(l) dl \quad (4)$$

It is possible to see that using such definition the projection data represents the integral of the attenuation coefficients of the materials through which the radiation was transmitted. The integral of equation (4) is in the projection form presented in equation (1). Then, in principle, the function μ could be reconstructed from the projections using the Radon transform (Deans, 1993).

Taking into account that the X-ray beam used in CT is polyenergetic, the projection data differs from equation (4). The attenuation data A is expressed as

$$A = \frac{I}{I_0} = \frac{\int_E S(E)D(E)e^{-\int_L^{\mu(E,x,y)ds} dE}}{\int_{E'} S(E')D(E')dE'} \quad (5)$$

where $S(E)$ and $D(E)$ represent the X-ray spectrum and the detector response, respectively. It is possible to include the $S(E)$ and $D(E)$ information in a weight function $w(E)$ as defined in

$$w(E) = \frac{S(E)D(E)}{\int_{E'} S(E')D(E')dE'} \quad (6)$$

Then the attenuation A simplifies as presented in

$$A = \int_E w(E)e^{-\int_L^{\mu(E,x,y)ds} dE} \quad (7)$$

From equation (7), assuming small and low atomic number absorbers, the exponential term, containing the integral of the attenuation coefficient, can be expanded as

$$A = \int_E w(E) \left(1 - \int_L \mu(E,x,y)ds + \frac{1}{2} \left[\int_L \mu(E,x,y)ds \right]^2 + \dots \right) dE \quad (8)$$

It is possible to simplify the first integral in equation (8) as $\int_E w(E)dE = 1$. Then, taking the logarithm of equation (8), we get

$$\ln(A) = \ln \left(1 - \int_E \int_L w(E)\mu(E,x,y)dsdE + \frac{1}{2} \int_E w(E) \left[\int_L \mu(E,x,y)ds \right]^2 dE + \dots \right) \quad (9)$$

It is possible to use the result of the Taylor series for $\ln(1-x) \approx -x$ with $x \approx 0$, this is the small-object approximation. Equation (9) becomes

$$\ln(A) = - \int_E \int_L w(E)\mu(E,x,y)dsdE + R \quad (10)$$

in which R represents the higher-order terms of the attenuation coefficient which are considered small (Heismann et al. 2012).

Defining $\bar{\mu}(x,y)$ as

$$\bar{\mu}(x,y) = \int_E w(E)\mu(E,x,y)dE \quad (11)$$

the attenuation logarithm is rewritten as

$$-\ln(A) = \int_L \bar{\mu}(x,y)ds \quad (12)$$

Equation (12) presents the form of the projection integral that can be solved using the Radon transform (equation 1). It is important to remark that $\bar{\mu}(x, y)$ is not the actual attenuation coefficient. It represents the mean attenuation coefficient weighted with the spectrum and detector response functions. It was also obtained using small objects with low attenuation properties. Errors generated by this approximation are usually referred as beam-hardening artefacts (Heismann et al., 2012).

A basic scheme of the *Backprojection* method is presented in Figure 7. It also presents how the implementation of a mathematical filter affects the definition of the reconstructed image. This technique is named Filtered *Backprojection*. As shown in Figure 7 a), the use of the simple *Backprojection* leads to blurred images (Bushberg et al., 2011). The use of a filter to convolute the projections generates sharp images as Figure 7 b).

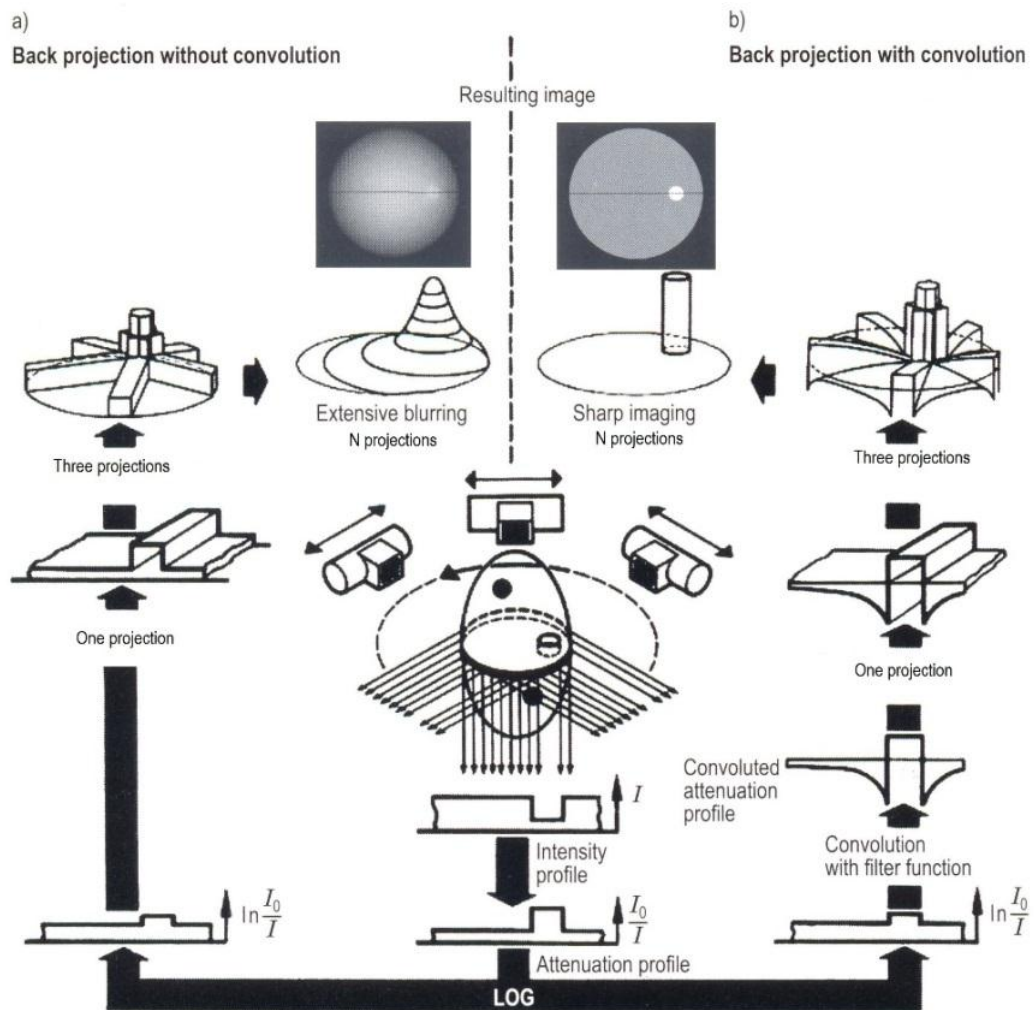


Figure 7. Representation of the image reconstruction via *Backprojection*. Different results are obtained using the a) simple *Backprojection* and b) the Filtered *Backprojection*. Figure adapted from Oppelt and Kalender (Oppelt, 2005; Kalender, 2011).

The mathematical behaviour of some filters commonly used to perform the Filtered Backprojection as a function of the spatial frequency is shown in Figure 8. The filters in Figure 8 are useful to reduce the unfiltered image blurring as they decrease the contribution of the low frequencies to the reconstruction. The filter used to reconstruct the images in this work is the Ramp filter, also known as Ram Lak filter. Further information and description of different filters and its effects on the reconstructed images can be found in the Image processing specialized literature (Demirkaya, 2008).

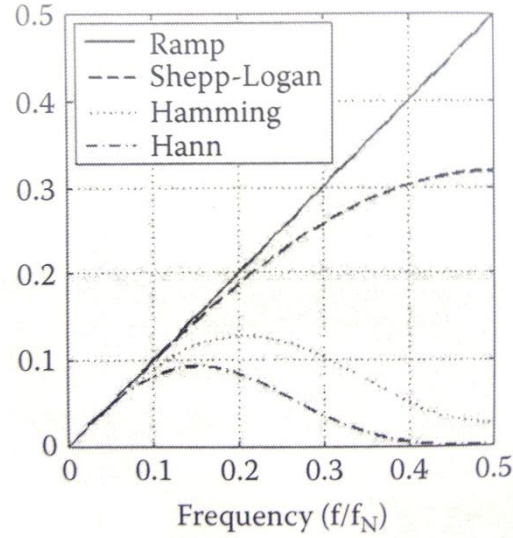


Figure 8. Graphs of the Ramp, Shepp-Logan, Hamming and Hann filters. Figure adapted from Demirkaya et al. (Demirkaya, 2008).

1.1.4 Hounsfield units (HU)

As explained in the previous section, the CT reconstruction provides the spatial distribution of $\bar{\mu}$, $\bar{\mu}(x, y)$. Such $\bar{\mu}(x, y)$ depends on the spectra used as in equation (11) via the weighting factor $w(E)$. A comparison between images presenting $\bar{\mu}(x, y)$ would be difficult as different devices use different voltages and filtration. For this reason, the Hounsfield Units (HU) were introduced as a reference unit to present the attenuation maps. Hounsfield Units (HU) were named in honour to Godfrey Hounsfield and its values are known as CT numbers. These units represent the attenuation relative to water and air. Their definition is presented in equation (13) (Hurrell et al., 2012). The CT numbers for water and air are fixed values as they do not depend on the used spectrum (Kalender, 2011).

$$HU = 1000 \times \frac{(\bar{\mu}_{material} - \bar{\mu}_{water})}{(\bar{\mu}_{water} - \bar{\mu}_{air})} \quad (13)$$

The $\bar{\mu}_{air}$ in equation (13) is normally ignored and taking it to zero is a correct approximation. As mentioned, HU vary with energy. It has been demonstrated that the HUs from different tissues present closer values when increasing the X-ray beam energy (Hurrell et al., 2012).

Figure 9 presents the usual CT values for body tissues. In this case, ranges are shown instead of exact values. One reason for the ranges is that the CT numbers vary with the energy. The other is the variability of biological tissues among patients, and consequently variable chemical composition of the tissues.

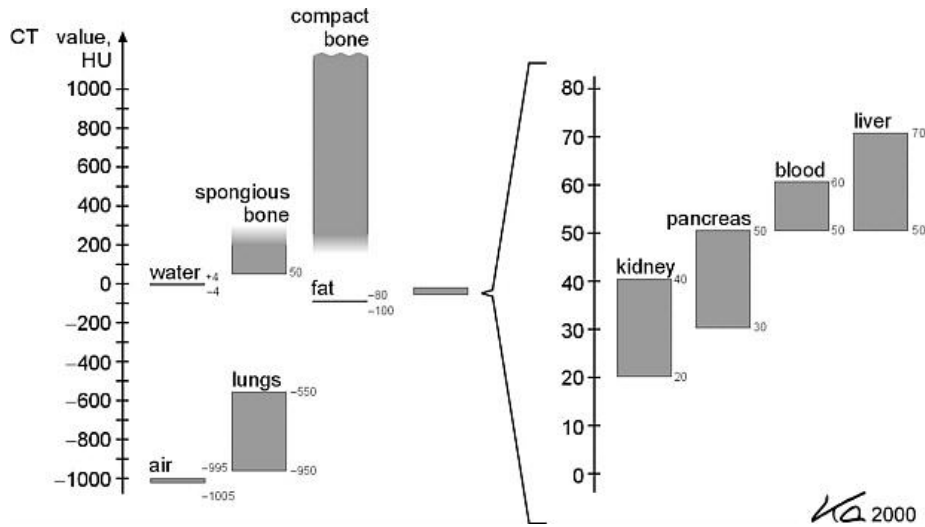


Figure 9. Usual CT values for various body tissues. Figure adapted from Kalender (Kalender, 2011).

1.1.5 Image quality parameters

The image quality in medical imaging is important to guarantee that the information contained in an image is able to assist the medical staff for adequate diagnostic decisions. Different methodologies and parameters allow the quantification of the image quality. In this section, some of the image quality parameters used in this work are presented.

Contrast to Noise Ratio.

The Contrast to Noise Ratio (CNR) is a parameter that relates two signal levels in the presence of noise. It is defined as

$$CNR = \frac{(\bar{x}_s - \bar{x}_{bg})}{\sigma_{bg}} \quad (14)$$

The contrast (numerator) is the difference between the mean signal in the Region of Interest (ROI) \bar{x}_s and the mean of the background signal \bar{x}_{bg} . The noise

(denominator) is estimated by the standard deviation of the background region, σ_{bg} . The usual regions used to compute the CNR in a CT image generated by scanning a CNR phantom are presented in Figure 10. CNR is a good metric to describe the signal amplitude relative to the noise (Bushberg et al., 2011).

Signal to Noise Ratio.

The Signal to Noise Ratio (SNR) is computed as

$$SNR = \frac{\sum_i (x_i - \bar{x}_{bg})}{\sigma_{bg}} \quad (15)$$

In this equation x_i represents the signal of each pixel included in the ROI, whereas \bar{x}_{bg} and σ_{bg} represent the mean and the standard deviation of the background regions (Bushberg et al., 2011). The usual regions used to compute the SNR in a CT image when scanning an SNR phantom are shown in Figure 10.

The SNR is a quantity that describes the detectability of an object. For this reason, the ROI does not need to perfectly match the object.

Both CNR and SNR are similar in their equation form as shown in (14) and (15). Nevertheless, there is a big difference between them, the selection of the regions of interest for each of them as presented in Figure 10.

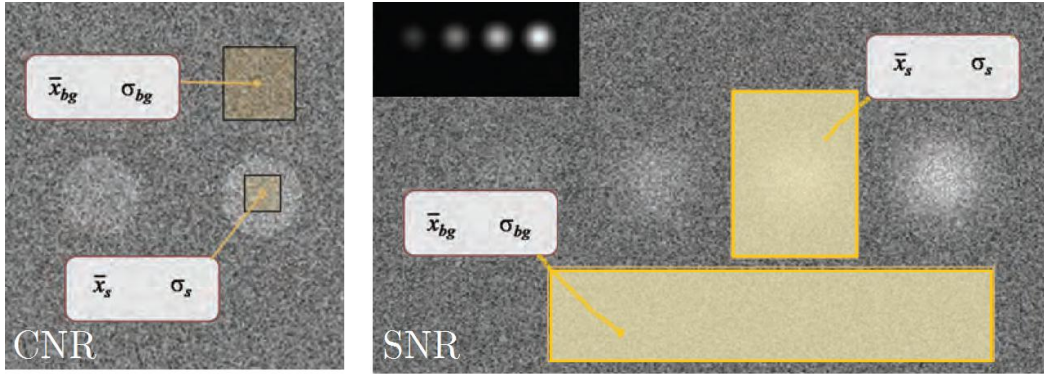


Figure 10. Example of regions and sizes usually used to measure the CNR and the SNR. Figure adapted from Bushberg et al. (Bushberg et al., 2011).

1.2 Dual Energy Computed Tomography

Dual Energy Computed Tomography (DECT) is a computed tomography modality that uses two different photon spectra to enhance the material differentiation in the tomographic images. Since physical interactions depend on both the photon energy and material composition, it is possible to characterize materials using DECT. Actually, in non-clinical DECT, it is possible to obtain properties like the mass density and the mass fractions of the compounds with high accuracy (Shimomura et al., 2017).

The advantages of DECT have been known since the late 1970s. As it requires patient irradiation with two spectra, the patient dose, involuntary motion and the required post-processing were unavoidable difficulties for its early clinical implementation. In 2006, with the introduction of the dual-source CT system, the interest in DECT renewed (Marin, 2014). Such interest led to an increase in the research and development in this technology. Nowadays, many vendors offer a variety of devices that exploit the advantages of DECT. This technologic expansion happened simultaneously to an increasing interest in medical imaging, leading to an increase in the literature on dual-energy CT for a variety of clinical applications (Marin, 2014).

There are several clinical applications for thorax and whole-body DECT. Some of them seek to differentiate tissues based on its composition and others use contrast agents to improve differentiation. Some clinical applications of DECT are aorta examinations, angiography with bone subtraction, virtual non-enhanced images with contrast media that allow the detection of organ lesions, estimation of the composition of kidney stones and gout diagnosis, among others (Johnson et al., 2011). Figure 11 shows some clinical images of the knee, confirming the presence of monosodium urate (MSU) that accumulates in joints, as a sign of gout (Nicolaou et al.2011).



Figure 11. DECT images with material decomposition confirm the presence of monosodium urate (MSU) in green, in the knee region. Figure adapted from Nicolaou et al. (Nicolaou et al.2011).

1.2.1 Basic principles of DECT

Standard CT tissue differentiation (contrast) is based on the differences in CT numbers of the pixels or voxels of the image. An image obtained using only one energy spectrum can present similar CT values for different elements such as calcium and iodine (Fornaro et al., 2011). At the same time, CT numbers vary for different energy spectra and this energy dependence is the base of spectral differentiation algorithms.

Spectral CT is an imaging modality which uses more than one spectrum to obtain CT images containing additional information of the materials of the imaged object. DECT is a specific case of spectral CT, in which two spectra are used to acquire CT images.

As exposed by Johnson and Kalender (Johnson T., & Kalender W., 2011) there are three requirements for spectral and dual energy CT to work properly. Such requirements refer to X-ray spectra, detectors and tissues characteristics.

X-ray Spectra

As in the case of the standard X-ray devices, DECT sources produce spectra composed of *bremsstrahlung* and characteristic radiation. Generally, there are two operation tube voltages: 80 and 140 kV.

For the material differentiation to work properly, it is important to have spectra with minimum overlap. Some aspects concerning the possible radiation used in clinical DECT are presented below:

- Monochromatic radiation is not clinically available because, currently, such sources do not provide the photon output required for clinical imaging purposes. In addition, the production of monoenergetic radiation requires complex equipment which would difficult its clinical availability;
- CT spectra generated with tube voltages lower than 80 kV produce photons with low energies. These photons would be easily absorbed by the human body generating noisy images and higher radiation doses;
- Spectra generated with tube voltages higher than 140 kV would produce photons for which the soft tissues would be transparent leading to low soft tissue contrast images (Johnson T., & Kalender W., 2011).

For these reasons, the pair of spectra used in DECT is produced with tube voltages between 80 and 140 kV. Examples of spectra used in different DECT implementations are shown in the section 1.2.2.

Detector

The ideal spectral detector system would discriminate the energy of photons and would work with high fluence rates. Both features are not currently available for clinical applications. Various prototypes have been studied for future clinical implementation (Schlomka et al., 2008; Cormode et al., 2017). In CT, detectors measure the integrated signal of various photons reaching the detection surface within a readout interval. There are some counting detectors currently available for research and industry applications. Such counting detectors do not work properly for the fluence requirements of clinical CT machines (Johnson, 2012).

Regarding the current detector systems, there are two modalities of DECT devices. The first modality uses two spectra and has geometric arrangements of the source and/or detectors that allow the separation of the photons coming from each spectrum. The other modality adopts the dual layer detector hardware, which uses only one radiation spectrum. This kind of equipment uses pairs of detectors with different energy responses with the capability of separating the photons in two ranges of energies (Vlassenbroek, 2011).

Materials

The mass attenuation coefficient for the diagnostic energy window is composed of three processes: Compton scattering, photoelectric absorption and Rayleigh scattering. The three processes are shown in Figure 12 for water and bone as a function of the energy. The main contributors to attenuation, at the energy range of diagnostic radiology, are Compton scattering and the photoelectric effect. Both, Compton scattering and the photoelectric effect are energy and material-dependent (Fornaro et al., 2011).

The contribution of Compton scattering is almost constant in the energy range of diagnostic energies. Then, in this energy range, Compton scattering depends more on electron density than in the energy itself. On the other hand, the photoelectric contribution depends strongly on energy. Its contribution to the total attenuation coefficient predominates at lower photon energies. In addition, the photoelectric effect occurs with higher probabilities in materials with high atomic numbers (Nelson & Rewy, 1965).

As a result, CT numbers for soft tissues do not vary much with beam energy. Nevertheless, the CT numbers vary considerably for high- Z materials (Johnson, 2007). Thus, the differentiable materials need to exhibit differences in CT numbers for different energies, so that clinical DECT will present a considerable improvement

differentiating high Z or dense materials like bone, calcified nodules, and contrast agents as iodine ($Z=53$), among others.

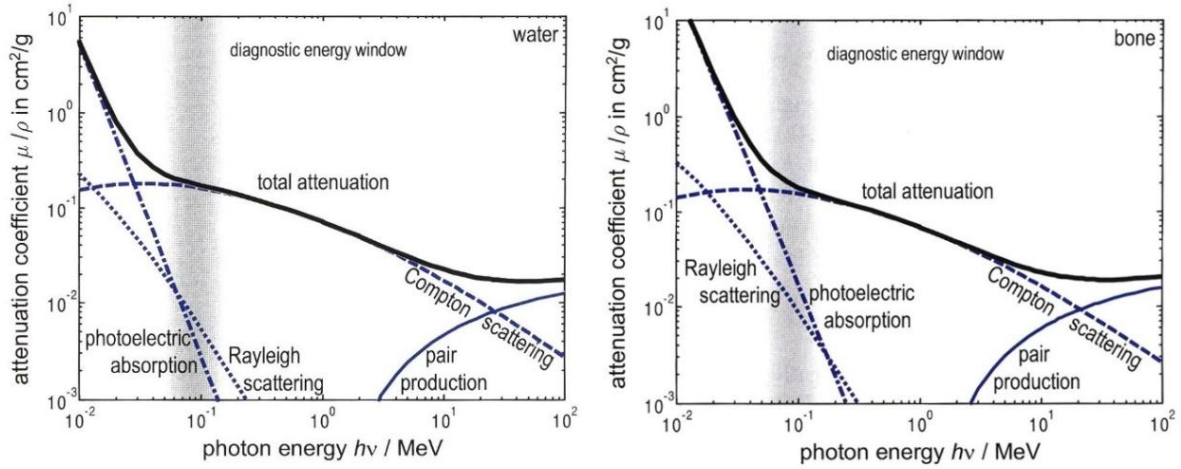


Figure 12. Mass attenuation coefficient as a function of incident photon energy for water and bone. The vertical dotted section represents the energy range of X-rays for diagnostic radiology. Figure adapted from Buzug (Buzug, 2008).

1.2.2 Devices for Spectral CT and DECT

Currently, there are commercial devices that use spectral and dual energy CT benefits for clinical purposes. Gong et al. (Gong, 2017) published a bibliometric analysis of the 50 most cited articles on DECT in abdominal radiology. Such study presents the statistics of the DECT technology used in the articles, they found that most of the studies used Dual Source methods (35 articles, 70 %), 28% used Rapid kV switching (14 articles) and 2% used the sequential acquisition method (1 paper). In this section different approaches used to perform Dual Energy CT and spectral CT are briefly explained.

Figure 13 represents the main CT configurations that explore the advantages of spectral and dual CT methods. As explained by Heismann et al. (2012), there are two kinds of devices that explore the spectral properties. The first one base its spectral separation on the X-ray tube voltage and filtration, using two X-ray spectra to acquire the images (Figure 13 a, b and c). The other devices are based on the response of the detectors, using an only spectrum to obtain the images (Figure 13 d and e, most recent approaches).

The three approaches that are currently used in clinical practice are dual-source CT, the rapid voltage switching CT and dual layer CT. The CT configuration also defines the kind of reconstruction algorithm that can be employed to obtain the spectral information of the images. There are two main options for DECT image reconstruction: the reconstructions based on the projections (section 1.3.1) and the reconstruction based on the standard images (section 1.3.2).

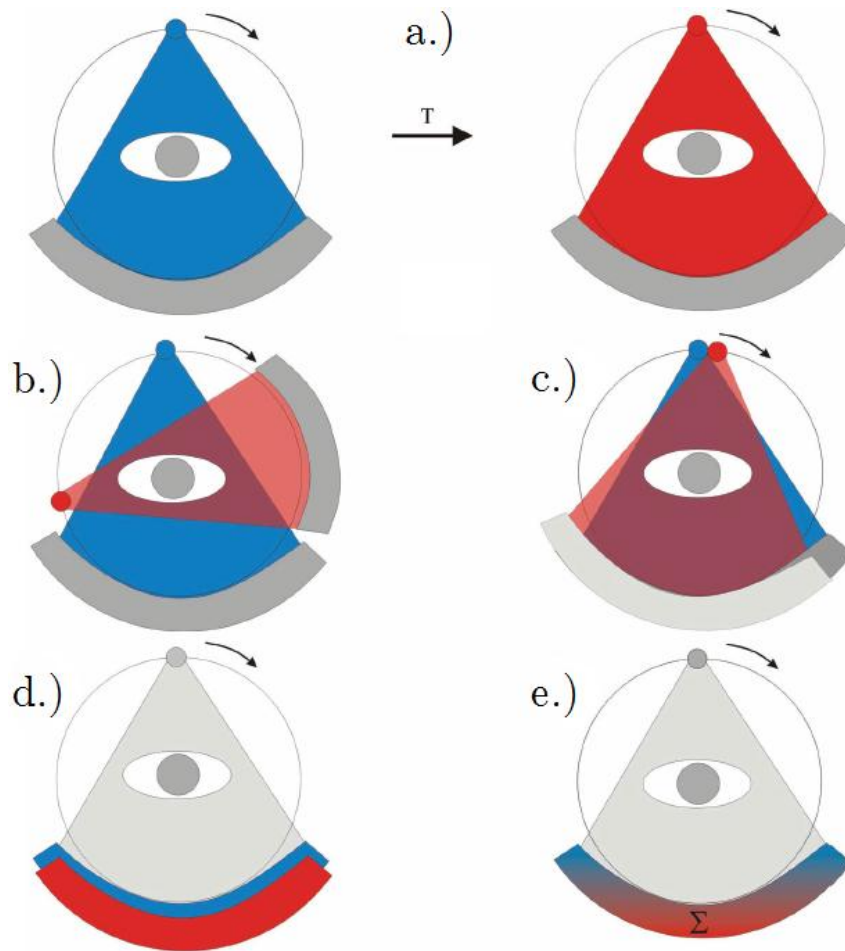


Figure 13. Schematic configurations of Spectral and Dual Energy CT devices. a.) Sequential acquisition CT. b.) Dual Source CT. c.) Tube kV Switching CT. d.) Dual Layer CT. e.) Photon Counting CT. Adapted from Heismann et al. (Heismann et al., 2012).

a.) Sequential acquisition

This implementation is based on the sequential acquisition of independent images, as shown in Figure 13a. It enables the use of optimal spectral separation by changing the filtering and tube voltages between the images. It also ensures that the detected photons come from each spectrum.

It can be used for dual-energy imaging in static situations, such as the characterization of kidney stones and gout diagnosis. It can also be used with contrast agents in the late phases when contrast equilibrium is reached (Heismann et al., 2012). However, it is almost clinically unused because the images generally present artefacts caused by patient motion between scans.

b.) Dual-source CT

This kind of device possesses two X-ray sources and two detector sets. Figure 13b presents its geometrical configuration. An advantage of these devices is that different filters can be used to improve spectral energy separation. At the same time, both tube currents can be adjusted to produce similar photon output. An example of the output photon distributions that can be adopted when using different filters and currents is presented in Figure 14. High temporal resolution is allowed due to the simultaneous image acquisition.

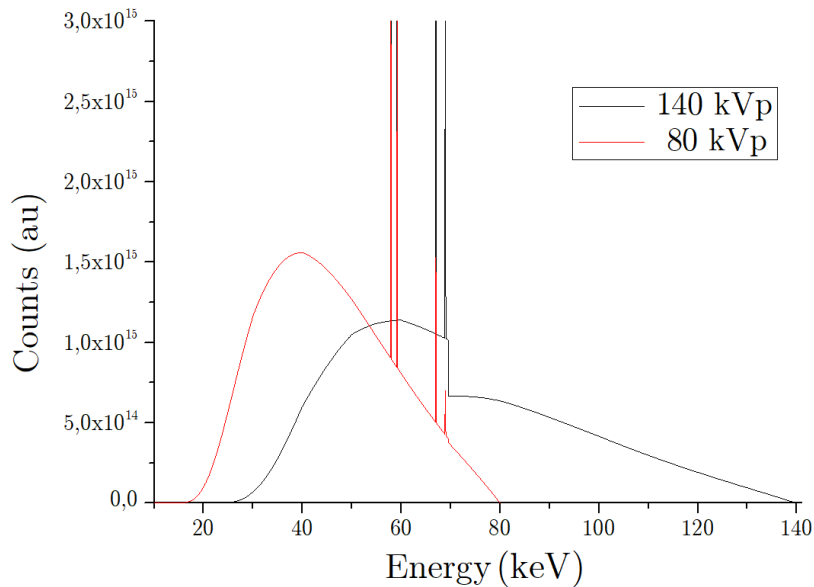


Figure 14. Example of the X-ray spectra that can be used in Dual Source CT with the two tubes running at 80 and 140 kV. The 140 kV spectrum is acquired with an additional filter which reduces the overlap of the spectra. It is also possible to increase the mAs of the low energy spectrum, corresponding to 80 kV, which in this case, is the double of the other. Spectra obtained using the modified TBC model (P. Costa et al., 2007).

A disadvantage is that the scatter radiation coming from one X-ray tube affects the signal of the detectors corresponding to the other tube. The high and low kV images are reconstructed separately. As there is no time correspondence for the projections, the post-processing algorithm is based on the reconstructed standard images (Krauss et al., 2011).

Currently, there are two clinical devices that use this technology: SOMATON Definition and SOMATON Definition Flash (Siemens, Germany). Both devices have similar configurations, but the Definition Flash has some improvements, such as faster tube-detector rotation and a large angle between the sources (95° instead of 90°), which allows a greater Field Of View (FOV), enabling imaging of oversized patients (Johnson et al., 2011).

c.) Rapid kV switching CT

This is a more refined approach to the sequential acquisition. Its geometrical configuration is shown in Figure 13c. The tube voltage is interleaved between 80 and 140 kV while taking the image projections. Its operating mode allows temporal correspondence of projections, full FOV, as well as the use of both Projection-Based and Image-Based reconstruction algorithms. The angular difference between the projections (section 1.3) can be overcome by applying interpolation in one of the projection data.

The device that incorporates this technology is the Discovery CT 750 HD *Gemstone Spectral Imaging* (GSI) (General Electric, USA). The name Gemstone imaging comes from its detector system. The scintillator material presents advantages over standard CT detectors. The reduced decay time and smaller afterglow level of the GSI detector make possible the faster sampling (Chandra & Langan, 2011). A limitation of this kind of devices is the switching time which is in the order of 1 ms, consequently, it takes between 0.6 to 1 second to complete an entire rotation. Therefore, images of fast-moving organs like the heart are difficult to obtain using this kind of technology (Heismann et al., 2012).

The X-ray tube switches the tube voltage between two values. It uses the same filter while acquiring the projections. Then, the photon distributions generated using the same filter at 80 and 140 kV are like those presented in Figure 15.

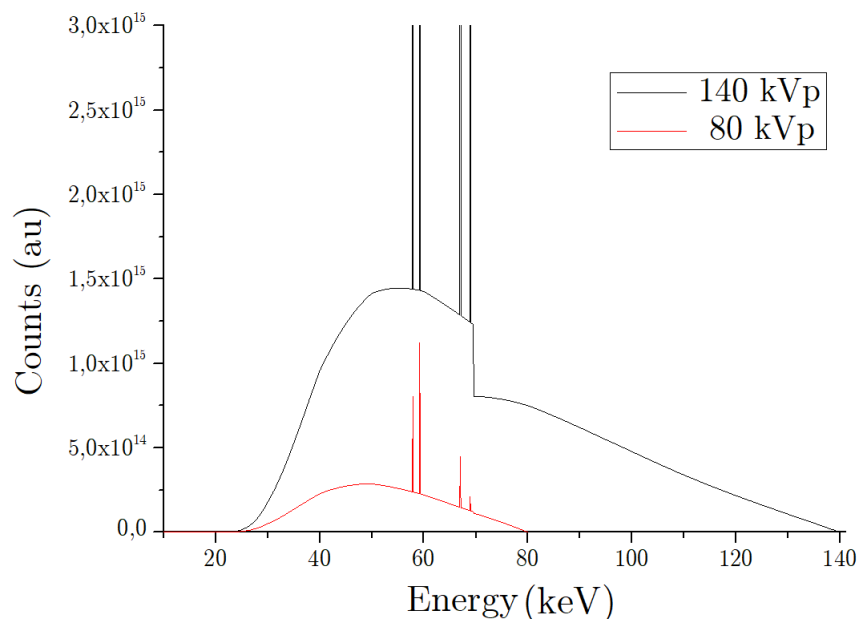


Figure 15. Spectra obtained for 80 and 140 kV. Spectra generated using 2 mAs and the same filter of 4mm Al. Spectra obtained using the modified TBC model (P. Costa et al., 2007).

Figure 15 presents a clear difference in the number of particles produced at each tube voltage. The tube current and voltage switching functions are time limited in this device, so in general, the low energy spectrum would produce an inferior number of photons (T. Johnson et al., 2011). Theoretically, it would be necessary a correction, irradiating the imaged object more time with the 80 kV spectra than the 140 kV spectra. Furthermore, the real CT system has no ideal kV switching. Then, more than two spectra are used while acquiring an image and the low/high irradiation times are defined in a more complex way (Chandra & Langan, 2011).

The possibility of almost simultaneous acquisition of projections of both spectra makes the Projection-Based reconstruction feasible. Figure 16 represents the reconstruction options of the GSI device. It is necessary to split the interleaved spectrum into the high and low projections. Standard images can be obtained from the separated attenuation projections. It is also possible to use the Projection-Based algorithm to find two projections of materials of interest and from them to reconstruct images for each material. Finally, virtual monoenergetic images can be acquired from the material images. A detailed explanation of the process to obtain the images is presented in section 1.3.1.

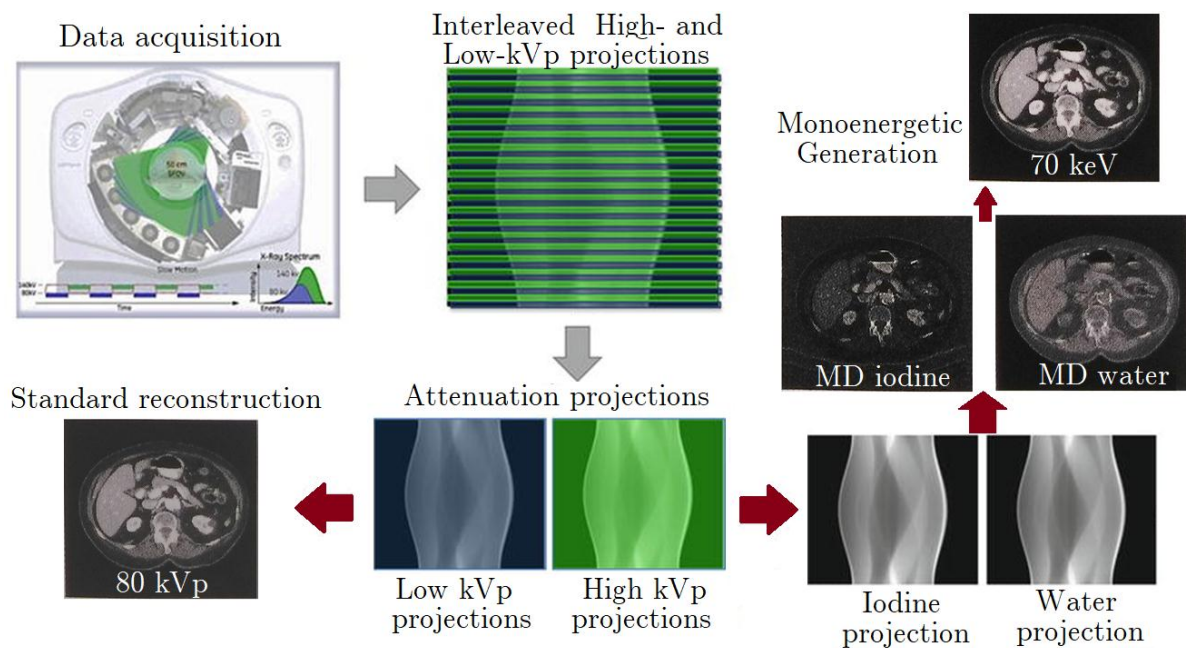


Figure 16. Scheme of the operation mode of the Discovery CT 750 HD. Red arrows represent the reconstructions sequence. The interleaved sinogram is split in the projections corresponding to each kV. From such projections, standard images can be reconstructed. Projections of materials of interest as iodine and water are also obtained performing the Projection-Based BMD on the standard sinograms. From these material projections, material concentration images can be reconstructed. Finally, virtual monoenergetic images can be obtained from the material concentration images. Figure adapted from Chandra & Langan (Chandra & Langan, 2011).

d.) Dual layer CT

The third DECT clinically available device is based on its detector system. In this case, the source works as in standard CT, with a single spectrum. There are two detectors layers with different energetic responses. The geometric CT configuration is shown in Figure 13d. The two scintillator arrangements absorb the photons sequentially. Its clinical implementation was done by Phillips in the IQon Spectral CT (Philips, 2017).

The advantage of using this kind of system is the use of only one X-ray source, which means time and spatial registration correspondence and full FOV. This approach acquires projections simultaneously which makes it ideal for fast-moving organs as the heart. Disadvantages include hardware effort and poor spectral separation. A scheme of the spatial distribution of the two layers of detectors is represented in Figure 17.

Images are reconstructed separately for each layer or can be used to obtain material information using Projection-Based methods (Ehn S., 2017). It is also possible to combine the data of the two layers to obtain standard CT images.

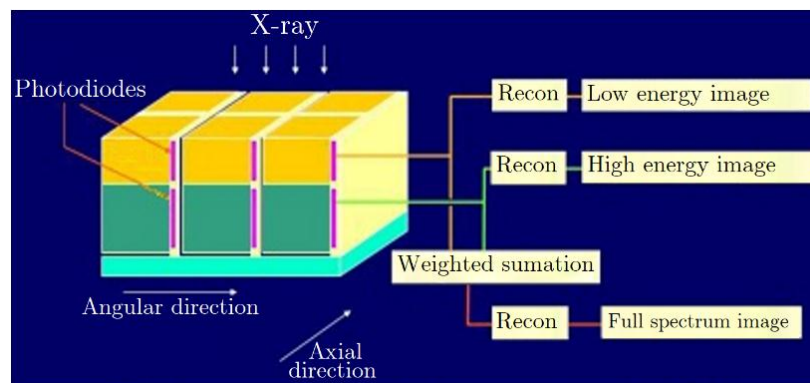


Figure 17 Schematic representation of the dual layer detector system (few elements shown). There are shown the two photodiodes of each pair of detectors. Figure adapted from Vlassenbroek (Vlassenbroek, 2011).

The use of scintillator detectors rather than photo-counting detectors is due to the counting rate performance capabilities. The thickness of both layers was specially designed so that each absorbs approximately the 50% of the radiation. The upper layer absorbs most of the low-energy photons of the incident radiation, and the bottom layer the remaining high energies (Vlassenbroek, 2011). Figure 18 presents the sensitivity curves for both detector layers.

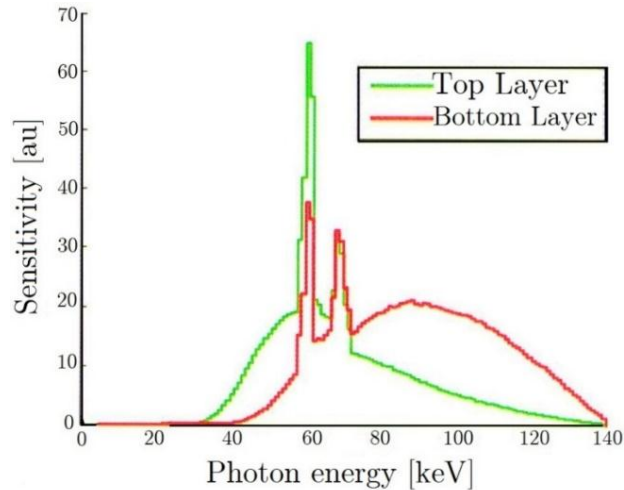


Figure 18. Sensitivity spectra of the two layers, the considerable overlap limits spectral contrast. Figure adapted from Johnson and Kalender (Johnson & Kalender, 2011).

a.) Photon counting CT

Nowadays, this modality is not available for clinical procedures but is a subject of ongoing research, and its technology represents a promising development in CT. Figure 12e presents its geometrical configuration.

Patients or image objects are irradiated with a single spectrum and the energy separation is performed on the detection system. The detectors are capable of counting discrete photon interactions (McCollough, 2015). There is a current challenge for this image modality to be implemented in clinical imaging. These photo counting detectors saturate for the high fluence rates necessary in clinical CT. Current photo-counting detectors experience loss of counts due to pulse pile-up effects at high fluence rates and can even become fully paralyzed (McCollough, 2015).

Additionally, the algorithms implemented to obtain the material information are different to the ones explained in this work, as there are used more than two energy channels, more than two material images can be acquired.

For example, Schlomka et al. (Schlomka et al., 2008) used a CT Photo-counting prototype and six energy channels to solve four “material” images. As base functions they used: photoelectric and Compton cross sections and the mass attenuation coefficient of gadolinium and iodine. Other CT prototypes have explored the performance and spectral characteristics of these devices (Heismann et al., 2012). For instance, Hurrell et al. (Hurrell et al., 2012) used six energy channels and demonstrated the HU dependence on the energy and how such concept must change if spectral CT imaging becomes a clinical tool for diagnosis.

Moreover, there have been studies where clinical CT conditions were set up and diverse features such as noise, dose, spatial resolution, mean HU were compared with standard CT procedures (Yu et al., 2016; Pourmorteza et al., 2016; Kalender et al., 2017).

Photon counting detectors are also used to improve materials detection in non clinical procedures. Rebuffel et al. (Rebuffel et al., 2011) presented a technique using photon counting detectors in radiography to improve the detection of explosives in luggage.

To summarize the different devices that implement dual and spectral energy methods, Table 2 exhibits the main advantages and disadvantages of each method presented in the last pages.

Table 2. Summary of the principal features of each Dual and Spectral Energy CT device, described in this section (McCollough, 2015).

Device	Advantages	Disadvantages
Sequential acquisition	Can be performed on any CT scanner (no special hardware required).	Susceptibility to motion, misregistration between the low- and high-energy images.
Dual-Source CT	Tube current and tube filtration can be optimized to generate low spectral overlap, which improves contrast-to-noise ratio in material-specific images. Beam-hardening corrections are applied to the standard images, allowing material-specific images to be created in the image domain.	Requires specialized hardware. The 90-95° phase shift between low- and high-energy data. Simultaneous use of two x-ray sources permits scattered radiation whose original primary photon came from one tube to be detected by the detector of the other tube, needing particular scatter correction.
Rapid kV switching CT	Almost simultaneous data acquisition of the low- and high- energy projections. Allows BMD algorithms by using either projection data or reconstructed images. Reduces beam-hardening artifacts in “virtual monoenergetic” images	Requires specialized hardware. Relatively high overlap of the energy spectra.
Dual Layer CT	Simultaneous acquisition of the low- and high-energy data set. All image data are acquired in a manner that supports material-specific imaging.	Requires specialized hardware. Fairly high overlap of the energy spectra (detector sensitivity).
Photo Counting CT	Uses energy-specific measurements and energy thresholds to reject electronic noise. Enables new imaging approaches, such as k-edge subtraction.	Involves specialized hardware, which is not anticipated to be commercially available for some time, if at all.

1.3 DECT Algorithms

The use of two energy spectra to irradiate materials allows the reconstruction of maps representing material properties which vary with the radiation energy. One of the interests in clinical radiology is to differentiate materials with similar CT number in standard CT images. When information of two different spectra is available, it is possible to segment an image into two components.

Therefore, depending on the selected functions, it is possible to reconstruct bone and soft tissues images, as well as, to obtain images of water and contrast agents. These Basis Material Decomposition (BMD) methods can increase the accuracy of medical diagnosis. Alvarez and Macovski (Alvarez et al., 1976) presented the BMD method in 1976. Since then, it has been used as the benchmark in DECT. There are two algorithms that use BMD: one is based on the physical information contained in the projections (or sinograms) and the other is based on the information contained in the reconstructed standard images (Heismann et al., 2012).

On the other hand, it is possible to estimate two physical properties whose energy dependence is well known. By addressing the problem correctly, it is possible to create maps of density and atomic number from the measured data (Heismann et al., 2012).

The attenuation coefficient as a function of energy can be represented as the linear combinations of basis functions as presented in equation (16). In equation (16), $f_i(E)$ represents the material functions of energy and c_i its concentration (Heismann et al., 2012). Equation (16) is based on the mixture rule of the attenuation coefficient for chemical compounds (Hubbell, 1969).

$$\mu(E) = c_1 f_1(E) + c_2 f_2(E) + \dots + c_n f_n(E) \quad (16)$$

Equation (16) represents the attenuation coefficient as an expansion using n base functions, for an arbitrary n , the method is known as spectral energy decomposition, and as a specific case dual energy decomposition is obtained for $n=2$.

The attenuation coefficient has a spatial distribution and depends on the energy, $\mu(E, x, y)$. Applying the attenuation formula for poly-energetic radiation of equation (6), the resulting attenuation of both spectra is given by equation (17).

$$\begin{pmatrix} A_1 \\ A_2 \end{pmatrix} = \begin{pmatrix} \int_E w_1(E) \exp\left(-\int_L \mu(E, x, y) ds\right) dE \\ \int_E w_2(E) \exp\left(-\int_L \mu(E, x, y) ds\right) dE \end{pmatrix} \quad (17)$$

In this equation system, the energy dependence of the spectra $S_1(E)$ and $S_2(E)$ is contained in the weight functions $w_1(E)$ and $w_2(E)$ as defined in section 1.1.3.

Then, inserting the corresponding parameterization of the attenuation coefficient in the system of equations (17) it is possible to estimate the content of materials in the imaged object. The choice of the basis materials is empirical. Alvarez and Macovski (Alvarez et al., 1976) used the representing functions of Compton and photoelectric effect but for clinical applications, a set of functions representing materials of clinical interest is generally used. Pairs of materials of large clinical interest are iodine and calcium, or iodine and water (Marin, 2014).

1.3.1 Projection-Based BMD

This method uses the information contained in the projection data or sinogram (Heismann et al., 2012). Then, this is an algorithm performed before the reconstruction of the images. Returning to the equation system (17), inserting the two-material parameterization of equation (18), the equations system (19) is obtained.

$$\mu(E, x, y) = c_1(x, y)f_1(E) + c_2(x, y)f_2(E) \quad (18)$$

$$\begin{pmatrix} A_1 \\ A_2 \end{pmatrix} = \begin{pmatrix} \int_E w_1(E) \exp(-(f_1(E)C_1 + f_2(E)C_2))dE \\ \int_E w_2(E) \exp(-(f_1(E)C_1 + f_2(E)C_2))dE \end{pmatrix} \quad (19)$$

In equation (18), functions $c_i(x, y)$ contain the spatial information of the attenuation coefficient and the functions $f_i(E)$ contain the energy dependence. Then, in equation (19), C_1 and C_2 are defined as coefficient projections by the equation (20).

$$\begin{pmatrix} C_1 \\ C_2 \end{pmatrix} = \begin{pmatrix} \int_L c_1(x, y)ds \\ \int_L c_2(x, y)ds \end{pmatrix} \quad (20)$$

Hence, knowing the X-ray spectra, the detector sensibility, the basis material functions, and the measured attenuations, it is possible to calculate C_1 and C_2 by a nonlinear solution. Once having C_1 and C_2 , it is possible to reconstruct $c_1(x, y)$ and $c_2(x, y)$, using *Backprojection* reconstruction algorithms. C_1 and C_2 , as defined in equation (20), present the form of the projection integral defined in equation (1).

In the present work the functions $f_i(E)$ of equation (18) are the mass attenuation coefficients of specific materials. Then, $c_1(x, y)$ and $c_2(x, y)$ would represent the spatial distribution of the effective concentration of the materials. In this work, the spatial display of $c_1(x, y)$ and $c_2(x, y)$ are called as material concentration images.

Once we have the material concentration images, $c_1(x, y)$ and $c_2(x, y)$, it is possible to reconstruct monoenergetic images. Since not actual monoenergetic radiation was used to obtain the images, they are called virtual monoenergetic images. The monoenergetic images are easily reconstructed using equation (18) via the solution for $c_1(x, y)$ and $c_2(x, y)$ (material concentration images), and the known functions $f_1(E)$ and $f_2(E)$ (mass attenuation coefficients) at the energy of interest.

1.3.2 Image-Based BMD

This method uses the information contained in the reconstructed standard images obtained with each tube tension. Then, this is a method performed after the standard reconstruction of the images. The measured attenuations A (sinograms) generate two standard images $\bar{\mu}_i(x, y)$ for each energy spectrum. Then, it is possible to return to the dual energy treatment assuming that the two reconstructed images follow relation (11)

$$\bar{\mu}(x, y) = \int_E w(E) \mu(E, x, y) dE \quad (11)$$

Using equation (11) and expanding $\bar{\mu}_i(x, y)$ as equation (18), we obtain

$$\begin{pmatrix} \bar{\mu}_1(x, y) \\ \bar{\mu}_2(x, y) \end{pmatrix} = \begin{pmatrix} c_1(x, y) \int_E w_1(E) f_1(E) dE + c_2(x, y) \int_E w_1(E) f_2(E) dE \\ c_1(x, y) \int_E w_2(E) f_1(E) dE + c_2(x, y) \int_E w_2(E) f_2(E) dE \end{pmatrix} \quad (21)$$

This system can be written as

$$\begin{pmatrix} \bar{\mu}_1(x, y) \\ \bar{\mu}_2(x, y) \end{pmatrix} = K \begin{pmatrix} c_1(x, y) \\ c_2(x, y) \end{pmatrix} \quad (22)$$

where the matrix elements of K are defined as

$$K_{i,j} = \int_E w_i(E) f_j(E) dE \quad (23)$$

Finally, the coefficients $c_1(x, y)$ and $c_2(x, y)$ are estimated by equation (24), where $T = K^{-1}$.

$$\begin{pmatrix} c_1(x, y) \\ c_2(x, y) \end{pmatrix} = T \begin{pmatrix} \bar{\mu}_1(x, y) \\ \bar{\mu}_2(x, y) \end{pmatrix} \quad (24)$$

1.3.3 Density and Atomic Number Reconstruction

This is a method performed after the standard reconstruction of the images. The method performs the differentiation using the reconstructed standard images. As previously explained, using DECT measurements, it is possible to reconstruct spatial information from functions that have energy dependence. In this case, the properties to be reconstructed are density ρ and atomic number Z , (Heismann et al., 2012).

Equation (25) shows the parameterization used to estimate ρ and Z , with the constants $\alpha, \beta = 0.02 \text{ kg/cm}^3$, $k=3, L=3$.

$$\mu(E) = \rho \left(\alpha \frac{Z^k}{E^L} + \beta \right) \quad (25)$$

Using the approximation of equation (11), it is possible to write the system as

$$\begin{pmatrix} \bar{\mu}_1(x, y) \\ \bar{\mu}_2(x, y) \end{pmatrix} = \rho(x, y) \begin{pmatrix} \int_E w_1(E) \left(\frac{\mu}{\rho} \right) (E, Z(x, y)) dE \\ \int_E w_2(E) \left(\frac{\mu}{\rho} \right) (E, Z(x, y)) dE \end{pmatrix} \quad (26)$$

where $\bar{\mu}_i(x, y)$ and $w_i(E)$ represent, respectively, the pixel measurements and the weight functions, as in the previous section.

Substituting (25) in (26), the equation system can be written as

$$\begin{pmatrix} \bar{\mu}_1(x, y) \\ \bar{\mu}_2(x, y) \end{pmatrix} = \begin{pmatrix} \beta & g_1 \\ \beta & g_2 \end{pmatrix} \begin{pmatrix} \rho \\ \rho Z^k \end{pmatrix} \quad (27)$$

where the matrix elements are defined as

$$g_i = \alpha \int_E \frac{w_i(E)}{E^L} dE \quad (28)$$

The solution of the equations system (27) is

$$\begin{pmatrix} \rho \\ \rho Z^k \end{pmatrix} = \frac{1}{\beta(g_2 - g_1)} \begin{pmatrix} g_2 & -g_1 \\ -\beta & \beta \end{pmatrix} \begin{pmatrix} \bar{\mu}_1 \\ \bar{\mu}_2 \end{pmatrix} \quad (29)$$

and the specific solutions for ρ and Z are

$$\rho = \frac{1}{\beta} \frac{g_2 \bar{\mu}_1 - g_1 \bar{\mu}_2}{(g_2 - g_1)} \quad (30)$$

and

$$Z = \left(\frac{\beta(\bar{\mu}_2 - \bar{\mu}_1)}{g_2 \bar{\mu}_1 - g_1 \bar{\mu}_2} \right)^{\frac{1}{k}} \quad (31)$$

The presented algorithm has the limitations of the expression (11) approximation (Heismann et al., 2012).

2 MATERIALS AND METHODS

This chapter is organized into five sections which present the methodology and materials used in the present work. This work intends to simulate the image acquisition process of the DECT equipment GE Discovery CT 750 HD. To do so, the PENELOPE/PenEasy Monte Carlo code (Salvat et al., 2011; Sempau et al., 2011) was used.

The Discovery CT 750 HD device was chosen because of the possibility of comparison of both, simulated images and images obtained in the real device. The real machine is installed on the Institute of Radiology of the School of Medicine of the University of São Paulo¹. Figure 19 presents a scheme of the sections and a summary of the objectives and methods which are presented in this chapter.

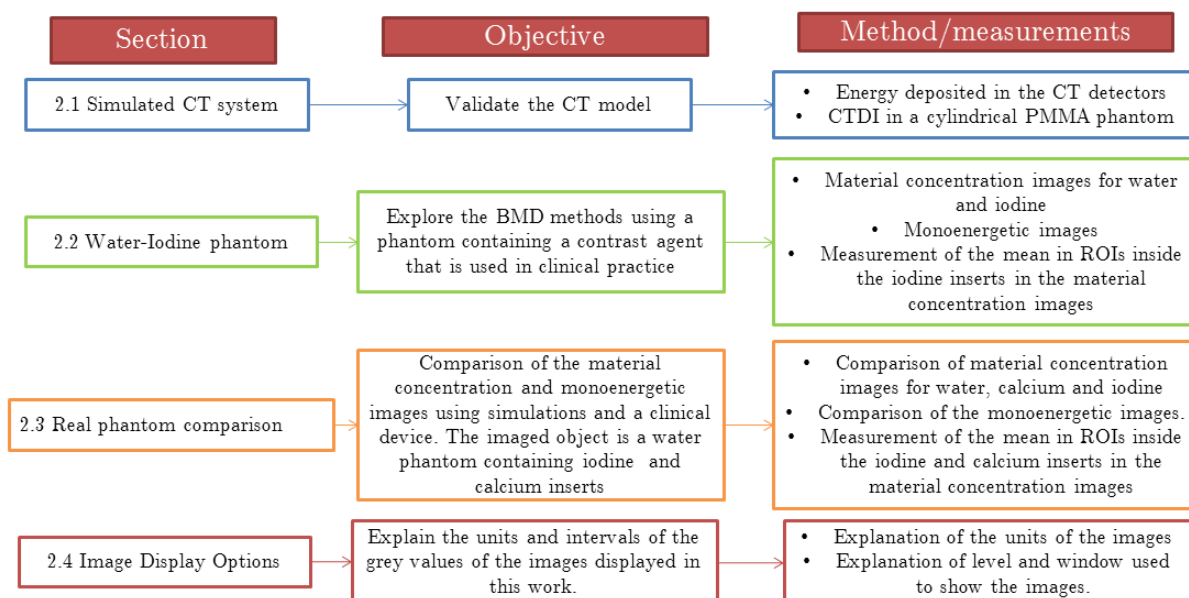


Figure 19. Scheme representing the sections of this chapter, the objectives and main methods implemented in each section. Sections 2.1 and 2.2 present the methodology of the simulations performed. The only section that presents the methodology concerning measurements in a real CT device and simulations is the 2.3. Section 2.4, explains the exhibition units and intervals of the images presented in this work.

First, the CT components and features were simulated, and some parameters derived from the model were compared with values present in the literature. Such comparative methodology is presented in section 2.1. The methodology is based on the analysis of the energy deposited in the CT detectors and the assessment of the CTDI.

In order to explore the main differences of the material decomposition methods, a water phantom containing inserts of iodine contrast agent was simulated. The

¹ Research Project 099/2017, approved on October 18, 2017 by the Department of Radiology and Oncology of the School of Medicine of the University of São Paulo

phantom contained three concentrations of iodine distributed in six cylindrical inserts of different sizes. The methodology used to analyse the images of the phantom is described in section 2.2.

Additionally, a real phantom designed to accommodate inserts of different materials was prepared to be imaged and an equivalent system was simulated. The phantom contained iodine and calcium inserts. Section 2.3 describes the procedures used to acquire and analyse the real and simulated images of the phantom.

Finally, section 2.4 presents the notation used to display the grey values of the images. The section also explains the display options of each type of image: Standard CT images, material concentration images and virtual monoenergetic images.

Terminology adopted to name the acquired images

A diagram summarizing the acquisition and reconstruction processes of the images presented in this work is shown in Figure 20. Sections 2.1 and 2.2 describe the simulation process of the image acquisition. Then, as such images are obtained from simulation, to clarify the terminology the word “simulated” is added to the name of the images, for example “simulated standard images”.

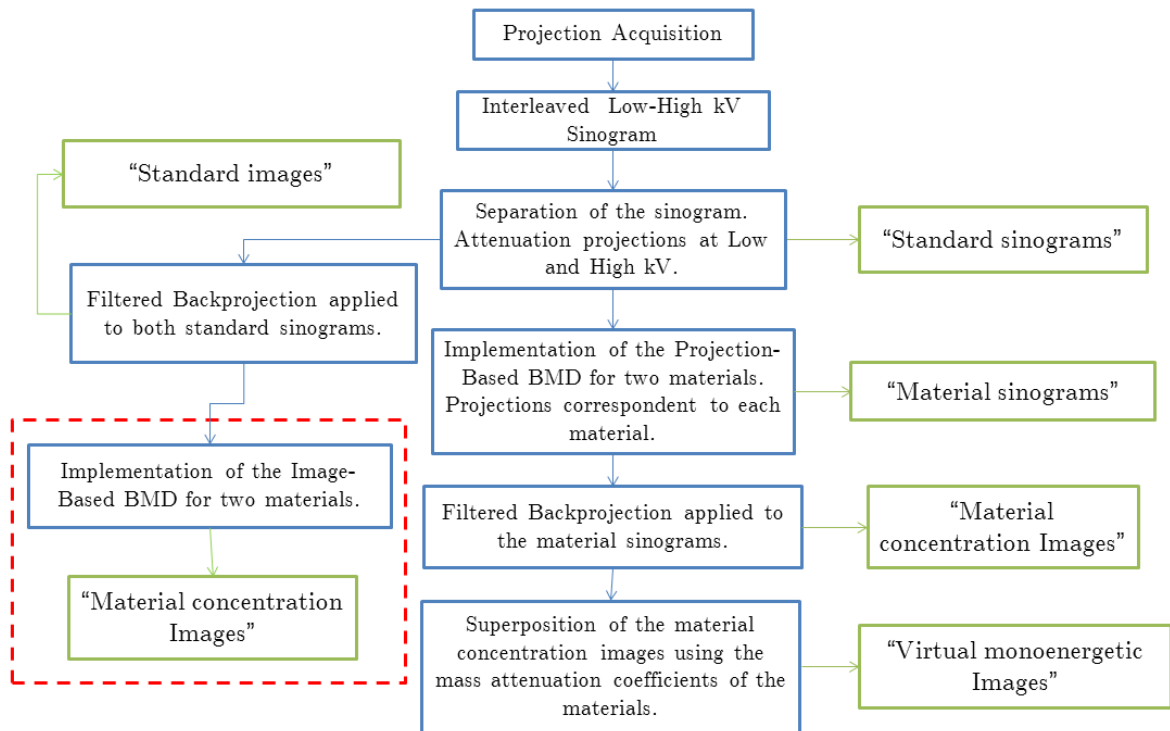


Figure 20. Summarized image reconstruction processes of the images used in the present work. The name of the images and sinograms obtained after each reconstruction are presented inside the green boxes. Detailed information about the acquisition process and reconstruction is found in section 1.3 and in Figure 16. Almost all the scheme is referred to the Projection-Based BMD of section 1.3.1. The box enclosed by the discontinuous red line represents processes correspondent to the Image-Based BMD of section 1.3.2.

In section 2.3, the acquisition process of images in a real device is presented as well as the simulation of an equivalent system. In this case, the images obtained from the real device include the word “real” in their names, as for example “real standard images”. In general, in the present work the labels “simulated” and “real”, in the image names, parameters and quantities, indicate whether they were obtained from simulations or experimentally in the real DECT equipment.

Monte Carlo simulations

As previously mentioned, the simulations were performed using the Monte Carlo radiation transport code PENELOPE/penEasy (Salvat et al., 2011; Sempau et al., 2011). PENELOPE performs Monte Carlo simulates photon, electrons positrons transport in arbitrary materials and complex quadric geometries. Photon interactions (Rayleigh scattering, Compton scattering, photoelectric effect and electron-positron pair production) and positron annihilation are simulated in a detailed way.

Figure 21 schematizes the simulations performed.

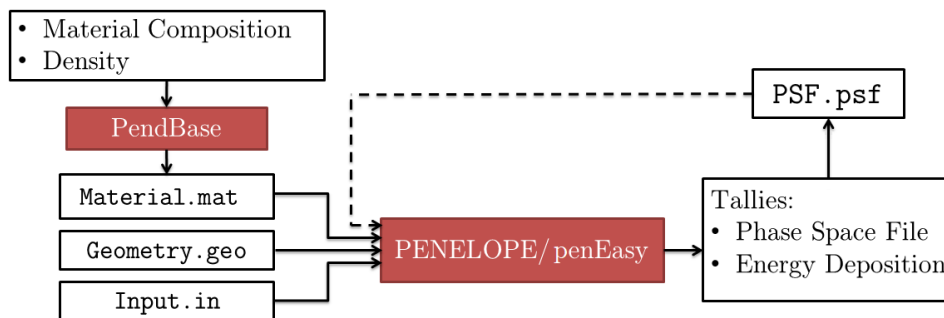


Figure 21. Schematic representation of the simulation process using PENELOPE/penEasy.

Each simulated material required being defined using the `material.exe` program and the `PendBase` database. To do so, it is important to know their chemical composition and the density. `material.exe` produces files, such as `material.mat`, which store the information necessary to simulate the transport of particles in such material.

The file `Geometry.geo` contains the spatial distribution of the materials of the simulated objects. Using quadric surfaces, space regions are defined as “bodies”. To each body, a numeric material identifier is assigned.

The file `Input.in` defines the parameters for the simulation such as the kind of particle, the energy distribution of the simulated particles, the number of initial particles to simulate and defines the tallies that are activated, among others. The number of initial particles is also called ‘number of histories’. The `Input.in` file also

correlates the material identifier of the geometry file with actual material files as `material.mat`.

Using the input files described in the last paragraphs, the PENELOPE/penEasy Monte Carlo code simulates the transport of photons, electrons and positrons through the defined system, and calculate the desired tallies (Salvat et al., 2011; Sempau et al., 2011). The tallies refer to the quantities that are estimated during the simulation. Figure 21 shows the most-used tallies during this work: Energy Deposition and Phase Space File (PSF).

The tally “energy deposition” reports the energy deposited per history in each material. The tally “PSF” generates a `PSF.psf` file containing the information of the particles entering (or created inside) a predefined material. The `PSF.psf` is used as input for subsequent simulations. In the present work, the material used to create the PSF is a perfect absorber. This assumption was taken to optimize computation time.

Another important remark for the simulations was the use of the servers available in the Group of Radiation Dosimetry and Medical Physics of the Department of Nuclear Physics of the Institute of Physics/USP. The simulations were performed on the computer servers due to the possibility of parallelizing the simulations. The main features of the servers are presented in Table 3.

Table 3. Main features of the servers available in the Group of Radiation Dosimetry and Medical Physics of the University of São Paulo.

Name	Processor	Number CPUs	RAM
WSDOSM	Intel(R) Xeon(R) CPU E5-2420 1.9 GHz	10	8 GB
WSDOSB	Intel(R) Xeon(R) CPU E3-1270 3.5 GHz	7	8 GB

2.1 Modelled CT system

The modelled CT system attempts to represent the geometrical characteristics of a DECT scanner, which works with rapid kV switching. The simulated device intends to preserve the features of the Discovery CT 750 HD (GE Company, 2011). The Discovery CT 750 HD equipment acquires two sinograms simultaneously. Figure 16 illustrates a sequential scheme of its acquisition process. The specifications of the actual device and the modelled CT are shown in Table 4. Such characteristics led to the simulated geometric arrangement shown in Figure 22.

The maximum field of view in Table 4 is different for both CT systems. In this case the modelled CT has a smaller FOV due to the intention to irradiate phantoms of 16 cm diameter and to optimize the detector signal.

Table 4. Characteristics of the GE Discovery CT 750 HD device (GE Company, 2015), and the modelled CT.

Feature	Actual device	Modelled CT
Focus to detector distance (cm)	95	95
Focus to isocenter distance(cm)	54.1	54.1
Maximum System FOV (cm)	50	19.1
Rotation times (s)	0.4–2.0	Not applicable
Target angle (°)	7	7
Target material	Tungsten–Rhenium	Tungsten

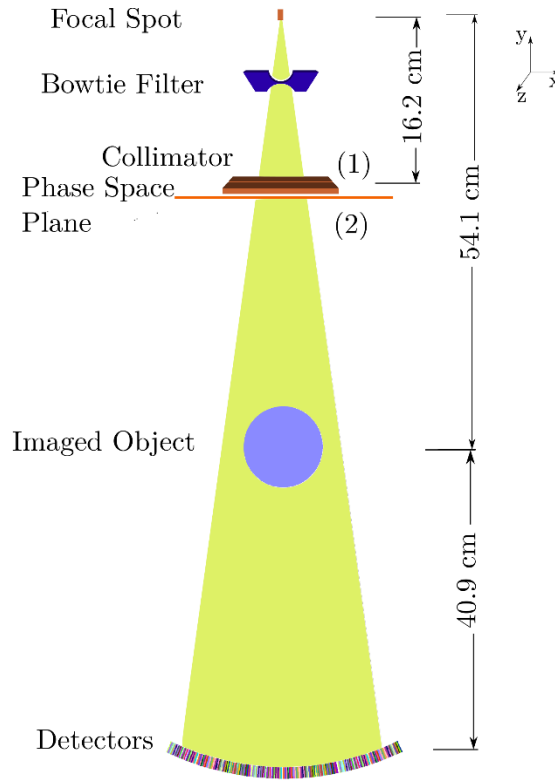


Figure 22. Scheme of the components of the modelled CT device, (1) depicts the elements of the source before the phase space plane (2) depicts the imaged object and the detector array.

As Kim et al. (Kim et al., 2013), the entire CT simulation was divided into two stages. Each stage corresponds to the regions (1) or (2), as indicated in Figure 22. The first stage corresponds to the simulation of the radiation interaction with the source elements (focal spot material, bowtie filter and collimator). The second stage is related to the simulation of the radiation interaction with the imaged object and detectors. The idea of dividing the simulation into two stages intends to optimize the computation time. In the present work, stage 1 was computed once for each energy spectrum. Then, the resultant particles of stage 1, which were stored in the PSF, were used multiple times to compute the CT projections.

In order to create the phase space files, a phase space plane was defined after the collimator, as shown in Figure 22. The information of the particles stored in the PSF is shown in the following list:

- KPAR type or particle (1=electron, 2=photon, 3=positron)
- E energy (eV)
- X, Y, Z position coordinates (cm)
- U, V, W direction cosines
- WGHT statistical weight
- ILB(1)-ILB(5) set of indices with information about how the particle was created
- NSHI difference between the shower numbers of the present particle and the one preceding

For further information of the parameters the PENELOPE, the authors recommend the PENELOPE/penEasy user manuals (Salvat et al., 2011; Sempau et al., 2011).

Other important parameters of the simulation are the absorption energies. Particles with energies less or equal than the defined absorption energy would be absorbed in the material. These energies were defined in the `input.in` file for each simulated material. For the components of the modelled CT system the absorption energies were:

- Bowtie filter = $E_{\text{abs}}(e^-)=150\text{keV}$, $E_{\text{abs}}(\text{ph})=1\text{keV}$
- Phantom: $E_{\text{abs}}(e^-)=E_{\text{abs}}(\text{ph})=1\text{keV}$
- Collimator: $E_{\text{abs}}(e^-)=E_{\text{abs}}(\text{ph})=1\text{MeV}$
- Detectors: $E_{\text{abs}}(e^-)=150\text{keV}$, $E_{\text{abs}}(\text{ph})=150\text{keV}$

Then, the radiation transport in the collimator and detectors is not simulated as the simulated particles have energies lower than the absorption energies. In the bowtie filter just the transport of photons is simulated, electrons transport is not simulated. In the phantom, the transport of both electrons and photons is simulated.

2.1.1 Source Model

The CT geometrical model described by Dixon et al. (Dixon et al., 2005) was adopted. Dixon described the geometrical characteristics of a GE LightSpeed, which is similar to the GE Discovery CT 750 HD.

As previously mentioned, the source model was composed of the focal spot, the bowtie filter and the collimator. In the following paragraphs, the characteristics of each of these elements are explained.

Focal Spot

The focal spot is the region where the photons are emitted in the simulation. As suggested in Figure 22, the focal spot was localized at 54.1 cm from the CT axis of rotation. The photon emission occurred in a line inside the anode material to consider the effect of the auto attenuation of photons inside the target in an real X-ray tube.

In the present work, the interaction of the electrons with the target material in the X-ray tube was not simulated using the PENELOPE code. The energy distributions of the photons were obtained using the modified TBC model (Costa et al., 2007). This model is based on the original TBC semi-empirical model (Tucker, 1991) for a tungsten target. The TBC model takes into account *bremsstrahlung* and characteristic X-ray production. The spectra obtained with the modified TBC model are the input spectra for the simulations. The energy distribution of the input spectra determines the energy of the particles that the code randomly sorts.

Apart from the operation voltages (80 kV and 140 kV), there was no available information about the energy spectra of the device Discovery CT 750 HD to compare with the spectra obtained from the modified TBC model. For that reason, the TBC spectra were compared to the spectra measured in a GE Discovery PET/CT 690. The measurement of the spectra was performed by Professor Dr. Ricardo Terini, collaborator of the Group of Radiation Dosimetry and Medical Physics. The spectra were measured using a Compton spectrometer. Such spectrometry modality reconstructs the original spectrum using the X-rays scattered incoherently by a material bar, as described by Vieira et al. (Vieira et al., 2011).

Spectra of 80, 100, 120 and 140 kV were compared. The measured spectra were obtained without a bowtie filter, which was adequate because it avoided the angular dependence of the energy distribution generated by the shape of the filter. Then, it was possible to directly compare the measured spectra with the outputs of the TBC model. For each tube voltage, TBC spectra were generated using aluminium additional filters of 4, 6, 8, and 10 mm.

After normalization, the spectra were compared for all filtrations (4, 6, 8, 10 mm Al). It was decided that the TBC spectra most similar to the measured ones were the ones obtained with filtration of 6 mm of Al. The TBC and the Discovery PET/CT 690 spectra for 140 kV are shown in Figure 23.

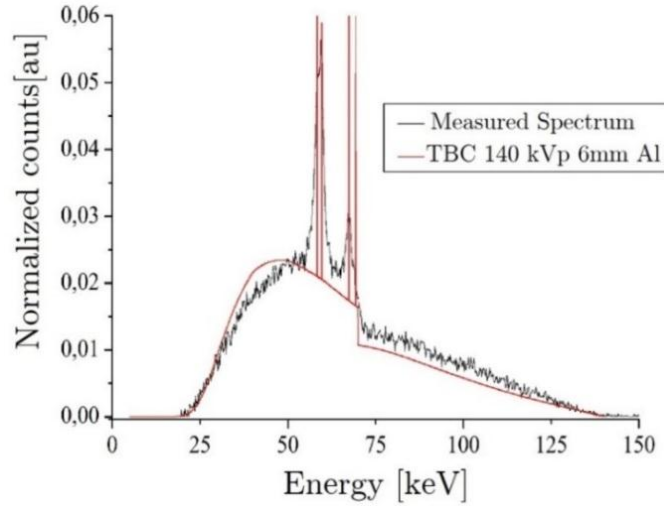


Figure 23. Measured spectrum and spectrum obtained using the modified TBC model for a tube voltage of 140 kV. The measured spectra were available thanks to the courtesy of Dr. Ricardo Terini.

Therefore, the 80 and 140 kV spectra used in the present work are the ones obtained with the same 6mm Al additional filtration. The assumption of using the same filter for both spectra was coherent considering the Discovery CT 750 HD device, in which both spectra are produced using the same X-ray tube while rapidly switching the tube voltage. Table 5 presents some features of the spectra like HVL and effective energy. Such features are also outputs of the computer program which calculates the TBC spectra (Costa et al., 2007).

Table 5. Features of the used spectra, such spectra are used as input for the simulations.

Tube Voltage (kV)	Additional filtration (mm Al)	HVL (mm Al)	Effective energy (keV)
80	6	5.45	48
140	6	7.69	62

Bowtie Filter

As shown in Figure 22, the bowtie filter is positioned between the focal spot and the collimator. The technical information found about the CT machines did not include detailed specifications about its dimensions and material. The bowtie filter was simulated as being a truncated rectangular pyramid of aluminium with two cylindrical sections removed. Figure 24 presents the geometry and dimension of the bowtie filter adopted in the present work.

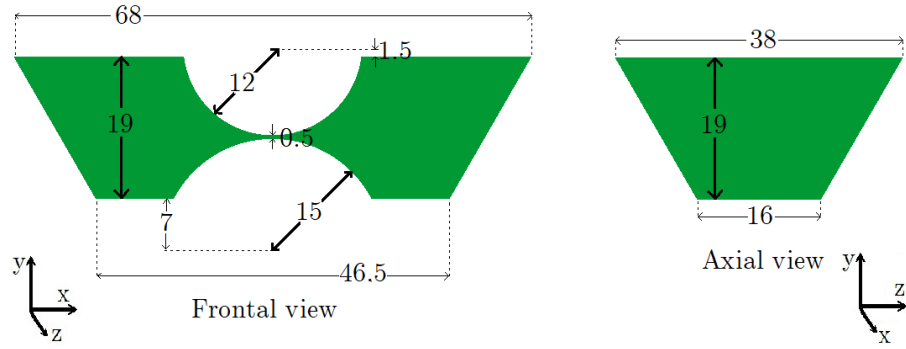


Figure 24. Design of the simulated bowtie filter, all the presented dimensions are in millimetres. The simulated bowtie filter material was aluminium.

As the geometry and material were assumed, the only missing variable was the relative position of the bowtie filter. It must be localized between the focal spot and the collimator. As shown in Figure 22, the distance between the focal spot and the collimator is 16.2 cm. To find the better filter position, 15 PSFs of 10^9 initial histories were generated varying the position of the bowtie filter (between the focal spot and collimator) in steps of one centimetre. Then two steps were performed to find the better position of the filter:

1. The different PSFs generated for each bowtie filter position were used to simulate the irradiation of a cylindrical water phantom and calculate the energy deposited in the detector array. As discussed before (section 1.1.2), the bowtie filter attempts to homogenize the energy deposited in the detectors. The aim was to find the position of the bowtie filter that improves the homogenization of the energy deposited in the detectors (belonging to the phantom shadow) when a water phantom was irradiated. Figure 25 presents the detectors covered by the phantom and the most external (or outer) detectors that belong to the phantom shadow. The three outer detectors, which belong to the shadow of the phantom, were studied as they exhibit the greatest variations of deposited energy due to the filter geometry. The process was performed using a 16 cm diameter cylindrical water phantom.
2. Using the PSFs correspondent to the best positions found with the first step, the Computed Tomography Dose Index (CTDI) (ICRP, 2007; McCollough et al., 2011) was calculated from simulations in a PMMA cylindrical phantom of 16 cm diameter. A modelled CTDI phantom is shown in Figure 26. The energy deposited was assessed in five cylindrical regions, with 10 cm length and 0.8 cm diameter: one at the centre and four at 1 cm from the cylindrical surface. The methodology used consists in computing the material Kerma (in this case PMMA Kerma) and then assess the air Kerma to compute the $CTDI_{100}$ and compare with the simulated results of Kramer et al. (Kramer et al., 2017).

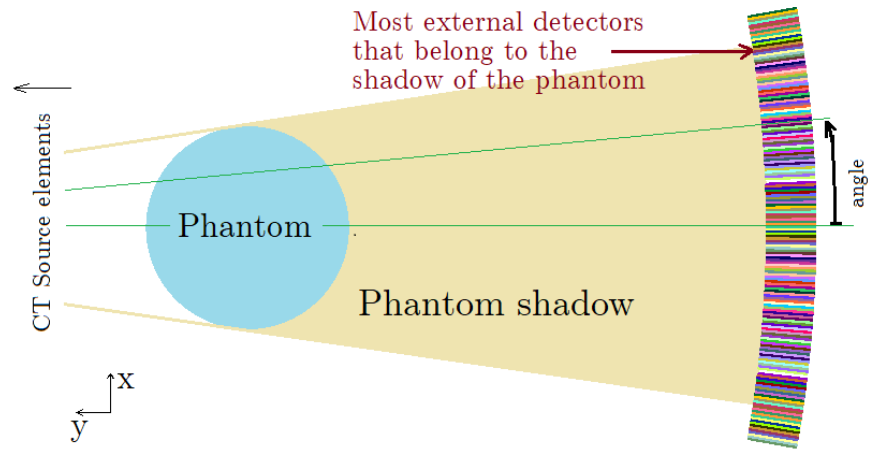


Figure 25. Representation of the geometric arrange used to study how the bowtie filter affects the energy deposited in the detectors. The energy deposited in the detectors belonging to the phantom shadow was analysed while the bowtie filter position was varied, especially the energy deposited of the outer or most external detectors (red arrow). The angle of the detector is measured with respect to the central line that passes through the centre of the detector arrangement. The green lines present the angle of a specific detector. This figure presents just the phantom and the detectors, the entire geometric model is found in Figure 22.

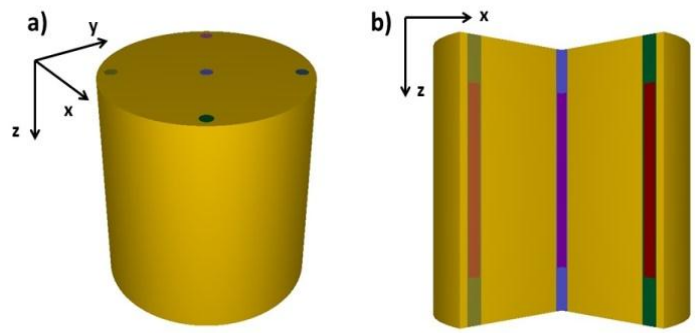


Figure 26 (a) CTDI cylindrical phantom used to compute the $CTDI_{100,c}$ at the centre and $CTDI_{100,p}$ at the 4 positions at 1 cm from the surface; (b) 3D view showing the cylindrical bodies with 10 cm length and 8 mm of diameter used to compute the CTDI.

Collimator

The collimator consisted of a pair of lead plates, positioned at 16.51 cm from the focal spot; they are 0.25 cm width and have an aperture of 0.8 cm to create a 1 cm projection length on the central axis. The collimator was simulated as a perfect absorber. Therefore, any photon reaching the collimator is totally absorbed. This assumption is consistent with the collimators adopted in real CT machines.

Detectors

The detectors were also simulated as being perfect photon absorbers. In other words, all the energy of the photons which reach the detector surface is absorbed. The perfect absorber assumption was taken to save computational time and to avoid the detectors crosstalk. In other words, to avoid the photons that reach a detector after

depositing energy in another adjacent detector. This assumption is consistent with the high efficiency of the CT detectors used in modern equipment.

An important feature of the detector simulation was the necessity of the definition of each detector as an independent material. The tally `Energy-Deposition` returns the energy deposited in each material defined for the simulation. Then, to generate the sinogram, each simulated detector element needed to be defined as an independent material. The PENELOPE parameter `MAXMAT` controls the number of materials allowed for a PENELOPE simulation. Its default value was `MAXMAT=10`. Then, it was necessary to increase `MAXMAT`, to a number that allowed the CT detectors simulation. An upper limit of `MAXMAT` was found at `MAXMAT=300`. Thus, the limitation of `MAXMAT` also limits the number of detectors. Additionally, the simulation of a large the number of materials requires more computational memory and makes the simulation slower.

For the simulations presented in this work, the detector element angle was 0.1125° (twice the size of a detector of the real device) and the total irradiated angle was selected to cover 20.25° . The selected angles permitted the simulation of the image acquisition of cylinders of 16 cm diameter, the standard size of head phantoms.

Once the modelled CT model was completely defined, there was undertaken a study of image parameters CNR and SNR as function of the number of initial simulated histories. Such study is too long to be included in the main text. Then, it is presented in Appendix A, and its methodology is described in section A.1.

2.1.2 Acquisition of the projections

As explained in section 1.1.3, the angular projections are necessary to obtain the CT images. In the simulation process, the projections were defined as the energy deposited in the detectors when imaging an object, divided by the energy deposited in the detectors of air scan (scan obtained without imaging object), similar to I/I_0 in equation (5).

To obtain the projections, the PSFs found in section 2.1 for 80 and 140 kV were used. As mentioned above, the idea was to simulate a device working with rapid kV switching. It meant that for each CT projection, one of each spectrum was used. It generated an interleaved sinogram, which contained the projections corresponding to the high and the low energy spectrum as presented in Figure 16. The interleaved sinogram was then split generating a sinogram for each energy spectrum.

Then, each projection was obtained running a simulation at a specific angle and for the corresponding spectrum. To manage a large number of simulations (720 per CT

image), a Matlab® routine (R2015a, The Math Works Inc., Natick, MA, 2015) was created. Such routine automatically parallelized multiple simulations and managed the output files of the simulation.

Once the sinograms were obtained, the standard CT images were reconstructed using the filtered *Backprojection* algorithm described in section 1.1.3. The beam geometry adopted in the modelled CT was a fan-beam. Then, the Matlab® function used to perform the FBP with fan-beam geometry is the “ifanbeam”. The reconstructions using the function ifanbeam were performed using the default mathematical filter Ram–Lak.

The real device possesses various filters to perform the images reconstruction, for the “normal” and GSI modes three filter are available: soft, standard and detail (Zhang, 2011). For the images obtained in the real device the filters used in the reconstruction were standard. The Discovery CT 750 HD also has different tools of post-processing such as MARs (Metal Artefact Reduction software), ASIR (Adaptive Statistical iterative Reconstruction) that can be used in the GSI mode to reconstruct material or monoenergetic images (Lee, 2012; Fuchs, 2013). Such tools weren’t implemented in the reconstruction of the real images.

To perform the BMD, a script written in Matlab® implemented both, Projection–Based BMD and Image–Based BMD as described in section 1.3. To do so, the equations presented in sections 1.3.1 and 1.3.2 were implemented after converting the integrals into sums.

Calibration of the images in Hounsfield Units

A calibration using the phantom Catphan 600 (The Phantom Laboratory, 2014) was performed to calibrate the HU obtained in the standard images. For such calibration, images at 80 kV and 140 kV were acquired in the device Discovery CT 750 HD at the InRad.

Equation (32) presents the linear function used to calibrate the images. HU_s represents the data of the simulated standard images, and h_l the parameters of the calibration. The parameters obtained from the calibration for each spectrum are presented in Table 6. Such parameters were used to calibrate the standard images of the present work.

$$HU_c = h_l \cdot HU_s \quad (32)$$

Table 6. Parameters obtained from the calibration of the HU using the phantom Catphan 600.

Spectrum	h_I
80 kV	1.77±0.10
140 kV	1.69±0.10

2.2 Water–Iodine phantom

To study the differentiation capabilities of the DECT methods, a water phantom containing three iodine concentrations was simulated. The simulated phantom is shown in Figure 27. It consists of a 16 cm diameter water phantom containing three inserts of iodine of 2 cm diameter and three inserts of iodine of 1 cm diameter. The simulations were done using 10^9 histories.

To simulate the iodine inserts, the chemical composition of the commercial iodine contrast Ultravist® 300 (Bayer, 2012) was used. Ultravist® 300 contains iopromide ($C_{18}H_{24}I_3N_3O_8$) as active ingredient. Each millilitre of Ultravist® 300 contains 623 mg of iopromide, equivalent to 300 mg iodine (Bayer, 2012).

Three concentrations of iodine were simulated: I-45, I-30 and I-15. These names are related to the equivalent content of iodine; for example, the I-30 insert contains 30 mg of iodine per cubic centimetre of solution. The geometric distribution of the inserts is shown in Figure 27. The composition of the solutions were obtained supposing the Ultravist® 300 diluted in pure water. The chemical features of each material are shown in Table 7. Detailed information is presented in Appendix B.1.

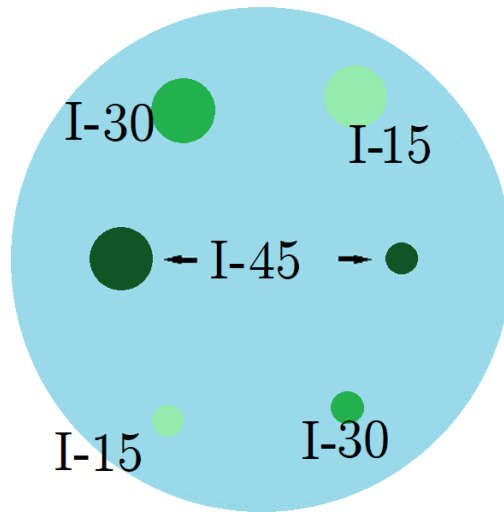


Figure 27. Representation of the iopromide distribution in the water phantom, water is placed in the blue region and the iodine concentrations in the green ones. Three concentrations of iodine were simulated, I-45 mg/cm³, I-30 mg/cm³ and I-15 mg/cm³ and two cylinder sizes, 1 and 2 cm diameter.

Table 7. Chemical features of the dilutions contained in the simulated phantom of Figure 27.

Label	Density (g/cm ³)	Iodine concentration (mg/cm ³)
I-45	1.0495	I 45
I-30	1.0330	I 30
I-15	1.0165	I 15

As described in section 2.1.2, the projections were obtained using 80 kV and 140 kV spectra and the standard simulated images were reconstructed by means of the FBP algorithm available in Matlab®. The material images were reconstructed using Projection-Based BMD and Image-Based BMD methods described in sections 1.3.1 and 1.3.2. The materials used to perform the BMD were water and iodine. The energy dependence of both mass attenuation coefficients of water and iodine is shown in Figure A-2. From the material concentration images, monoenergetic images were generated following the theory presented in section 1.3.1. Finally, the mean values in the inserts were computed and compared.

A calibration was performed analysing the linearity of the grey values of the material concentration images. The calibration will be used in the concentration images obtained with the real phantom described in the next section.

2.3 Real phantom comparison

A final set of simulations was performed in order to evaluate the similarity of the results obtained in a real CT and in the modelled CT. The real and simulated devices are shown in Figure 28. A physical CT phantom (Costa, 1993) was prepared to be imaged and a similar geometry was simulated. The phantoms are shown in Figure 29.

The concentrations of the inserts in the phantom were selected to be similar to those used in the dedicated DECT phantoms, with iodine concentration from 2 to 20 mg/ml and calcium concentration from 50 to 600 mg/ml (Gammex, 2015). Both real and simulated phantoms are presented Figure 29, in which is possible to see the labels A-F indicating each material. The features of the materials in the inserts are presented in Table 8.

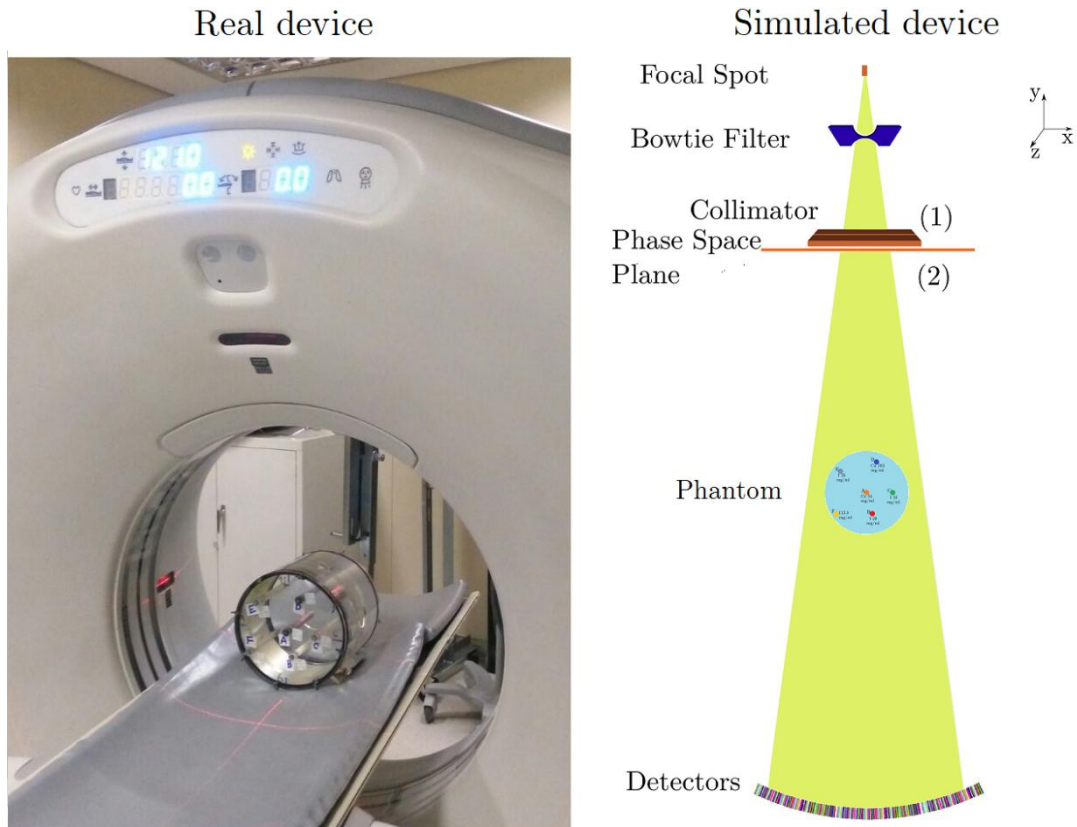


Figure 28. Left: Real device with the phantom positioned in the centre on the gantry CT. Right: modelled CT system.

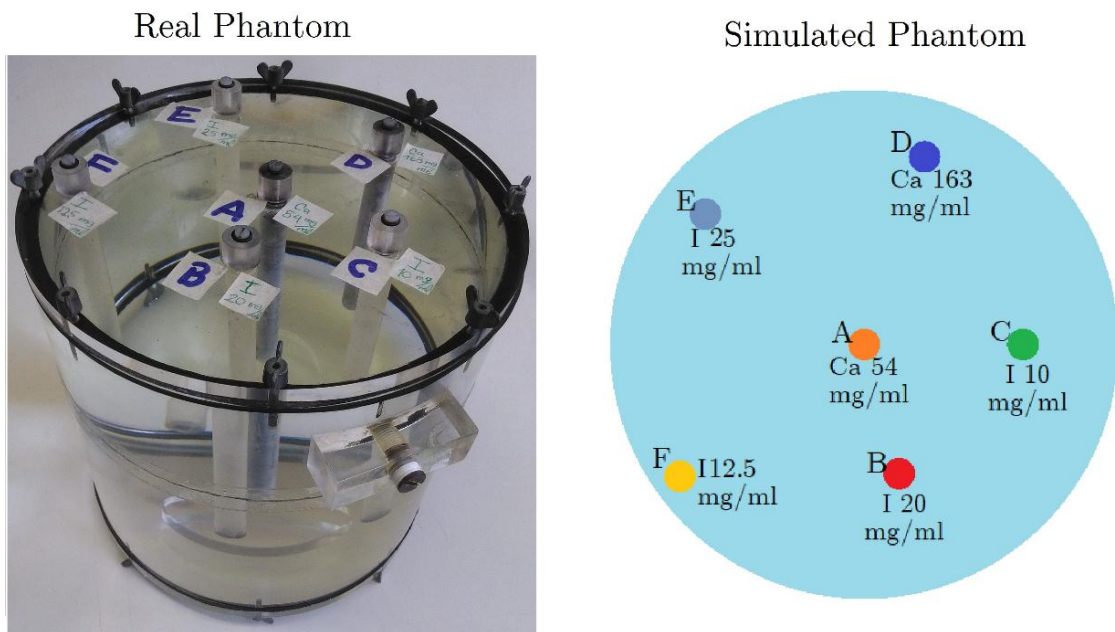


Figure 29. Real phantom (Costa, 1993) and its equivalent simulated phantom. The inserts are placed in a water phantom. The labels A-F represent each material and its composition as in Table 8.

The mixtures of iodine were prepared mixing Ultravist® 300 and saline solution (distilled water with sodium chloride in a concentration of 9 mg/ml). The solutions were mixed in a beaker. The cylindrical inserts of the phantom were slowly filled using

a pipe to avoid the formation of bubbles. Further information on the composition is found in Appendix B.2.

Table 8. Material density and element concentration of the phantom cylinders. The Labels presented coincide with the ones shown in Figure 29. The Short Name column presents the names used for future reference.

Label	Short Name	Density (g/cm ³)	Concentration
A	Ca-54	0.52±0.05	(54 ± 5) mg/cm ³ of Ca
B	I-20	1.03±0.04	(20 ± 1) mg/cm ³ of I
C	I-10	1.02±0.04	(10.0 ± 0.4) mg/cm ³ of I
D	Ca-163	0.90±0.06	(163 ± 11) mg/cm ³ of Ca
E	I-25	1.03±0.04	(25 ± 1) mg/cm ³ of I
F	I-12.5	1.02±0.04	(12.50 ± 0.5) mg/cm ³ of I

The calcium inserts were prepared as combinations of commercial CaCO₃ (Carbonates, 2015) and carbon black (Anastacio, 2017). To fill the phantom cylinders, the components were mixed and then the resulting powder was manually compressed while filling the cylinders. Additional information on the composition is found in Appendix B.2.

The real phantom (Figure 29) has a radius of 10 cm, and cavities of 1 cm diameter. The PSFs were previously generated to image an object of 8 cm of radius. This restricts the size of the simulated phantom. Then, the simulated inserts also had a diameter of 1 cm, but the position of the inserts E and F (Figure 29) were adjusted to fit in an 8-cm phantom.

2.3.1 Features of the acquired images

The CT device GE Discovery CT 750 HD works as a standard CT device and the dual energy mode can be activated selecting the GSI acquisition option. Figure 30 represents the scan modes and the type of images that were acquired in such device. Both GSI and standard images were acquired in axial mode.

The GE Discovery CT 750 HD was adjusted to acquire images of four slices of the phantom. Each slice covered 5 mm of the phantom. Then, for quantitative analysis of the images, such as measurements of mean CT number and standard deviation, the quantities were measured in each image of the four slices and quantities presented in this work were derived from the four measurements.

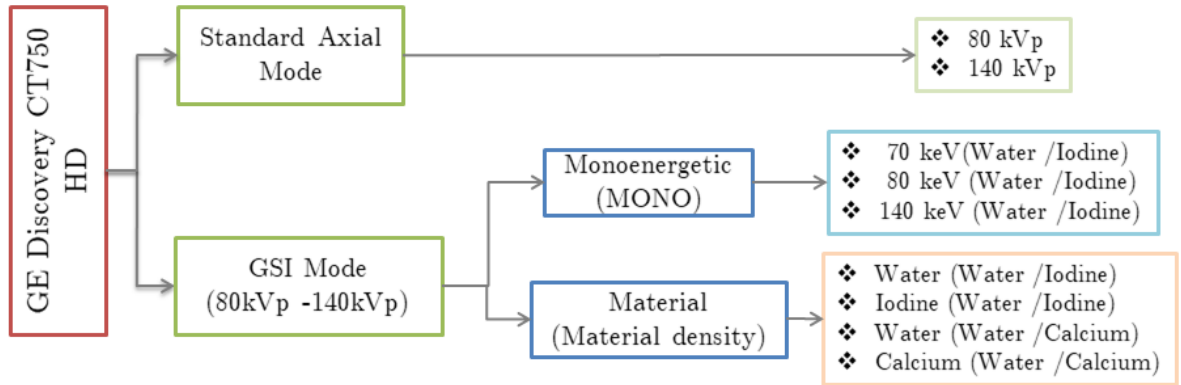


Figure 30. Acquisition modes and type of images acquired in the GE Discovery CT 750 HD. For the Monoenergetic and the Material images, the pairs of materials between parentheses represent the materials used to perform the BMD method.

The simulations performed with the phantom of Figure 29 were intended to generate images equivalent to the images acquired with the GE Discovery CT 750 HD (Figure 30). As the real device, the simulated images were reconstructed using just the Projection-Based BMD algorithm.

Standard images were acquired for 80 kV and 140 kV in the real device. Simulated standard images were also reconstructed for each sinogram, and a qualitative comparison of the pairs of standard images was done.

The pairs of materials available in the device are water-iodine and water-calcium. As the phantom includes water and inserts of calcium and iodine, the material images were obtained using the pairs of materials available in the device.

Monoenergetic images were also generated from the material concentration images of water and iodine, as presented in section 1.3.1. CNR was studied as function of the energy of the monoenergetic image. CNR was measured in each insert and for each energy following equation (14). For these measurements the background was a water region inside the phantom.

2.4 Image display options

In the present work the standard and monoenergetic CT images will be presented using the standard units used in CT, the Hounsfield Units. The raw reconstructed images obtained using FBP (section 1.1.3) represents the spatial distribution of $\bar{\mu}(x,y)$ as in equations (11) and (12). Such $\bar{\mu}(x,y)$ are converted to HU units as presented in section 1.1.4, and then the calibration presented in Table 6 was applied.

Once the images are presented in HU, the level (L) and window (W) are used to the display the range of HUs shown in an image. The level and window are commonly presented as L/W. The level indicates the central value of the range and the window

the half range. For example, if an image is displayed using HU values from -1000 to 2000 the level will be 500 HU and the window 1500 HU, this can be presented as L/W: 500 HU/ 1500 HU (Schlomka et al., 2008).

Material concentration images

On the other hand, as explained in section 1.3.1, the material concentration images present the effective concentration of a material. Then, the material concentration images presented in this work (simulated and obtained from the device) are given in units of concentration, as g/cm^3 or mg/cm^3 .

The material concentration images scale is also presented using the level and window. In this case, the L/W presents the corresponding units of concentration. Schlomka et al. (Schlomka et al., 2008) display their results in this same manner.

Regions for measurements

To measure the mean and standard deviation of the different images, there were defined regions of interest for each material. The defined ROIs are shown in Figure 31. There is also a region used to measure the mean value of water. The ROIs of the material inserts are smaller than the actual size of the inserts.

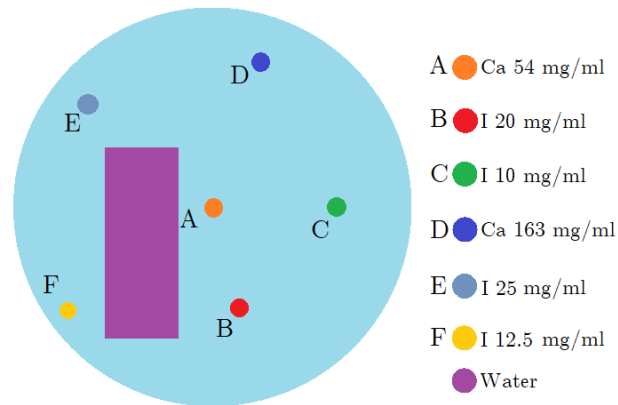


Figure 31. Representation of the regions of interest used to measure the mean value and standard deviation on both simulated and real images. Material labels A-F are shown as well as the region defined for water.

3 RESULTS AND DISCUSSIONS

The following sections present results concerning the DECT model and the CT images obtained from simulations and from the real CT device. The results concerning the localization of the bowtie filter of the modelled CT model are presented in section 3.1. The DECT images of a phantom containing iodine inserts were reconstructed and analysed in section 3.2. Finally, in section 3.3, a comparison between images obtained from real scans and simulations is presented. The phantom used for such comparison contained iodine and calcium inserts.

3.1 Modelled CT geometry

As presented in section 2.1, in the literature and technical specifications of the CT device, there was no available information about the bowtie filter features. Then, its material and shape were modelled for the simulations proposed in the present work. Therefore, it was necessary to find the best relative position (along the y -axis, Figure 22) in the region between the focal spot and collimator.

The approach adopted to find the best position of the bowtie filter consisted of two steps: 1) finding the bowtie filter position that better homogenizes the energy deposited in the modelled CT detectors and 2) comparing simulated and empirical Computed Tomography Dose Index values (CTDI_{100}) at central and peripheral axes of a cylindrical PMMA phantom.

As presented in the section Bowtie Filter (page 38), the first step consisted in the comparative evaluation of the energy deposited in the modelled CT detectors when a homogeneous water phantom is imaged. Figure 32a shows the energy deposited in the CT detectors as a function of the X-ray beam fan-angle (measured respect to the central line that passes through the center of the detectors arrangement, as suggested in Figure 25) when the 16 cm diameter water phantom was irradiated. The distances 1, 3, 5 and 7 cm correspond to some of the distances adopted between the focal spot and the center of the simulated bowtie filter.

In Figure 32a, it can be noticed that the uncertainties decrease for greater angles. This property allows observing that the use of the bowtie filter generates a decrease of the energy deposited in the detectors. For example, comparing the violet curve (Bowtie filter at 7 cm from the focal spot) with the black curve (no filter used), the difference in the energy deposited is greater for the larger angles.

Figure 32b shows the energy deposited in the three outer detectors which belong to the phantom “shadow”, as shown Figure 25, as a function of the distance between

the focal spot and the bowtie filter. In Figure 32b, the energy deposited in the detectors is minimal for focal spot–filter distances 10, 11 and 12 cm. The uncertainties of the minimum deposited energies did not allow identifying in which the energy deposited was more reduced. For such positions of minimal energy, the deposited energies represented about 25% of the obtained without bowtie filter. Therefore, for the filter positions of 10, 11 and 12 cm, the energy deposited in the outer detectors is reduced almost to a quarter of the energy that is obtained without filter.

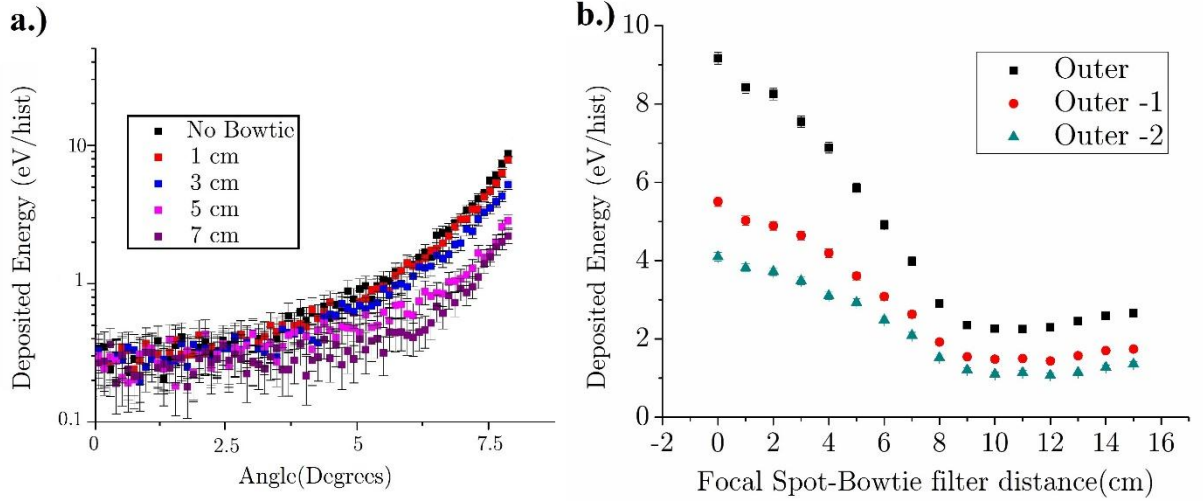


Figure 32. **a.)** Energy deposited in the detectors as a function of the fan angle (Figure 25). The energy deposited is obtained for different bowtie filter positions (1 cm, 3 cm, 5 cm, and 7 cm) and without a filter. **b.)** Response of the three most external detectors for each bowtie filter position (1 to 15 cm), the no-filter data is plotted at 0 cm position.

The second step to find the best position of the bowtie filter consisted in the comparison of the $CTDI_{100}$. The $CTDI_{100}$ was simulated using the CTDI phantom presented in Figure 26. The ratio $CTDI_{100,c}/CTDI_{100,p}$ was calculated as presented in the section Bowtie Filter (page 38), remembering that $CTDI_{100,c}$ represent the $CTDI_{100}$ in the centre of the phantom and $CTDI_{100,p}$ the mean $CTDI_{100}$ of the peripheral cylinders.

The ratio $CTDI_{100,c}/CTDI_{100,p}$ was evaluated for the three bowtie filter positions: 10, 11 and 12 cm. Then, the position that presented the ratio most similar to the results reported by Kramer et al. (Kramer et al., 2017) was chosen for the subsequent simulations. From the $CTDI_{100,c}/CTDI_{100}$ calculation, the best position was found at 10 cm from the focal spot. Ratios $CTDI_{100,c}/CTDI_{100,p}$ obtained considering this bowtie filter position are shown in Table 9.

Table 9. $\text{CTDI}_{100,c}/\text{CTDI}_{100,p}$ ratios resulting from the present simulations for 80, 100, 120 and 140 kV, ratios obtained by Kramer et al. (Kramer et al., 2017) and the percentage differences of both.

kV	$\text{CTDI}_{100,c}/\text{CTDI}_{100,p}$ (Head, 16cm)		
	This work	Kramer et al.	Percentage difference (%)
80	1.14(2)	1.07	6.5
100	1.16(2)	1.13	2.7
120	1.16(2)	1.16	0.0
140	1.14(2)	1.16	1.7

The $\text{CTDI}_{100,c}/\text{CTDI}_{100,p}$ ratios show agreement with the Kramer results for the 100, 120 and 140 kV spectra, taking into account a coverage factor $k = 2$ for the standard deviation. It is important to remark that the results of Kramer et al. do not provide uncertainties which make this comparison less conclusive.

The percentage differences obtained from the comparison are up to 6.5% (for the 80 kV spectrum). The differences are explained for the difference in the geometry and materials of the bowtie filters, this work (aluminium) and Kramer’s (PMMA). The percentage differences of Table 9 are considered acceptable for the simulations of the present work.

At this point, the definitive CT source model adopted for the simulations of the present work is represented in Figure 22 with the parameters of Table 4 and the bowtie filter positioned at 10 cm from the focal spot. With the mentioned modelled CT model, two PSFs for 80 and 140 kV tube voltages were generated. Such PSFs were used for the simulation of all projections in the present work unless otherwise stated.

Additional to this bowtie position determination, a characterization of the image reconstruction as a function of the number of simulation histories was performed. The methodology and results concerning such characterization are presented in Appendix A. The characterization was conducted by analysing the SNR and CNR. Section A.1 presents the features of the simulations performed to characterize both SNR and CNR in the simulated CT images. Section A.1 also describes the methodology used to implement the BMD method and analyse the material concentration and monoenergetic images of a water phantom containing a bone insert.

Section A.2 presents plots of the SNR and CNR calculated in simulated phantoms with a central material insert. The data presented show how the CNR and SNR increase as increasing the number of histories, especially for materials of attenuation coefficient greater than water. The CNR and SNR pertaining to the bone insert were almost an order of magnitude greater than the values obtained for the other materials.

According to the results of the Section A.2, it was possible to conclude that a greater number of histories improves the image definition of the monoenergetic and material concentration images. For the water phantom with the bone insert, the method that exhibited better material differentiation images was the Projection-Based BMD.

This part of the study was conducted to improve the level of confidence of the results depending on the number of initial histories used in the simulations. The number 10^9 initial histories was chosen as it balances the computational time considering the available hardware.

3.2 Simulations using the water-iodine phantom

This section deals with the simulated images concerning the dual energy analysis of the phantom shown in Figure 27. The phantom consists of a water cylinder containing three iodine concentrations in six cylindrical inserts. The three simulated concentrations of iodine were 45, 30 and 15 mg/cm³, with the labels I-45, I-30 and I-15 as shown in Figure 27. The methodology used is described in section 2.2.

The projections were acquired from simulations as described in section 2.1.2. Figure 33 shows the standard sinograms obtained for an angular step of 1 degree. It is possible to see the sinusoidal strips corresponding to each insert. The computation time to generate these sinograms was approximately 64 hours using the computer servers WSDOM and WSDOSB (Table 3).

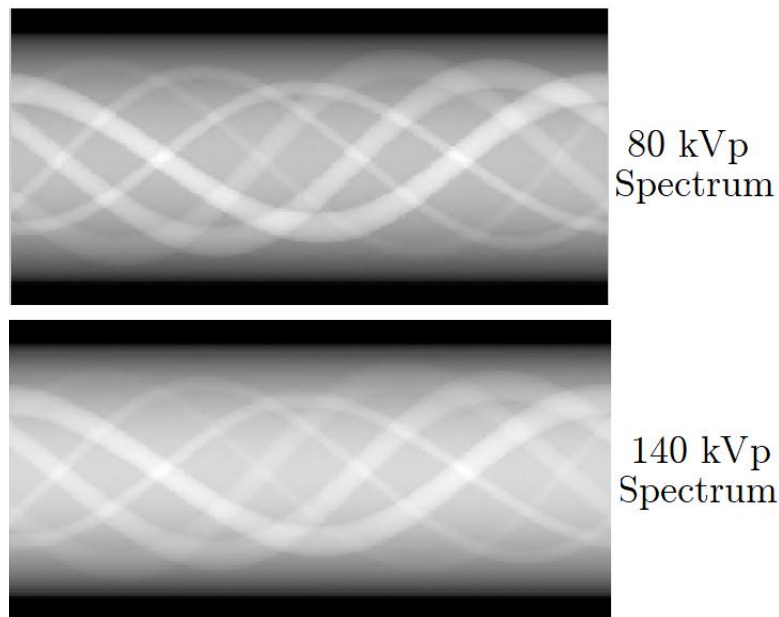


Figure 33. Sinograms obtained for an angular step of 1 degree and for both 80 kV and 140 kV spectra. The curves corresponding to each iodine insert are visible.

Using the sinograms presented in Figure 33, the 80 kV and 140 kV standard images were reconstructed using the FBP algorithm available in Matlab®. The images are displayed in Figure 34. Beam hardening artefacts are present in both standard images, especially in the 80 kV image.

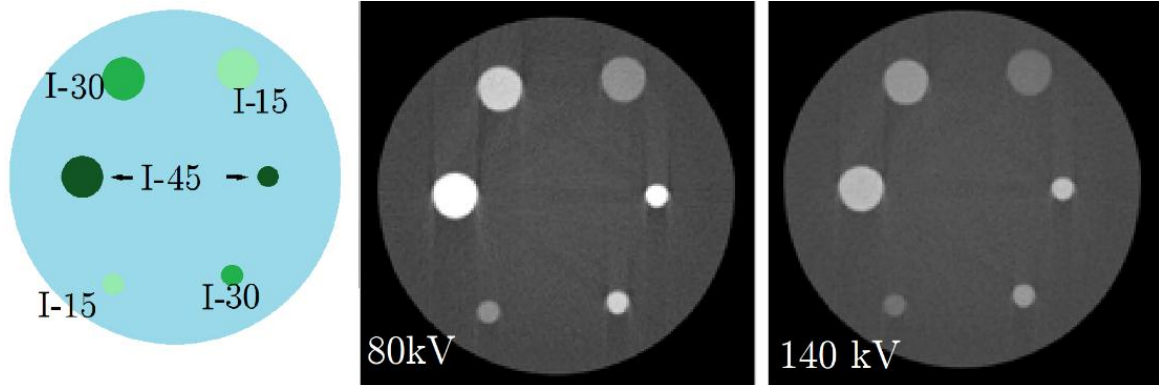


Figure 34. Standard images reconstructed for the 80 and 140 kV spectra. Beam hardening artefacts are present in both images, especially in the image of 80 kV. Image size: 160x160 pixels. L/W: 650 HU/1850 HU. On the left, the representation of the phantom and its iodine concentrations is reprinted from Figure 27.

3.2.1 Projection-Based BMD

The Projection-Based BMD uses the information of the sinograms (Figure 33) to obtain projections corresponding to each material or “material sinograms” (section 1.3.1, Figure 20). As the phantom contained water and iodine inserts, the functions selected for the decomposition were the mass attenuation coefficients of water and iodine. The mass attenuation coefficients were extracted from the X-COM database (Berger M. et al., 2017). The energy dependence of the mass attenuation coefficients is depicted in Figure A-2 (Appendix A).

The material sinograms are shown in Figure 35. These sinograms present the solution for C_1 (water) and C_2 (iodine) of equations (19) and (20), from them $c_1(x, y)$ and $c_2(x, y)$ are obtained by applying the FBP (as presented in Figure 20). The mathematical calculation of the material sinograms spent about 30 hours of computation time, using just one core of the server WSDOSB. Applying the filtered Backprojection to the material sinograms presented in Figure 35, the material concentration images were obtained and are shown in Figure 36.

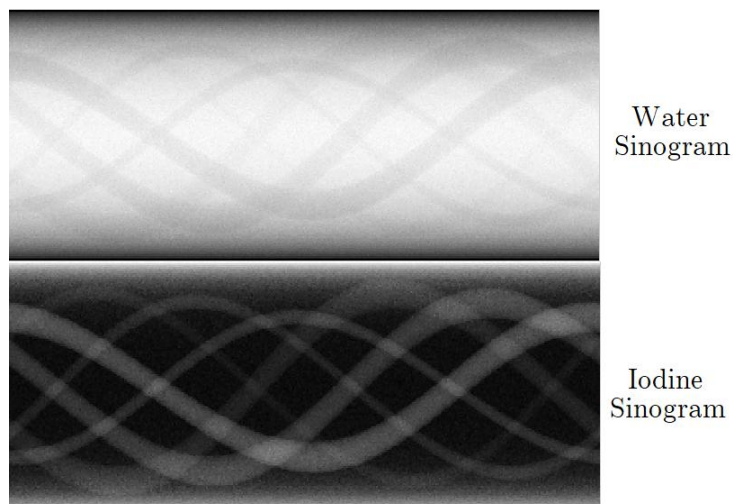


Figure 35. Material sinograms for water and iodine reconstructed from the 80 and 140 kV projections (Figure 33). The material sinograms were obtained following the theory presented in the section 1.3.1.

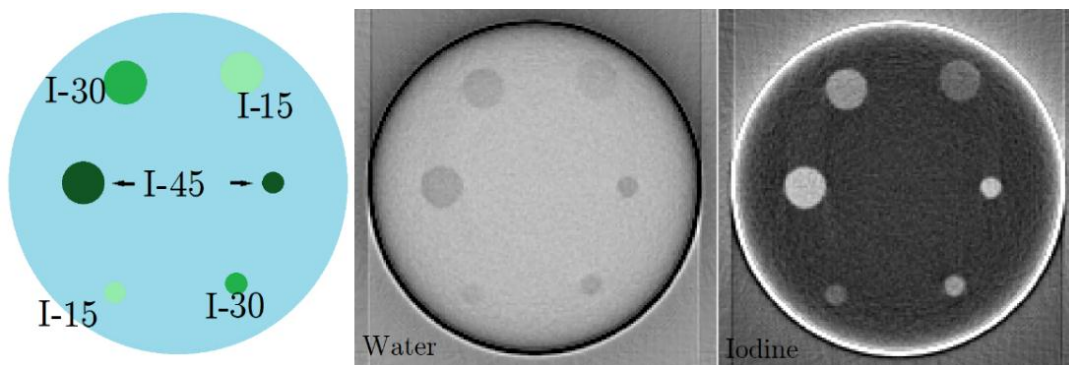


Figure 36. Reconstructed concentration images for water (L/W $0.82 \text{ mg cm}^{-3} / 0.37 \text{ g cm}^{-3}$) and iodine (L/W $23 \text{ mg cm}^{-3} / 42 \text{ mg cm}^{-3}$) using the Projection-Based BMD. On the left, the representation of the phantom and its iodine concentrations is reprinted from Figure 27.

As mentioned in section 2.2, the grey levels of the material concentration images were calibrated using a linear function. Then, the mean effective concentrations were calculated in the iodine inserts of the calibrated iodine concentration images. The values found by analysing the inserts grey levels were similar to the expected concentration, with differences lower than 2%. The adjusted calibration function in this section will be used to calibrate the concentration images of section 3.3.

3.2.2 Image-Based BMD

The straightforward reconstruction method is the Image-based BMD (section 1.3.2). Water and iodine concentration images of Figure 37 were calculated from the standard images presented in Figure 34. As the Image-Based BMD method requires the computation of four matrix elements and the resolution of a system of two linear equations per pixel (equations (21) to (24)), the computation and display of the images took just a few seconds.

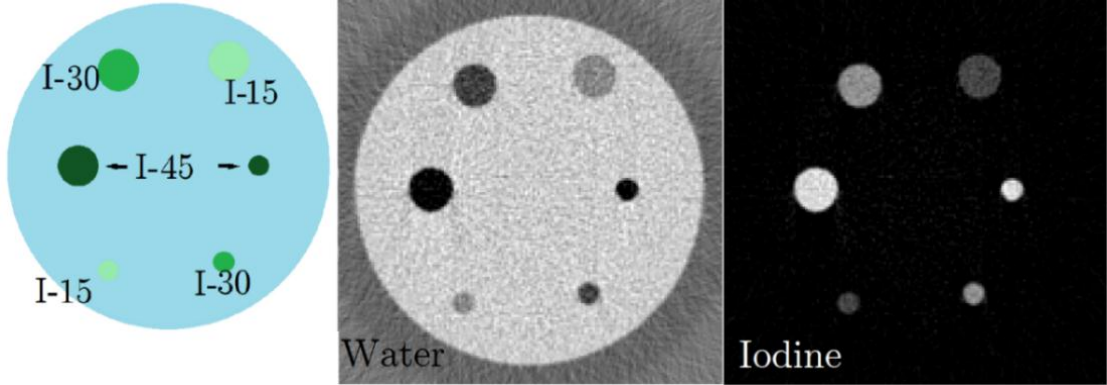


Figure 37. Reconstructed material concentration images of water (L/W : $0.94 \text{ g cm}^{-3} / 0.09 \text{ g cm}^{-3}$) and iodine (L/W : $26 \text{ mg cm}^{-3} / 25 \text{ g cm}^{-3}$). The images were generated using the Image-Based BMD method. On the left, the representation of the phantom and its iodine concentrations is reprinted from Figure 27.

In Figure 37, it is possible to see how the iodine inserts are subtracted in the water concentration image. As the iodine inserts also contain water, the grey shades of the cavities corresponding to the iodine inserts in the water concentration image are expected. The iodine concentration image of Figure 37 presents black in the water region and different grey values in the iodine inserts. The whiter insert in the iodine concentration image corresponds to the insert containing the highest concentration of iodine, 45 mg/cm^3 .

The images of Figure 36 are different from the ones of the Image-Based method, presented in Figure 37. These differences are associated to the BMD methods, in spite of both sets of images were obtained from the same set of initial projections.

3.2.3 Monoenergetic images

Once found the spatial distribution of water and iodine (Figure 36), it was also possible to reconstruct monoenergetic images. As mentioned in section 1.3.1, the monoenergetic images are reconstructed using the solution for $c_1(x, y)$ and $c_2(x, y)$ (material concentration images in Figure 36), and the functions $f_1(E)$ and $f_2(E)$ at the energy of interest. Equation (18) was used to produce the monoenergetic images. It means that the monoenergetic images are linear combinations of the material concentration images, which are spatial functions, weighted by the mass attenuation coefficients $f_1(E)$ and $f_2(E)$ at the desired energy.

The virtual monoenergetic images considering the maximum energies of the considered spectra, 80 keV and 140 keV, and their respective effective energies, 48 keV and 62 keV (Table 5), are shown in Figure 38.

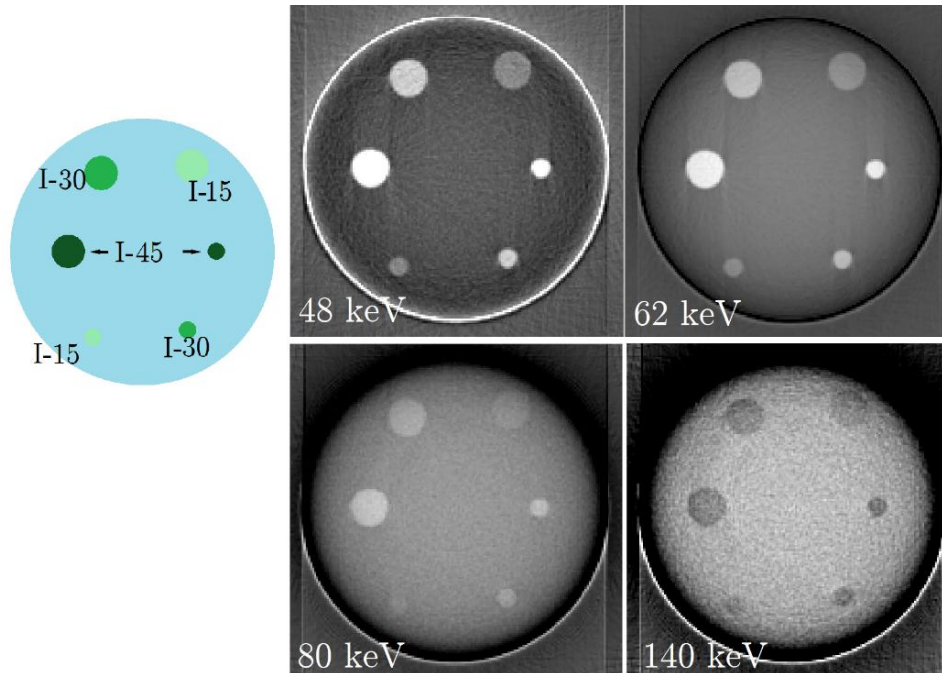


Figure 38. Reconstructed monoenergetic images for 48 keV (L/W: 500 HU/2000 HU), 62 keV (L/W: 0 HU/1500 HU), 80 keV (L/W: -250 HU/1250 HU) and 140 keV (L/W: -500 HU/1000 HU). Images obtained using the Projection-Based BMD method. On the left, the representation of the phantom and its iodine concentrations (Ultravist®) is reprinted from Figure 27.

Comparing to the standard reconstructed images of Figure 34, the images of Figure 38 show some features as:

- Both monoenergetic images of 62 and 80 keV are similar to standard CT images, but with reduced beam hardening artefacts.
- In contrast, the 140 keV monoenergetic image looks different from the standard images. In such image, the iodine inserts seem to possess attenuation coefficient less than water. It is possible to observe the 140 keV monoenergetic image is similar to the water concentration image of Figure 36.
- The image of 48 keV also looks different from the standard images, in this case, the image presents a white line in the edge of the water cylinder. This is a feature of the iodine concentration image of Figure 36.

Then, the 140 keV monoenergetic image presents a dominant contribution of the water concentration image and the monoenergetic 48 keV image presents a dominant contribution of the iodine concentration image. Thus, it is possible to think that there is a range of energies where the virtual monoenergetic images represent information of the imaged object similar to what would be obtained in real monoenergetic images. It is also possible to say that for high energies the water component dominates in the monoenergetic images and for low energies the iodine contribution dominates. Generally low energy monoenergetic images present enhancement of high attenuators, which is important to enhance the detection of structures in clinical CT.

3.3 Real phantom comparison

This section presents the results concerning the simulations and measurements using the real and simulated phantoms of Figure 29. The images acquired using the GE Discovery CT 750 HD device will be thereafter called real images. The simulated images were obtained using the CT model described in the previous sections.

According to section 2.3.1, the types of images acquired are standard, material concentration and monoenergetic. This section is divided following these types of images. Section 3.3.1 presents a comparison of the standard images. Section 3.3.2 presents the results of the material concentration images. Section 3.3.3 presents a comparative evaluation of the monoenergetic images of both simulated and real CT devices. The images presented in this section were reconstructed using the Projection-Based BMD as explained in section 1.3.1. The scheme of Figure 20 summarizes the different algorithms and reconstruction used to obtain each image.

3.3.1 Standard images

In this section both simulated and real standard images are presented. Figure 39 shows the images obtained with the DECT equipment Discovery CT 750 HD. The simulated standard images of the phantom are shown in Figure 40.

The standard images (Figure 39) were acquired to be compared to the standard images obtained using simulations. The GSI mode used to acquire material concentration and monoenergetic images does not allow displaying the standard images at each energy spectrum (Figure 30). Thus, the information of the real standard images presented in Figure 39 was not used to reconstruct the material concentration and the monoenergetic images.

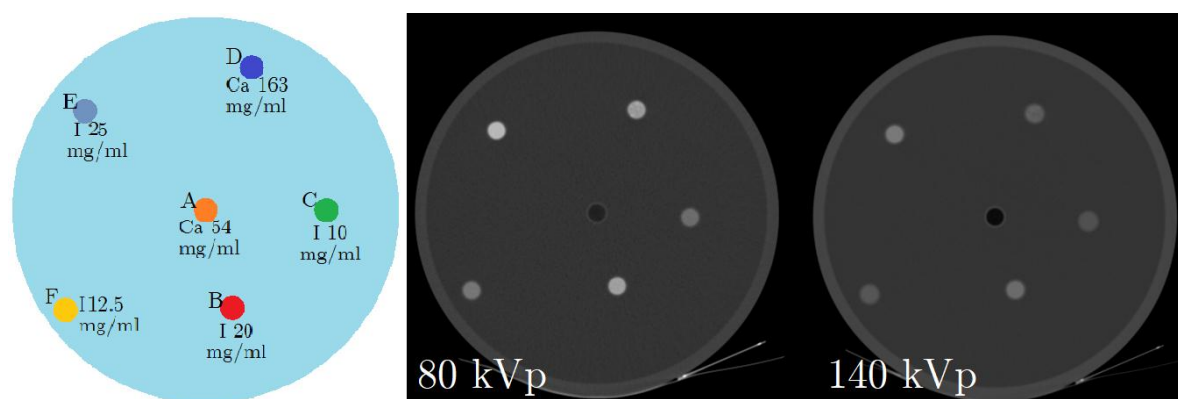


Figure 39. Standard images obtained with the real CT scanner, the images were obtained in axial mode with a slice thickness of 5 mm. The images were obtained with the same exposition 270 mAs. The image size is 512x512 pixels, L/W: 596 HU/2002 HU. On the left, the representation of the inserts and material concentrations is reprinted from Figure 29.

In Figure 39, the 80 kV image presents the brighter inserts as iodine attenuates more efficiently at low energies. A difference among the simulated and the real images is the presence of the acrylic wall in the real phantom, which is clear in the images of Figure 39.

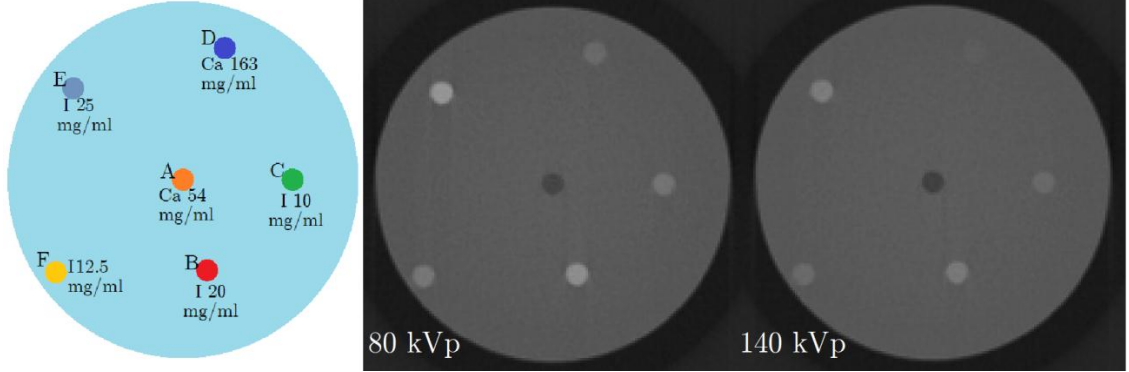


Figure 40. Simulated standard images for 80 kV and 140 kV spectra (L/W: 596 HU/2002 HU). The beam hardening artefacts in the 80 kV image of the two highest concentrations of iodine are smooth but perceptible. On the left, the representation of the inserts and material concentrations is reprinted from Figure 29.

The reduction of the beam hardening artefacts when comparing Figure 40 to Figure 34 is a consequence of the lower iodine concentration adopted for producing these images. In Figure 40, the insert D in the 140 kV image presents a grey level close to the background which make difficult its identification.

Table 10 lists the mean and standard deviation measured in ROIs positioned inside the material inserts in both real and simulated images. The ROIs used for such measurements are shown in Figure 31. The pixel calibration to convert from $\bar{\mu}$ to HU was done as presented in section 1.1.4.

Table 10. Measured mean HU for the standard images obtained from both simulations and real device images, and t and t_{crit} to compare the values.

Label	80 kV				140 kV			
	Real (HU)	Simulated (HU)	t	t_{crit}	Real (HU)	Simulated (HU)	t	t_{crit}
A (Ca 54)	-202±8	-316±38	2.90	2.07	-343±5	-390±23	1.96	2.08
B (I 20)	842±5	780±23	2.70	2.07	434±2	464±26	1.15	2.08
C (I 10)	446±5	387±23	2.57	2.07	225±2	226±24	0.08	2.08
D (Ca 163)	677±14	226±24	16.37	2.03	257±9	41±16	11.76	2.03
E (I 25)	1033±5	896±22	6.26	2.07	542±2	502±20	1.98	2.08
F (I 12.5)	518±5	430±21	4.01	2.07	273±2	234±16	2.49	2.08
Water	1±5	-1±26	0.05	2.08	0±2	2±22	0.09	2.08

The t-test was performed following the theory presented in Appendix C. In this case the number of degrees of freedom, ν , depends in each pair of compared values. It is omitted in the table, instead t_{crit} is presented. The test was performed using a two-tailed distribution with significance level of 5%. The values in green present the values which present agreement under the t-test. Just the HU of water agrees for the 80 kV spectrum. In the case of the 140 kV spectrum most of the simulated and real CT numbers agree, except for the Ca-163 and the I-12.5 insert.

The mean HU value measured in the iodine inserts of the 80 kV images is always less than the obtained from the real device. The differences in the obtained HU of the table can be due to the use of different X-ray spectra and bowtie filter. It can also be explained as the 80 kV spectra presented the higher differences when comparing with the literature results in Table 9.

In the case of the calcium inserts, the differences can be attributed to the simulated composition and the preparation of the inserts. There were obtained variations in the mean grey level of the regions containing calcium. Such differences of HU were appreciable among the four slices as presented in Figure 41. Consequently, the calcium inserts presented the highest uncertainties in columns corresponding to the real images in Table 10. As mentioned in section 2.3, the calcium inserts were prepared with powders. During the procedure of filling the cylinders with such powder, a pressure was manually exerted to compact the powder. Therefore, there was no accurate control of this variable. Then, the calcium inserts had not the same mass density along the cylinder.

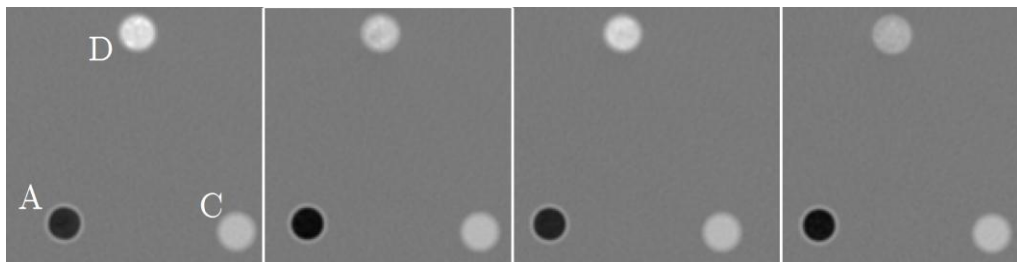


Figure 41. Regions inside the images corresponding to the four slices at 140 kV, the inserts represented are the A, C and D. The variation in the grey level of the insert D among the slices is appreciable. The grey level of the insert C, which contains iodine, is less variable among the slices. L/W: 1300 HU / 2100 HU.

An important feature of the simulated and the real images is the noise. As presented by Bushberg et al. (Bushberg et al., 2011), the noise is estimated as the standard deviation in a ROI defined as the background. The background was defined as the water region presented in Figure 31. Comparing the standard deviation of the water grey levels Table 10, it is observed that the noise of the real 80 kV image, $\sigma=5$ HU, is more than twice the noise of the real 140 kV image, $\sigma=2$ HU. This

difference in noise is not appreciable in the displayed images because of the used W/L combination. This behaviour of the noise is expected as both real images were acquired using the same current–time product (mAs). Then, the photon fluence emitted using the 80 kV tube tension, is lower than the photon fluence produced using 140 kV. As the noise is inversely proportional to the photon fluence impinging the detectors, these differences in fluence impact the noise of both images.

On the other hand, according to Table 10, the values of the noise of both simulated images are similar: $\sigma=26$ for the 80 kV image and $\sigma=22$ for the 140 kV image. In this case, both simulated images were obtained using the same number of initial photons. If the materials of the phantom do not have a high attenuation coefficient and are not thick, the number of photons reaching the detectors is similar for both spectra. Then, the simulated images present noise in the same order of magnitude.

3.3.2 Material concentration Images

In this section, the results concerning the material concentration images are presented. This section is divided according to the pairs of materials used to perform the BMD: water–iodine and water–calcium. The energy dependence of the mass attenuation coefficients used for the decomposition is found in Appendix A (Figure A-2). As the device uses the Projection–Based BMD (section 1.3.1) this was the method adopted to process the simulated images.

Water–Iodine

This section presents the results of the material differentiation when the water and iodine functions are used to perform the BMD. The water and iodine concentration images acquired in the real device are displayed in Figure 42. The corresponding images obtained from simulations are shown in Figure 43.

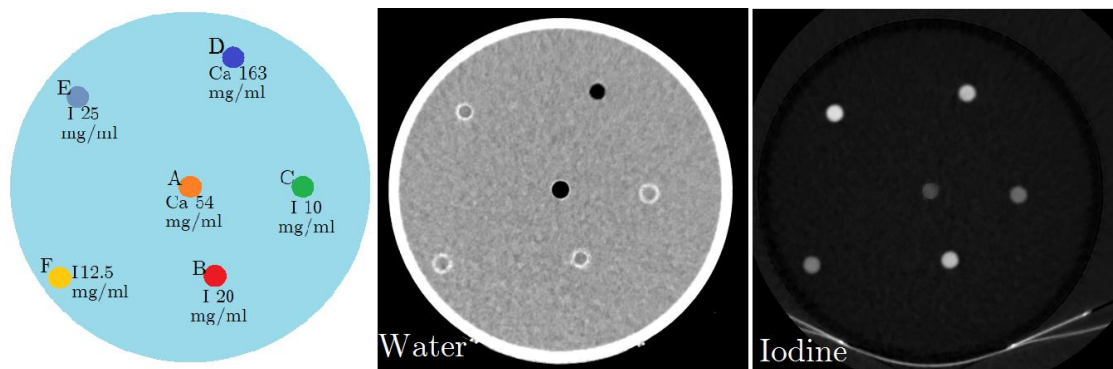


Figure 42. Material concentration images obtained from the real device. The decomposed materials were water (L/W: $966 \text{ mg cm}^{-3}/313 \text{ mg cm}^{-3}$) and iodine (L/W: $128 \text{ mg cm}^{-3}/306 \text{ mg cm}^{-3}$). On the left, the representation of the inserts and material concentrations is reprinted from Figure 29.

The images obtained in the GE Discovery CT 750 HD present good material differentiation as can be seen in Figure 42. Some important features concerning these images are:

- The water concentration image presents grey in the water region and in the iodine inserts region, once more than the 85% of the iodine inserts is water;
- The water concentration image presents black in the calcium inserts. Even when they attenuate similar to the iodine inserts (Figure 39), the water concentration image presents such inserts with minimum content of water; and,
- The iodine concentration image presents black in the water region and grey shades in the iodine and calcium inserts.

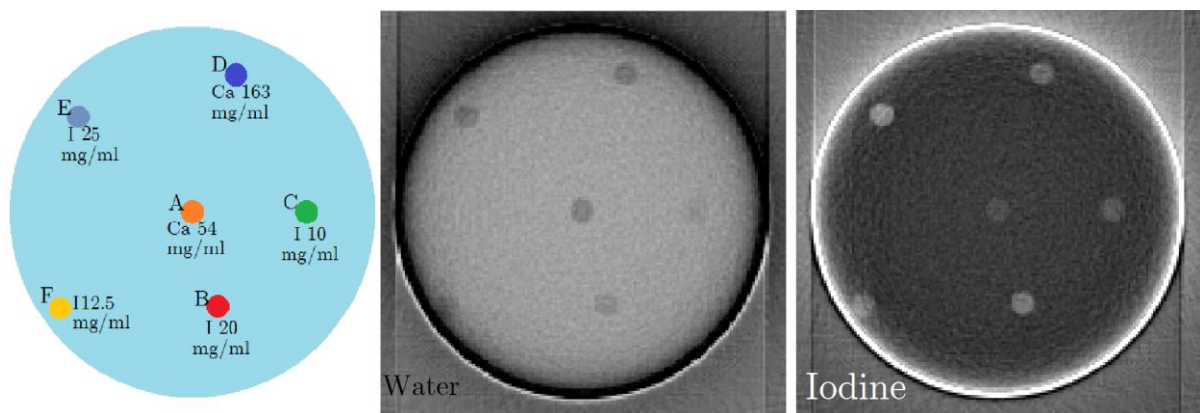


Figure 43. Material concentration images obtained from the simulations for water (L/W: $0.925 \text{ g cm}^{-3} / 0.275 \text{ g cm}^{-3}$) and iodine (L/W: $23 \text{ mg cm}^{-3} / 43 \text{ mg cm}^{-3}$). On the left, the representation of the inserts and material concentrations is reprinted from Figure 29.

Some characteristics concerning the material concentration images obtained from simulations (Figure 43) are:

- The water concentration image presents grey shadows in the regions corresponding to the material inserts of calcium and iodine;
- The I-10 iodine insert is almost disappearing in the water concentration image. Such insert corresponds to the lowest iodine concentration, i.e. the highest concentration of water. This explains why this insert is the less defined in the water concentration image;
- The water concentration image presents an artefact in the external surface of the phantom. In this case, the surface seems to present less concentration of water than the central part of the phantom. As this feature is the opposite of the beam hardening artefact, in the present work this artefact is called “inverse hardening artefact”;

- In the iodine concentration image, the material inserts are whiter than the background. In this case, the most internal inserts are less visible, as the I-10 and Ca-54 inserts; and
- The iodine concentration image presents an artefact in the external surface of the phantom. It seems that the external surface presents greater concentration of iodine than the central part of the phantom. It is a feature of beam hardening artefact.

The measured mean values inside the iodine inserts in both iodine concentration images (Figure 42 and Figure 43) are presented in Table 11. There are presented the expected and measured concentrations and their respective uncertainties. The uncertainties of the expected values were estimated in the process of preparation of the phantom. The concentration was directly measured in the iodine concentration images as the mean in an internal ROI of each insert. The uncertainties of the real and simulated values were obtained from the standard deviation of the mean in the respective ROIs defined in Figure 31. Table 11 also presents the t-test values (Appendix C) of the comparison of the measured and expected concentrations. Table 11 shows that the concentrations obtained from the real and simulated images are similar to the expected ones.

A feature of the images obtained in the real scan is that the images presented a map of values and a rescale factor. The values shown in Table 11 correspond to the values measured in the image applying the rescale factor. The simulated concentration values were calculated in the iodine image applying the calibration obtained from the iodine concentration images presented in section 3.2.

Table 11. Measured effective iodine concentration in the inserts of the iodine concentration images of Figure 42 and Figure 43. The expected concentration coincides with the “Concentration” column in Table 8. The t-values (Appendix C) were computed comparing the Real and Simulated concentrations with the expected values. The uncertainty of the expected values was considered in the t-values calculation.

Iodine material	Concentration			t-test	
	Expected (mg/cm ³)	Real images (mg/cm ³)	Simulated (mg/cm ³)	Real images	Simulated
B (I 20)	20±1	19.41±0.03	20±4	0.59	0.05
C (I 10)	10.0±0.4	9.97±0.01	10±3	0.07	0.06
E (I 25)	25±1	23.50±0.03	30±4	1.50	1.02
F (I 12.5)	12.5±0.5	11.33±0.02	23±5	2.34	1.95

The t-test values presented in Table 11 were obtained with a modification on the standard deviation of the mean, σ_m . To consider the uncertainty of the expected values, σ'_m was used instead of σ_m . σ'_m is defined in equation (33) where σ_{exp} represent the uncertainty of the expected value and σ_m the standard deviation of the mean in the ROI corresponding to the evaluated insert.

$$\sigma'_m = \sqrt{\sigma_{\text{exp}}^2 + \sigma_m^2} \quad (33)$$

For the comparison of the real images, the selected significance level was 5% and $t_{\text{crit}} = 1.96$, for 612 degrees of freedom (616 pixels in 4 ROIs). Then it is possible to conclude that the concentrations obtained from the real images agree for the I-10, I-20 and I-25 inserts, as its t-values are less than t_{crit} . The hypothesis of agreement of the insert I-12.5 insert is rejected as the t-value obtained for this insert was greater than t_{crit} .

For the simulated images, the significance level was 5% and $t_{\text{crit}}=2.086$, for 20 degrees of freedom (21 pixels in the ROI). Then, it is possible to note that effective concentrations obtained from simulation agree with the expected ones as all the t values are less than t_{crit} . Even when the concentration of the inserts I-25 and I-12.5 differ from the expected, their t-value are small due to their uncertainty.

It is important to mention, that the simulated phantom contained materials with the exact concentrations. Then, the uncertainties associated with the measured concentrations in the simulated images are associated to simulation, reconstruction algorithms and calibration. The real images contained the materials that were prepared. In such case, the uncertainties can be associated with the reconstruction algorithms, to the material preparation uncertainties and to the image acquisition.

There were also measured the material concentration of water in the water concentration images. In this case, the expected value for the concentration was the 1 g/cm^3 as distilled water was used. The value obtained from the real water concentration image is $(1.000 \pm 0.005) \text{ g/cm}^3$. The concentration value obtained from the simulated water concentration image was $(0.84 \pm 0.06) \text{ g/cm}^3$. This value does not agree with the expected concentration of water. It could be related to the calibration of water or even to the inverse hardening artefact presented in the image of water.

Water-Calcium

This section collects the results of the material differentiation when the water and calcium mass attenuation coefficients are used to perform the BMD. The water and calcium concentration images obtained in the real device are shown in Figure 44.

The water and calcium concentration images obtained from simulations are shown in Figure 45.

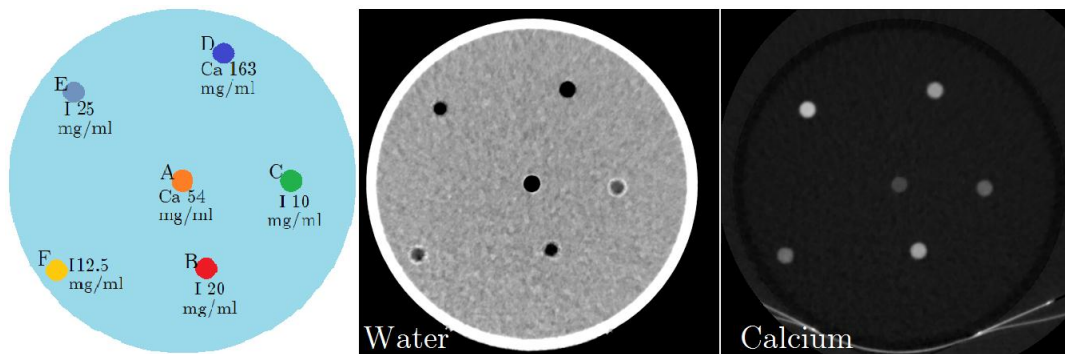


Figure 44. Material concentration images obtained from the real device. The decomposed materials were water (L/W: $966 \text{ mg cm}^{-3}/313 \text{ mg cm}^{-3}$) and calcium (L/W: $208 \text{ mg cm}^{-3}/ 518 \text{ mg cm}^{-3}$). On the left, the representation of the inserts and material concentrations is reprinted from Figure 29.

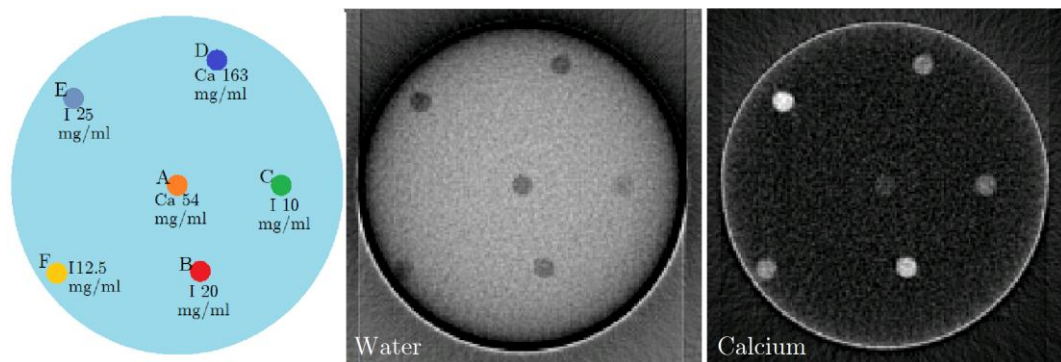


Figure 45. Material concentration images obtained from the simulations. The decomposed materials were water (L/W: $0.94 \text{ g cm}^{-3}/0.14 \text{ g cm}^{-3}$) and calcium (L/W: $27 \text{ mg cm}^{-3}/ 27 \text{ mg cm}^{-3}$). On the left, the representation of the inserts and material concentrations is reprinted from Figure 29.

Some features concerning the material concentration images obtained in the Discovery CT 750 HD, presented in Figure 44, are:

- The water concentration image presented in Figure 44 is displayed with the same level and window of the water concentration image of Figure 42. In this case, the water concentration image of Figure 44 presents less water concentration in the iodine inserts.
- The calcium concentration image presented in Figure 44 is similar to the iodine concentration image of Figure 42.

It is important to remark that the grey levels in the material concentration images represent the *effective* concentration of the material in the imaged object. Then, obtaining white color in a ROI of iodine in the calcium concentration image of Figure 44 does not mean that the insert contains calcium, but that the method associates a high concentration of calcium, when calcium and water are used to perform the BMD.

Some characteristics concerning the material water and calcium concentration images obtained from the simulations in Figure 45 are:

- The water concentration image of Figure 45 is similar to the simulated water concentration image of Figure 43. The artefact known as inverse beam hardening is also present.
- The calcium concentration image of Figure 45 is similar to the iodine concentration image of Figure 43. The calcium concentration image also presents the hardening artefacts in the surface.
- The cylinders that present the highest effective concentration of calcium are I-20 and I-25.
- The images of Figure 45 were not calibrated as there wasn't performed a previous simulation containing calcium.

The material concentration of water in the water concentration images was measured. The expected value of the concentration was 1 g/cm^3 for distilled water. The value obtained from the real water concentration image was $(1.001 \pm 0.006) \text{ g/cm}^3$, which agrees with the expected concentration.

The concentration values measured from the simulated and real images were not similar to the expected concentrations of calcium. As mentioned in the previous section, the calcium inserts presented clear differences in CT numbers among the four slices. It means that the materials presented a strong non-homogeneity. In addition, the carbon black, material used in the mixture with the calcium carbonate, was assumed as pure carbon, but it could contain high atomic number impurities. The calcium carbonate also includes a significant content of magnesium with atomic number 12. That is, the mixtures of powders may not represent good calcium equivalent material.

Then, the differences in the concentration obtained in the real image can be attributed to the systematic errors in the preparation of the calcium inserts, and on the material composition itself. In the case of the simulation, an additional factor is the lack of calibration. It makes necessary a better knowledge of the material composition for future studies.

3.3.3 Monoenergetic images

This section presents the virtual monoenergetic images that were obtained in the real device and from simulations. The images reconstructed in the Discovery CT 750 HD were acquired for the pair of materials water-iodine, thus, the simulated images the same pair of materials was used.

Figure 46 presents the monoenergetic images for the energies 70, 80 and 140 keV. The level and window of the displayed images are similar to that of the standard images of Figure 39. The images of 70 and 80 keV look similar to the images of Figure 39.

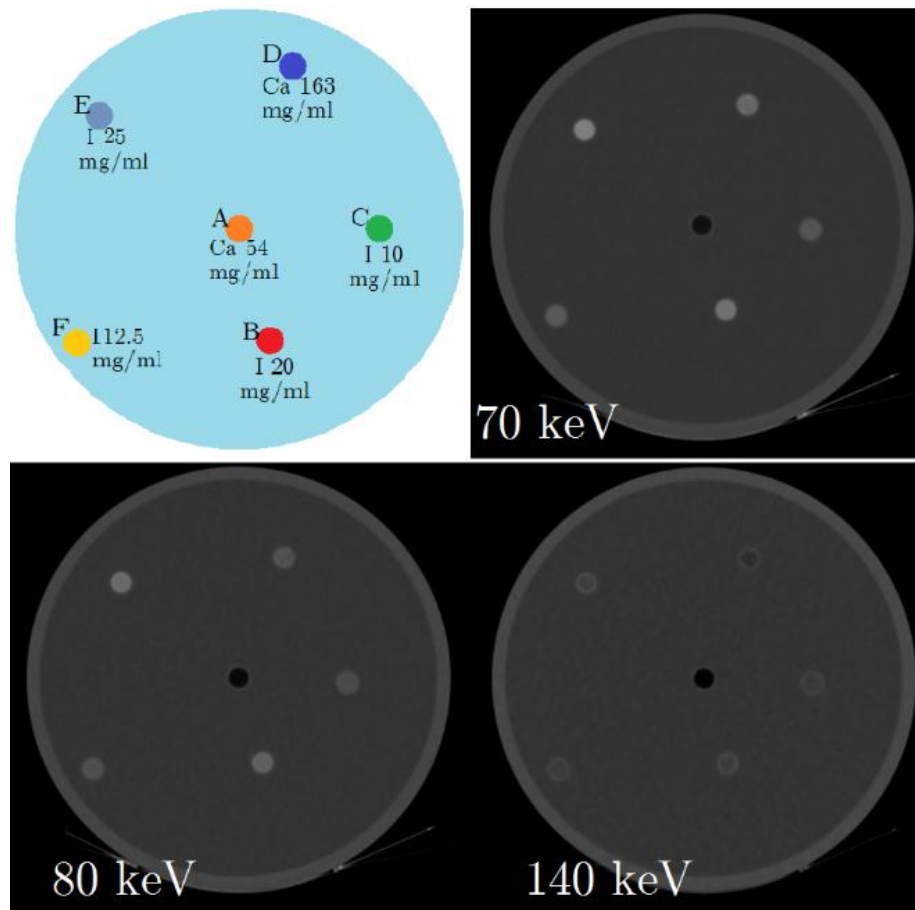


Figure 46. Monoenergetic images for 70, 80 and 140 keV (L/W: 594 HU/2005 HU). The images were obtained using the real device. The images were reconstructed using the Projection-Based BMD method, for the materials water and iodine. On the left, the representation of the inserts and material concentration distributed in the phantom is reprinted from Figure 29.

The monoenergetic image of 140 keV presents the D insert (Ca 163) as less attenuating than water. The mean CT number measured at the D insert was -107 ± 2 HU, meanwhile, water was 0.5 ± 0.1 HU. As the monoenergetic images of Figure 46 are a linear combination of the material concentration images of Figure 42, it is possible to see that for the 140 keV monoenergetic image, the contribution of the water concentration image dominates. The same behaviour was found in the section 3.2 for the simulated 140 keV monoenergetic image.

Figure 47 presents the monoenergetic images acquired from simulations for the energies 48, 62, 70, 80 and 140 keV. The figure also presents the images of 48 and

62 keV, which correspond to the effective energies of the spectra used in the simulations.

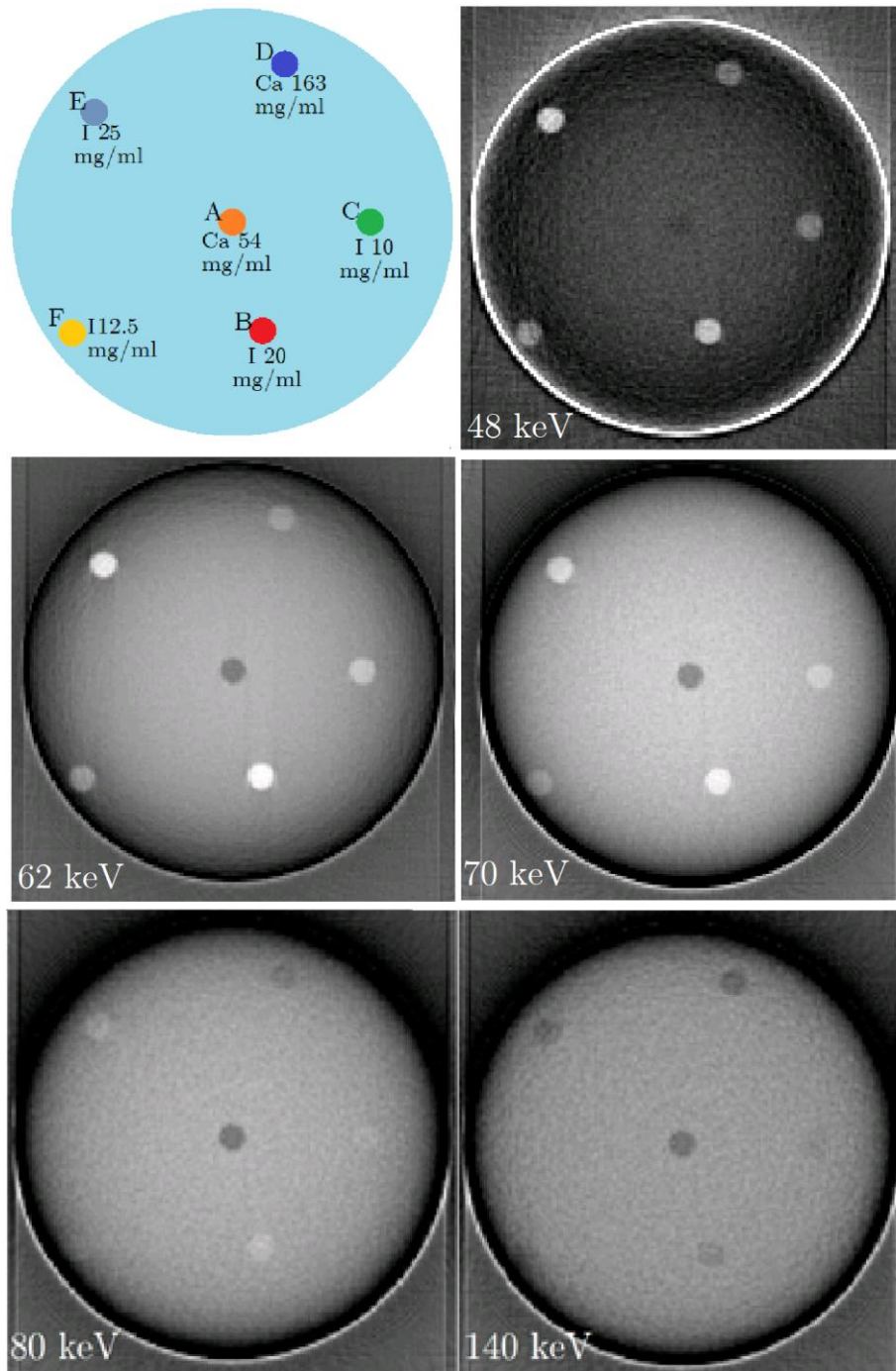


Figure 47. Monoenergetic images for 48 keV (L/W: 1000 HU/3000 HU), 62 keV (L/W: -655 HU/2345 HU), 70 keV (L/W: -1150 HU/2350 HU), 80 keV (L/W: -930 HU/3070 HU) and 140 keV (L/W: -932 HU/5060 HU). The images were obtained from simulations and reconstructed using the Projection-Based BMD method. On the left, the representation of the inserts and material concentration is reprinted from Figure 29.

The 140 keV monoenergetic image presented all inserts with a dark grey level meanwhile the water region presented light grey level. It means that the image is showing the material inserts as if they possess lower attenuation coefficient than water.

In the 80 keV image, the D insert also appears as less attenuator than water. The 62 keV image presents all the inserts, except for the A, as higher attenuators than water, as was obtained in the standard images.

In the monoenergetic images for 62, 70, 80 and 140 keV the presence of inverse beam hardening artefacts is observable on the external surface of the phantom. Such artefact is characteristic of the material concentration image of water (Figure 43). The image obtained at 48 keV presented beam hardening artefact on the external surface of the phantom. Such artefact is characteristic of the iodine concentration image (Figure 43).

In the real and simulated monoenergetic images, it was found cases where the images do not present information with physical meaning. Therefore, there is a range of energies where the monoenergetic images presented unusual behaviour, different to standard CT images. It was found that, for high energies, the water contribution dominates the monoenergetic images, and for low energies the iodine contribution dominates. The monoenergetic images obtained from simulation at 48 keV and 140 keV were more similar to the material concentration images than to the standard CT images.

Yu et al. (Yu et al., 2011) found an optimum energy for the monochromatic images. Such energy depends on various factors as the size of the imaged object, the dose partitioning between the low and high energies and the specific quality metric to optimize. When optimizing the CNR in iodine, the optimal monochromatic energy increased as the phantom size increased. The scanner used by Yu et al. was a dual-source CT. In such device, the dose partitioning can be altered using different filters and currents in both X-ray tubes. Such partitioning is not easily implemented in a rapid kV switching scan as neither filter nor current are flexible to be altered between the switching. Additionally, while the kV-switching device uses the Projection-Based BMD method, the BMD method used in a dual source CT is the Image-Based.

In the next pages CNR is studied in both, real and simulated monoenergetic images for the kV-switching device.

CNR in the virtual monoenergetic images

Monoenergetic images were obtained from both real device and simulations. The CNR was calculated in each insert at each monoenergetic image. The virtual monoenergetic images used to calculate CNR from both real device and simulations are presented in Figure D-1 and Figure D-2, in Appendix D.

CNR values were calculated following equation (14), where the ROIs inside the inserts and background (corresponding to a water region) were defined as presented in Figure 31. The CNR curves obtained from the images of the real device and from the simulations are presented in Figures 47 and 48, respectively.

It is possible to note the difference in the order of magnitude of the CNR values of the images acquired in the real device and from simulations. In this case, it is due to the noise which is smaller in the real device images. This generates greater CNR for the real device images, according to equation (14).

The CNR curves of both real-device and simulated images presented a discontinuous increase in the CNR at an energy of 33.2 keV which match with the energy of the K-border of iodine. As the superposition implemented to generate the monoenergetic images of equation (18) is weighted by the mass attenuation coefficient of iodine and water, the discontinuous increase in the CNR corresponds to the high contribution of the iodine concentration image at the energy of the K-border.

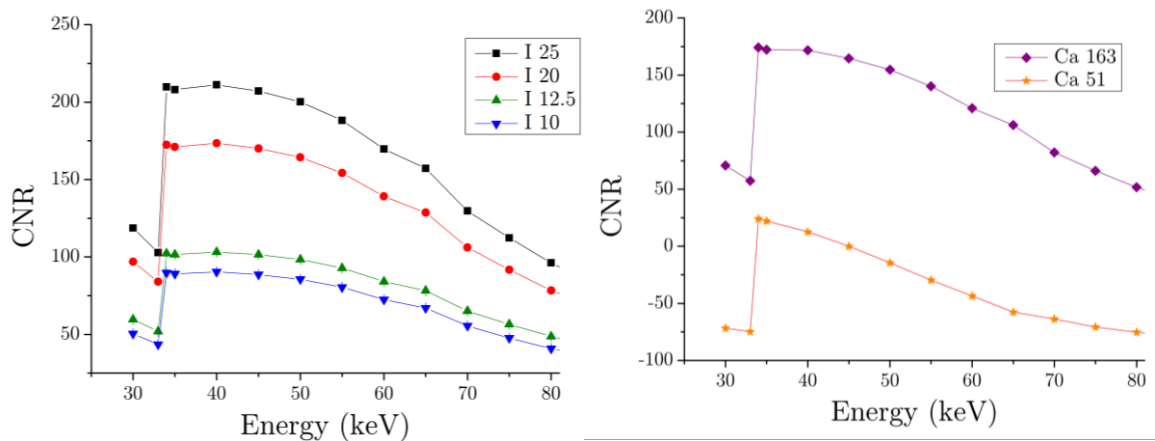


Figure 48. CNR as a function of the energy of the virtual monochromatic images obtained from the real device.

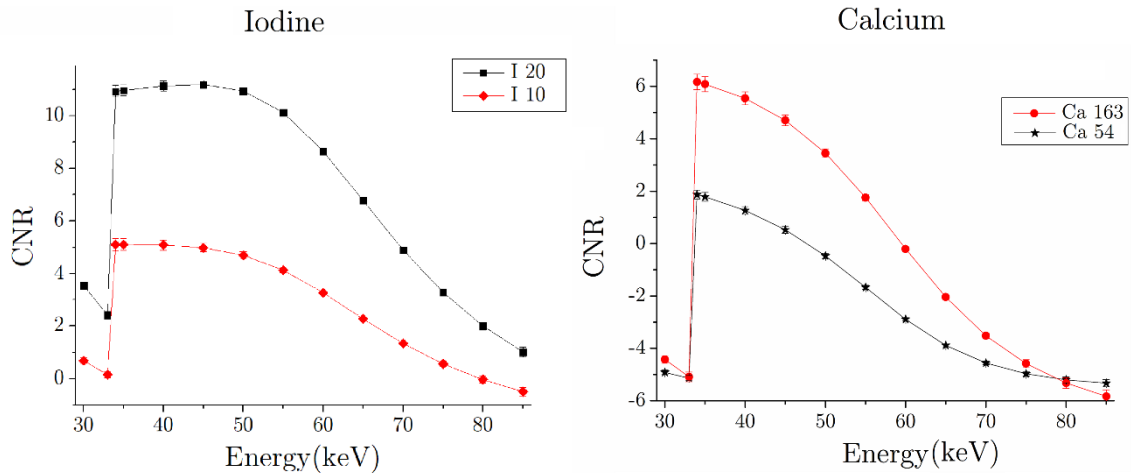


Figure 49. CNR as a function of the energy of the virtual monochromatic images obtained from simulations.

The CNR curves presented in Figure 49 present the results of the calcium inserts and the iodine inserts I-10 and I-20. The CNR of the inserts I-25 and I-12.5 are not presented as they are positioned closer to the phantom external surface and the beam hardening artefacts are stronger in such inserts.

The maximum CNR was found at the optimal energy of 40 keV for the iodine inserts in the real images. Such maximum was not observed in the calcium inserts. In the case of the simulated images the energy of maximum CNR was 34 keV but it is due to the K-border peak of iodine in the I-10 insert. The I-20 insert presented maximum CNR at 45 keV.

4 CONCLUSIONS

There were presented the features of the construction of a modelled CT device which intends to replicate the acquisition process of a rapid kV switching DECT device. Most of the features of the clinical device were obtained from its technical manual, but there was no information about the bowtie filter. The bowtie filter shape and material were modelled and its position was assessed in two steps. From the analysis of the detectors energy deposition, three positions were selected as the ones which better homogenizes the energy deposited in the detectors. The three positions were selected as their uncertainty did not allow discerning which position was better. Then, the $CTDI_{100,c}/CTDI_{100,p}$ was assessed in a simulated PMMA phantom for the three filter positions. Comparing to the results obtained by Kramer et al. (Kramer et al., 2017), the position 10 cm was selected as it presented the most similar $CTDI_{100,c}/CTDI_{100,p}$ values. The percentage differences obtained from the comparison of $CTDI_{100,c}/CTDI_{100,p}$ were up to 6.5%. Since there were differences in the geometry and material of the bowtie filters of this work and Kramer et al. the percentage differences were considered acceptable for the imaging purposes of the present work.

After defining the characteristics of the modelled CT, studies of DECT differentiation properties in phantoms were performed. The first phantom in which the DECT properties were studied was a water phantom with inserts of an iodine contrast agent. Some features of the images were:

- The standard images acquired from such phantom presented beam hardening artefacts, especially in the 80 kV image;
- The material concentration images were obtained using both Image-Based and Projection-Based BMD methods for water and iodine. The spatial differences in the material concentration images were associated to the BMD algorithms. The linearity of the iodine concentration of the images was used to calibrate the concentration; and
- The monoenergetic images are linear combination of the material concentration images weighted by the mass attenuation coefficient of water and iodine. There are energies where the monoenergetic images exhibited behaviour similar to the standard images with a reduction of the beam hardening artefacts. In addition, it was observable that at high energies, the mononenergetic images presented a dominant contribution of the water concentration image, generating monoenergetic images where the iodine inserts attenuated less than water. At low energies, the iodine concentration image was the dominant contribution in the monoenergetic images.

The second analysis of the DECT methods in the modelled CT consisted in a comparison of the images when a real phantom was imaged and a similar one was simulated. There were performed a comparison of the images obtained from the real device and for the simulations. Some features of the images of this comparison were:

- In the standard CT images, the mean HU levels were compared. The standard images acquired from the simulations presented agreement in the mean HU level in the inserts containing iodine for the 140 kV spectra. The differences of the 80 kV were attributed to the different bowtie filter and spectra of the simulated and real device. The differences obtained for the calcium inserts were attributed to the possible differences in the simulated and real composition of the materials used in the inserts and to the inhomogeneity of the density along calcium inserts;
- The Projection-Based BMD method was carried out using the mass attenuation coefficients of water and iodine. The measured concentration in the iodine inserts agreed with the expected ones in both real device and simulated images. In the case of the concentration obtained from the simulated images, even when the concentration of some inserts differed from the expected, their t values were less than the critical t due to their uncertainty. The mean concentration in both real device and simulated images were acquired applying a calibration factor;
- The second pair of materials used to perform the BMD was water-calcium. In this case, neither the concentration from the real image nor the concentration from the simulations agreed with the expected concentration values of the calcium inserts. In the case of the simulations, no previous calibration was done for calcium materials, and then the values could not be directly compared. The differences in the concentration obtained from the real images can be attributed to the systematic errors in the preparation of the calcium inserts, and on the material composition itself;
- A qualitative result of the material concentration images was the presence of beam hardening artefacts in the iodine and calcium concentration images obtained from simulations and the presence of the “inverse hardening artefact” in both water concentration images obtained from simulations;
- As in the case of the water-iodine phantom, it was found that for high energies, the water component dominated in the monoenergetic images and for low energies, the iodine contribution dominated. This behaviour was present in both simulated and real device images; and
- The CNR was measured in the monoenergetic images as a function of the energy. In the real images, the optimal energy which produced maximum CNR for the iodine inserts was 40 keV. In the case of the simulated images, 34 keV was the

energy that maximizes CNR in the I-10 insert, but it was due to the energy of the K-border of the attenuation coefficient of iodine. The insert I-20 exhibited maximum CNR at 45 keV.

Finally, it is possible to conclude that the simulated DECT model presents qualitative results similar to the obtained in the real device. There are limitations in the material concentration images which generate limitations in the virtual monoenergetic images. For future works it would be important to:

- Implement beam hardening corrections in the simulated CT images to avoid the beam hardening artefacts in the material concentration images and to avoid the underestimation of the CNR of the inserts positioned close to the phantom external surface; and
- Include the calibration of calcium considering materials such as calcium hydroxyapatite. It would be necessary to simulate different concentrations which will allow a detailed characterization. It would allow the assessment of quantitative results in the simulation of calcium concentration materials.

In general, the modelled CT system permits exploring the images characteristic with different materials and compositions. It can also be used as a didactic tool to improve the understanding of the material differentiation in spectral and DECT. Due to the flexibility of the modelled CT system, it would be interesting to carry out simulations using monoenergetic photons to acquire monoenergetic images and compare them with the virtual monoenergetic images obtained with the DECT method.

It will be also possible to perform simulations of spectral CT using more than two spectra imaging a phantom. Or even perform Spectral CT simulations by using only one spectrum and defining the detectors as a Phase Space surface. In such case, the energetic separation would be performed by an external program which reads the particle information of the PSFs of the detectors and separates them in the defined energy channels.

REFERENCES

- AAPM, (1977). *Phantoms for performance evaluation and quality assurance of CT Scanners*. Report (1),1-27
- AAPM, (2008). *The Measurements, Reporting, and Management of radiation Dose in CT*. Report (96),1-34
- AAPM, (2011). *Size-Specific Dose Estimates (SSDE) in Pediatric and Adult Body CT Examinations*. Report (204),1-30
- AAPM, (2014). *Use of Water Equivalent Diameter for Calculating Patient Size and Size-Specific Dose Estimates (SSDE) in CT*. Report (220),1-23
- Alvarez, R. (1976). *Energy-selective reconstructions in X-ray computerised tomography*. *Physics in Medicine and Biology*, 21(5), 733. Doi: 10.1088/0031-9155/21/5/002
- Anastacio, Quimica (2017). *Especificação Técnica Negro de Fumo N550*. Brazil.
- Attix, F. (2004). *Introduction to Radiological Physics and Radiation Dosimetry*. WILEY-VCH. Weinheim.
- Bayer, (2012). *ULTRAVIST®*, *Iopromide*. New Zealand Limited.
- Bazalova, M., and Verhaegen, F. (2007) *Monte Carlo simulation of a computed tomography x-ray tube*. *Physics in Medicine & Biology*, 52(19) Doi: 10.1088/0031-9155/52/19/015
- Berger, M., Hubbell, J., Seltzer, S., Chang, J., Coursey, J., Sukumar, R., Zucker, D., and Olsen, K. (2010), *XCOM: Photon Cross Section Database* (version 1.5). [Online] Available: <http://physics.nist.gov/xcom> [2018, March 20]. National Institute of Standards and Technology, Gaithersburg, MD.
- Bradley, W. (2008). *History of Medical Imaging*. *Proceedings of the American Philosophical Society*, 152(3), 349-361.
- Bushberg, J., Seibert, J., Jr. Leidholdt., & Boone, J. (2011). *The Essential Physics of Medical Imaging* (2nd ed.). Philadelphia: Lippincott Williams & Wilkins.
- Buzug, T. (2008). *Computed Tomography: From Photon Statistics to Modern Cone-Beam CT*. Springer.
- Caldas, E. (2008). *Study and application of the FDK algorithm for the reconstruction of multi-section tomographic images*. (Master), University of São Paulo, USP, Brazil. Retrieved from: <http://www.teses.usp.br/teses/disponiveis/43/43134/tde-10032009-132445/pt-br.php>
- Caldas, E., Costa, P. (2010). *Application of the FDK algorithm for the reconstruction of tomographic images*. *Brazilian journal of biomedical engineering* (26)105–120 Doi: 10.4322/rbeb.2012.084
- Carbonates, Imerys (2015). *SUPERMICRO® 230*. In.
- Chandra, N., & Langan, D. (2011). *Gemstone Detector: Dual Energy Imaging via Fast kVp Switching*. In T. Johnson, C. Fink, S. Schönberg, & M. Reiser (Eds.), *Dual Energy CT in Clinical Practice* (pp. 35-41). Berlin, Heidelberg: Springer Berlin Heidelberg.
- Cormode, D., Si-Mohamed, S., Bar-Ness, D., Sigovan, M., Naha, P., Balegamire, J., Lavenne, F., Coulon, P., Roessler, E., Bartels, M., Rokni, M., Bleviss, I., Bousset, L., Douek, P.(2017). *Multicolor spectral photon-counting computed tomography: in vivo dual contrast imaging with a high count rate scanner*. *Scientific Reports*, 7(1) 4784. Doi: 10.1038/s41598-017-04659-9
- Costa, P. (1993). *Generalized model for geometric efficiency in computed tomography* (Master), University of São Paulo, USP, Brazil.

- Costa, P., Nersissian, D., Salvador, F., Rio, P., & Caldas, L. (2007). *Generation of calibrated tungsten target X-ray spectra: Modified TBC model*. Health Physics, 92(1), 24-32. Doi: 10.1097/01.HP.0000231565.66004.f9
- Deans, S. (1993). *The Radon Transform and Some of Its Applications*. Krieger Publishing Company.
- Demirkaya, O., Asyali, M. and Sahoo, P. (2008). *Image Processing with MATLAB @ Applications in Medicine and Biology*. CRC Press, Taylor and Francis Group. Florida USA.
- Dixon, R., Munley, M., & Bayram, E. (2005). *An improved analytical model for CT dose simulation with a new look at the theory of CT dose*. Medical Physics, 32(12), 3712-3728. doi:10.1118/1.2122507
- Ehn, S., Sellerer, T., Muenzel, D., Fingerle, A., Kopp, F., Duda, M., Mei, K., Renger, B., Herzen, J., Dangelmaier, J., Schwaiger, B., Sauter, A., Riederer, I., Renz, M., Braren, R., Rummeny, E., Pfeiffer, F., Noël, P. (2017) *Assessment of quantification accuracy and image quality of a full-body dual-layer spectral CT system*. Journal of Applied Clinical Medical Physics, 19(1). DOI: 10.1002/acm2.12243
- Farma, Adv (2017). Saline solution especifications. <http://www.advfarma.com.br/medicamentos/medicamentos-de-notificacao-simplificada/agentes-de-irrigacao/soro-fisiologicos-cloreto-de-sodio/>.
- Ferreira, C., Galvao, L., Veira, J. and Maia, A. (2010). *Validation of an exposure computational model to computed tomography dosimetry*. Brazilian Journal of Medical Physics 4(1):19-22.
- Fornaro, J., Leschka, S., Hibbeln, D., Butler, A., Anderson, N., Pache, G., & Stolzmann, P. (2011). *Dual and multi-energy CT: approach to functional imaging*. Insights into Imaging, 2(2), 149-159. Doi:10.1007/s13244-010-0057-0
- Fuchs, T., Stehli, J., Fiecher, M., et al. *First experience with monochromatic coronary computed tomography angiography from a 64-slice CT scanner with Gemstone Spectral Imaging (GSI)*. Journal of Cardiovascular Computed Tomography, 7(1), 25 – 31. Doi: 10.1016/j.jcct.2013.01.004
- Journal of Cardiovascular Computed Tomography , Volume 7 , Issue 1 , 25 - 31
- Fu, W., et al. (2017) *Estimation of breast dose reduction potential for organ-based tube current modulated CT with wide dose reduction arc*. Physics of Medical Imaging (Proceedings) 10132(46) Doi:/10.1117/12.2255797
- Gammex (2015). CT Dual Energy Phantom. CT QA Solution. Retrieved from: <http://snc4quarter.sunnuclear.net/documents/datasheets/gammex/ct'dual'energy'phantom.pdf> In: Sun Nuclear Company.
- Gammex (2017). Multi-Energy CT phantom. In: Sun Nuclear Company.
- GE Company (2011). GE Healthcare Discovery CT 750 HD. In. Waukesha, USA.
- GE Company (2015). GE Healthcare Discovery CT 750 HD. Technical Reference Manual.
- Gong, B., Yuhao, W., O'Keeffe, M., Berger, F., et al. *Top 50 Highly cited Articles on Dual Energy Computed Tomography (DECT) in Abdominal Radiology: A bibliometric Analysis*. Polish Journal of Radiology, 82, 748-759. Doi:10.12659/PJR.904075.
- Heismann, B., Schmidt, B., & Flohr, T. (2012). *Spectral Computed Tomography* (Vol. PM226): SPIE PRESS BOOK.
- Helene, O., & Vanin, V. (1991). *Tratamen to Estatístico de Dados em Física Experimental*. São Paulo, Brazil.: Blucher.
- Hubbell, J. (1969). *Photon Cross Section, Attenuation Coefficients, and Energy Absorption Coefficients From 10keV to 100 GeV*. Retrieved from Washington D.C.: <https://srd.nist.gov/NSRDS/NSRDS-NBS29.pdf>

- Hurrell, M., Butler, A., Cook, N., Butler, P., Ronaldson, J., & Zainon, R. (2012). *Spectral Hounsfield units: a new radiological concept*. *European Radiology*, 22(5), 1008-1013. doi:10.1007/s00330-011-2348-3
- ICRP (2007). *Managing Patient Dose in Multi-Detector Computed Tomography (MDCT)*. In (Vol. 102): International Commission on Radiation Protection.
- ImpactScan. (2017). CT-Dosimetry. <http://www.impactscan.org/#ctdose> Retrieved in April 2017
- Johnson, T. (2007). *Material differentiation by dual energy CT: initial experience*. *European Radiology*, 17(6), 1510. DOI:10.1007/s00330-006-0517-6
- Johnson, T. (2012). *Dual-Energy CT: General Principles*. *American Journal of Roentgenology*, 199(5 supplement), S3-S8. doi:10.2214/AJR.12.9116
- Johnson, T., & Kalender, W. (2011). *Physical Background*. In: T. Johnson, C. Fink, S. Schönberg, & M. Reiser (Eds.), *Dual Energy CT in Clinical Practice* (pp. 3-9). Berlin, Heidelberg: Springer Berlin Heidelberg.
- Kalender, W. (2011). *Computed Tomography; Fundamentals, System Technology, Image Quality and Applications* (Publicis Ed. third ed.). Erlangen.
- Kalender, W., Kolditz, D., Steiding, C., Ruth, V., Lück, F., Rößler, A., Wenkel, E. (2017). *Technical feasibility proof for high-resolution low-dose photon-counting CT of the breast*. *European Radiology* 27(3) 1981-1086. Doi: 10.1007/s00330-016-4459-3
- Kim, S., Yoshizumi, T., Yin, F., & Chetty, I. (2013). *Spiral computed tomography phase-space source model in the BEAMnc/EGSnrc Monte Carlo system: implementation and validation*. *Physics in medicine and biology*, 58(8), 2609. Doi: 10.1088/0031-9155/58/8/2609
- Kramer, R., Cassola, V., Andrade, M., Araújo, M., Brenner, D., & Houry, H. (2017). *Mathematical modelling of scanner-specific bowtie filters for Monte Carlo CT dosimetry*. *Physics in Medicine and Biology*, 62(3), 781. Doi:10.1088/1361-6560/aa5343
- Krauss, B., Schmidt, B., & Flohr, T. G. (2011). *Dual Source CT*. In T. Johnson, C. Fink, S. Schönberg, & M. Reiser (Eds.), *Dual Energy CT in Clinical Practice* (pp. 11-20). Berlin, Heidelberg: Springer Berlin Heidelberg.
- Landry, G., et al (2011). *Extracting atomic numbers and electron densities from a dual source dual energy CT scanner: Experiments and a simulation model*. *Radiotherapy and Oncology* , 100(3) , 375 – 379.
- Lee, Y., Park, K., Song, H., Kim, S. & Suh, J. (2012). *Metal artefact reduction in gemstone spectral imaging dual-energy CT with and without metal artefact reduction software*. *European Radiology*, 22(6), 1331–1340. Doi: 10.1007/s00330-011-2370-5
- Marin, D. (2014). *State of the art: dual-energy CT of the abdomen*. *Radiology*, 271(2), 327. Doi: 10.1148/radiol.14131480.
- McCollough, C., Leng, S., Yu, L., Cody, D., Boone, J., & McNitt-Gray, M. (2011). *CTDIvol, DLP, and Effective Dose Are Excellent Measures for Use in CT Quality Improvement Response*. *Radiology*, 261(3), 999-1000. Doi: 10.1148/radiol.11111055.
- McCollough, C., Leng, S., Yu, L., Fletcher, J. (2015). *Dual- and Multi-Energy CT: Principles, Technical Approaches, and Clinical applications*. *Radiology*, 276(3), 637-653. *Physics in Medicine & Biology*, 62(5). Doi: 10.1088/1361-6560/aa5911
- McMillan, K., McNitt-Gray, M. and Ruan, D. (2016). *Development and validation of a measurement-based source model for kilovoltage cone-beam CT Monte Carlo dosimetry simulations*. *Medical Physics*, 40(11). Doi: 10.1118/1.4823795

- Ming, X., Feng, Y., Liu, R., Yang, C., et al. (2017). *A measurement-based generalized source model for Monte Carlo dose simulations of CT scans*. *Physics in Medicine and Biology* 62(5). Doi: 10.1088/1361-6560/aa5911
- Nelson, G., & Rewy, D. (1965). *Gamma-Ray Interactions with Matter*. In K. Siegbann (Ed.), *Alpha, Beta and Gamma Ray Spectrometry*. Amsterdam.
- Nicolaou, S., Co, S., & Hou, D. (2011). *Gout*. In T. Johnson, C. Fink, S. Schönberg, & M. Reiser (Eds.), *Dual Energy CT in Clinical Practice* (pp. 199-213). Berlin, Heidelberg: Springer Berlin Heidelberg.
- Oppelt. (2005). *Imaging Systems for Medical Diagnosis: Fundamentals and Technical Solutions – X-Ray Diagnostics– Computed Tomography – Nuclear Medical Diagnostics – Magnetic Resonance Imaging – Ultrasound Technology* (A. Oppelt Ed.). Erlagen: SIEMENS.
- Philips, IQon Spectral CT. <http://www.spectralctlearningcenter.philips.com/> Retrieved in November 2017.
- Pourmorteza, A., Symons, R., Sandfort, R., Mallek, M., Fuld, M. et al.(2016). *Abdominal Imaging with Contrast-enhanced Photon-counting CT: First Human Experience*. *Radiology* 279(1), 239-245. Doi: 10.1148/radiol.2016152601
- Rebuffel, V., Rinkel, J., Tabary, J., & Verger, L. (2011). *New Perspectives of X-ray Techniques for Explosive Detection Based on CdTe/CdZnTe Spectrometric Detectors*. In. International Symposium on Digital Industrial Radiology and Computed Tomography, Berlin.
- Radon, J. (1917). Über die Bestimmung von Funktionen durch ihre Integralwerte längs gewisser Mannigfaltigkeiten. *Berichte Sächsische Gesellschaft der Wissenschaften. Leipzig, Math. –Phys. Kl.*(69) 262–277.
- Salvat, F., Fernández-Varea, J. M., & Sempau, J. (2011). PENELOPE: A Code System for Monte Carlo Simulation of Electron and Photon Transport. *OECD Nuclear Energy Agency*.
- Sarrut, D. , Bardies, M. , Bousson, N. , Freud, N. et al.(2014). *A review of the use and potential of the GATE Monte Carlo simulation code for radiation therapy and dosimetry applications*. *Med. Phys.*, (41) 064301. Doi:10.1118/1.4871617
- Schlomka, J., Roessl, E., Dorscheid, R., Dill, S., Martens, G., Istel, T., Proksa, R. (2008). *Experimental feasibility of multi-energy photon-counting K-edge imaging in pre-clinical computed tomography*. *Physics in Medicine & Biology*. 53(15):4031-47. Doi: 10.1088/0031-9155/53/15/002
- Schneider, D., Apfaltrer, P., Sudarski, S., Nance, J. W., Haubenreisser, H., Fink, C., Henzler, T. (2014). *Optimization of Kilolectron Volt Settings in Cerebral and Cervical Dual-energy CT Angiography Determined with Virtual Monoenergetic Imaging*. *Academic Radiology*, 21(4), 431-436. Doi: 10.1016/j.acra.2013.12.006
- Sechopoulos, I., Vedantham, S., Suryanarayanan, S., et al. (2008). *Monte Carlo and Phantom Study of the Radiation Dose to the Body from Dedicated CT of the Breast*. *Radiology*, 247(1). Doi: 10.1148/radiol.2471071080
- Sempau, J., Badal, A. and Brualla, L. (2011). *A PENELOPE-based system for the automated Monte Carlo simulation of clinacs and voxelized geometries-application to far-from-axis fields*. *Medical Physics* 38(11) 5887-5895. Doi: 10.1118/1.3643029
- Shimomura, K., Araki, F., Kono, Y., Asai, Y., Murakami, T., Hyodo, T., Nishimura, Y. (2017). *Identification of elemental weight fraction and mass density of humanoid tissue-equivalent materials using dual energy computed tomography*. *Physica Medica* (39)1-174. Doi: 10.1016/j.ejmp.2017.05.060
- Sookpeng, S., Cheebsumon, P., Pengpan, T., Martin, C. (2016). *Comparison of computed tomography dose index in polymethyl methacrylate and nylon dosimetry phantoms*. *Journal of Medical Physics/Association of Medical Physicists of India*. 41(1):45-51. Doi: 10.4103/0971-6203.177287

- The Phantom Laboratory (2014). Catphan ® 500 and 600 Manual. New York. US.
- Tucker, D. M. (1991). Semiempirical model for generating tungsten target x-ray spectra. *Medical Physics*, 18(2), 211.
- Verhaegen, F. and Slobodan, D. (2005). *Sensitivity study for CT image use in Monte Carlo treatment planning*. *Physics in Medicine & Biology* (50)5, 937-946. Doi: 10.1088/0031-9155/50/5/016
- Vieira, A., Linke, A., Yoshimura, E., Terini, R., & Herdade, S. (2011). *A portable Compton spectrometer for clinical X-ray beams in the energy range 20–150keV*. *Applied Radiation and Isotopes*, 69(2), 350–357. Doi: 10.1016/j.apradiso.2010.10.011
- Vieira, D. (2016). Desenvolvimento de um sistema automatizado de análise da qualidade de imagens tomográficas. (Master of Science), University of São Paulo
- Vlassenbroek, A. (2011). Dual Layer CT. In T. Johnson, C. Fink, S. O. Schönberg, & M. F. Reiser (Eds.), *Dual Energy CT in Clinical Practice* (pp. 21-34). Berlin, Heidelberg: Springer Berlin Heidelberg.
- Yu, L., Christner, J., Leng, S., Wang, J., Fletcher, J., & McCollough, C. (2011). *Virtual monochromatic imaging in dual-source dual-energy CT: Radiation dose and image quality*. *Medical Physics*, 38(12), 6371-6379. doi:10.1118/1.3658568
- Yu, Z., Leng, S., Jorgensen, S., et al. (2016). *Evaluation of conventional imaging performance in a research whole-body CT system with a photon-counting detector array*. *Physics in Medicine & Biology* 61(4), 1572. Doi:10.1088/0031-9155/61/4/1572
- Zhang, D., Li, X. & Liu, B. (2011). *Objective characterization of GE Discovery CT750 HD scanner: Gemstone spectral imaging mode*. *Medical Physics*, 38(3), 1178-1188. Doi: 10.1118/1.3551999

APPENDIXES

A. CT IMAGE CHARACTERIZATION

This section presents the methodology and results of the characterization performed in order to be confident in the regime of work of 10^9 initial particles. The characterization consists in the analysis of image properties as a function of the number of initial particles. The number of initial particles is also called number of histories.

A.1 Methodology

Simple geometry simulations were performed in order to characterize the image properties as a function of the number of histories. The simple geometry refers to a cylindrical water phantom containing a material insert in the centre, as presented in Figure A-1. Such geometrical configuration of the phantom presents angular symmetry. When a phantom with this symmetry is irradiated all the projections are similar, despite small variations caused by the noise.

The cylindrical symmetry was intentionally selected to enable the single projection reconstruction. Due to the cylindrical symmetry, at any projection angle, the phantom would attenuate the beam in an equivalent way, and the energy deposited in the detectors would be similar. Then, for simplicity and to save time, for each image, just a single projection was acquired. The information of the projection was replicated to generate the sinogram. As a consequence of using a single projection reconstruction, it is expected that the reconstructed images would present polar symmetry or could be described as composed of rings.

As each projection meant a simulation, the single projection assumption reduced drastically the simulation time, especially for the simulations with the larger numbers of histories. For example, the projection obtained with the water phantom and the bone insert with 10^{10} histories took 8 hours of computation, using the single projection reconstruction. If the image were obtained using 360 simulation angles the simulation time would take 12 days (using 10 cores of the computer server).

Once the sinogram was simulated the images were reconstructed using the FBP, for simplicity in this text the images which are reconstructed from the simulated sinograms are called “simulated images”.

There were obtained simulated images of a water phantom of 16 cm diameter containing a central cylindrical insert (1 cm diameter) of one of the following materials: bone, nylon, PMMA, polyethylene and water. The phantom with the water insert represented a homogeneous water phantom. There were reconstructed images for 80 and 140 kV and for 10^6 , 10^7 , 10^8 , 10^9 and 10^{10} number of histories.

For the simulations with 10^6 to 10^9 histories the PSF used was the one of 10^9 and the number of initial histories was restricted in the input files to reach the number of particles desired in each case. For the 10^{10} PSF was necessary a different approach.

The generation of a PSF corresponding to 10^{10} initial histories required computational times of 50-60 days (using just one core of the server). Thus, ten PSF of 10^9 histories were simulated in parallel. As each PSF consists in a list of the particles and its physical features, the PSFs were joined using Matlab®. The joined PSF is then the equivalent to a PSF generated using 10^{10} initial histories.

To guarantee the statistical independence of the particles in each PSFs of 10^9 histories, specific seeds were used in each simulation. The periodicity of the random generator of FORTRAN 77 is close to 10^{18} . Therefore, it was possible to use as seeds the values that the generator would return to every 10^{13} sequence steps. More information about the seeds and the random generator are found in the PENELOPE manual (Salvat et al., 2011).

The parameters CNR and SNR, mentioned in section 1.1.5, were calculated from the simulated images. To study the image properties, specific regions were defined to compute SNR and CNR as defined in section 1.1.5. Such regions are shown in Figure A-1, in this case the regions defined were circles. The mean value and standard deviation on each region were computed using Matlab®.

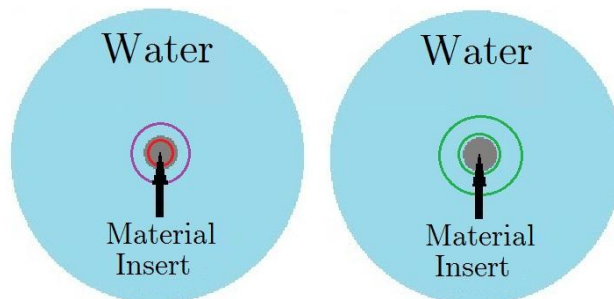


Figure A-1. Representation of the simulated water phantom with a material insert in the centre, the regions used to compute SNR and CNR are shown in different colours. The region bounded by the green circumferences defines the background ROI. The region bounded by the red circumference defines the ROI for the CNR calculation. The violet curve bounds the region defined as ROI for SNR calculation.

A.1.1 Reconstructed images of bone and water

DECT reconstructions were performed for the simulated water phantom described in the previous pages which contain a bone insert. The simulated phantom is presented in Figure A-1. It corresponds to a 16 cm diameter water cylinder with a central cylindrical bone insert of 1 cm diameter. The materials used to perform the BMD were cortical bone and water. The mass attenuation coefficients of both materials were obtained using the XCOM database (Berger M. et al., 2017). The energy dependence of the mass attenuation coefficients is found in Figure A-2. The material concentration images were solved using the BMD methods described in sections 1.3.1 and 1.3.2.

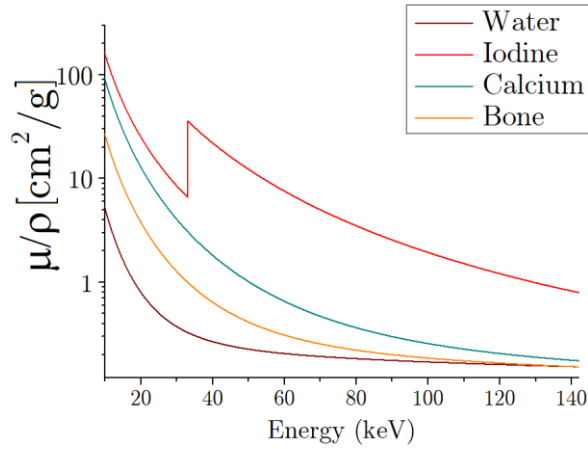


Figure A-2. Mass attenuation coefficients as a function of the energy of the materials that are used to perform the BMD in the present work. The K–border of iodine is observed at 33.2 keV. The functions were obtained from the database XCOM (Berger M. et al., 2017)

This procedure was adopted to explore how the definition of the insert and image contrast change using the BMD methods when the reconstruction is performed using 10^9 and 10^{10} histories. Images were reconstructed using both Projection–Based and Image–Based BMD methods.

A.2 Results

This section presents the results concerning the two characterizations described in section A.1. In the first one, CNR and SNR are studied as functions of the number of histories used to perform the Monte Carlo simulations. The second one consists on studying how the number of histories affects the dual energy images of a water phantom with a bone insert.

A.2.1 Characterization of CT images: Contrast and Noise

As mentioned in section A.1, an initial characterization of the CT images was performed to understand how the number of initial histories affects the reconstructed images. The images were simulated by varying the number of histories from 10^6 to 10^{10} .

The simulated standard images for the 80 kV and 140 kV spectra, for 10^6 to 10^{10} initial histories, are shown in Figure A-3 and Figure A-4.

It is possible to note how the number of histories improves the image definition. As the images were reconstructed using just one projection, the images presented artefacts with polar symmetry (rings). The artefacts are more evident in the images acquired using 10^6 and 10^7 initial histories but are present in all the images. The rings presented in the images of 10^{10} images are smoother than the ones of the images of 10^6 histories.

As the single projection reconstruction was implemented, the sinograms were generated replicating a single projection 360 times. As the energy deposited in the detectors vary from a detector to other, such variation are again replicated in the sinogram, and as a consequence the reconstructed image presents rings. Then, the rings present in the reconstructed images are a direct consequence of the single projection reconstruction.

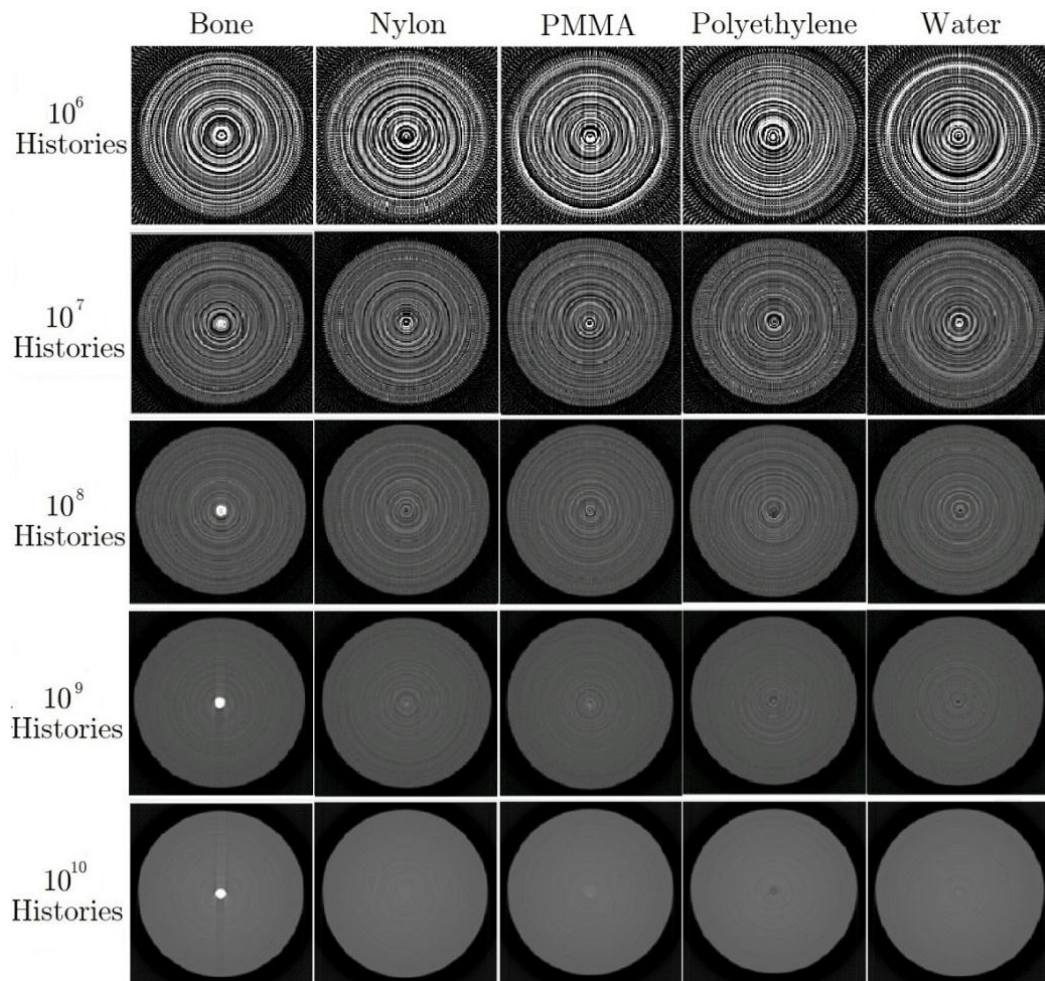


Figure A-3. Reconstructed images of a water phantom of 16 cm diameter obtained for the 80 kV spectrum. The phantom contained a central insert of a material of 1 cm diameter. In the upper part, the name represents the material of the insert and the information on the left the number of initial histories used for the simulations. Image size is 160 x160 pixels, L/W: 250HU/1250HU.

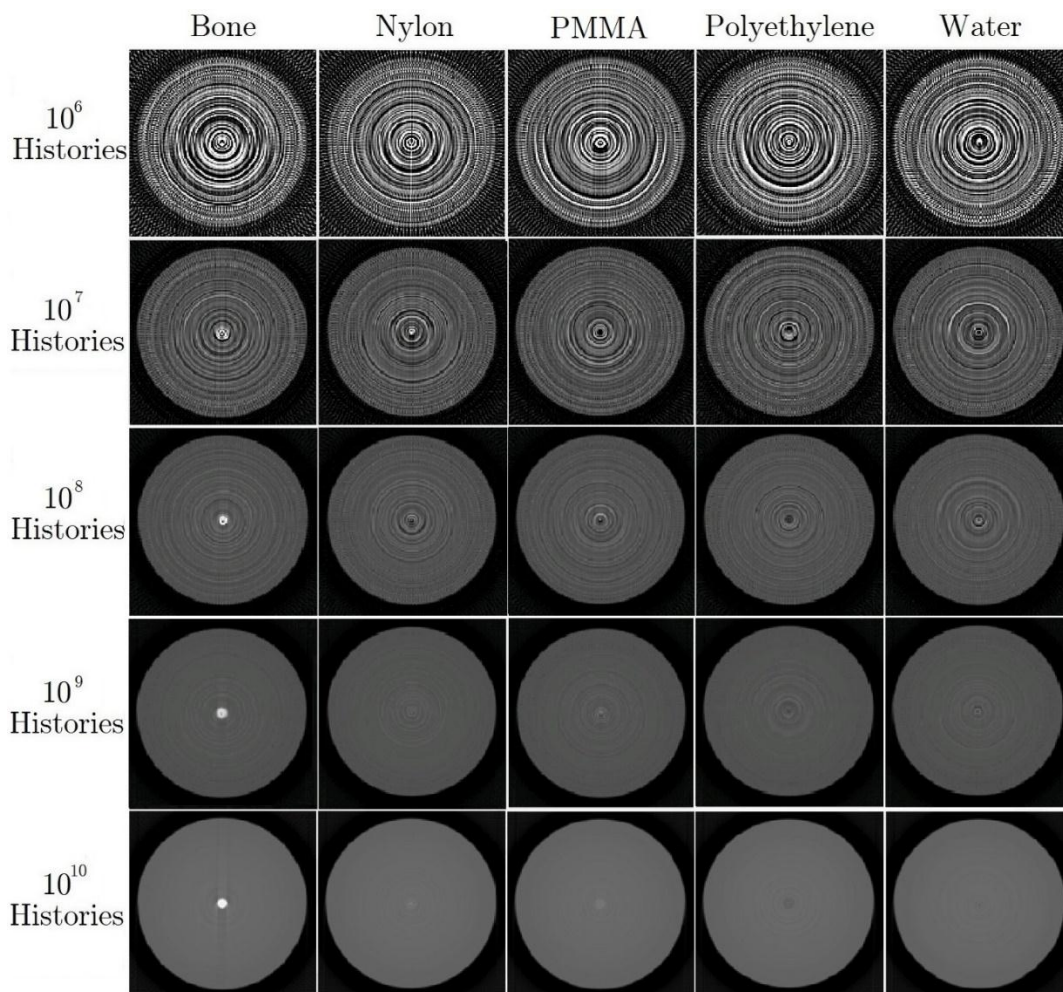


Figure A-4. Reconstructed images of a water phantom of 16 cm diameter obtained for the 140 kV spectrum. The phantom contained a central insert of a material of 1 cm diameter. In the upper part, the name represents the material of the insert and the information on the left the number of initial histories used for the simulations. Image size is 160 x160 pixels, L/W: 250HU/1250HU.

Contrast to noise ratio CNR and Signal to noise ratio SNR

The parameters CNR and SNR were evaluated in the simulated images (Figure A-3 and Figure A-4). CNR and SNR were calculated as described in section 1.1.5, for each material insert and number of histories. The ROIs used for such calculations are presented in Figure A-1. Uncertainties of the CNR and SNR values were derived from the uncertainties of the ROIs involved in the calculations, as presented in Appendix A.3. Figure A-5 and Figure A-6 show the CNR and SNR as a function of the initial number of histories.

Figure A-5 presents the CNR as a function of the number of histories for the mentioned material inserts. The tendency of CNR to increase as increasing the number of histories is clear for bone, Figure A-5a. For Nylon (Figure A-5c) and PMMA (Figure A-5b), the CNR seems to increase as increasing the number of histories from 10^8 to 10^{10} histories.

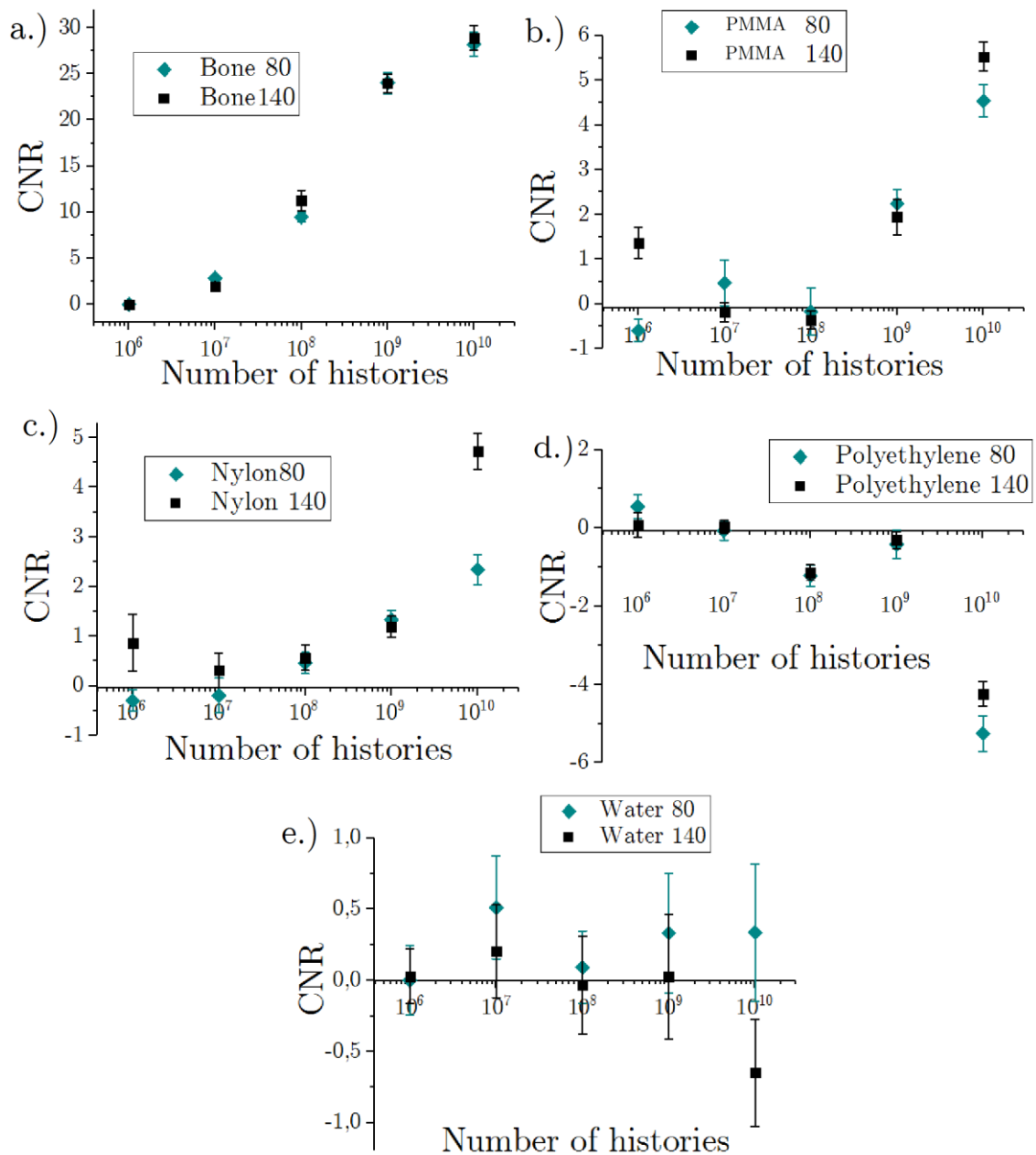


Figure A-5. CNR as a function of the number of initial histories in a water phantom with a material insert of a.) Bone, b.) PMMA, c.) Nylon, d.) Polyethylene and e.) Water (representing a uniform phantom). The CNR was calculated as presented in equation (14), defining the ROIs shown in Figure A-1.

The attenuation coefficient of polyethylene is less than water. Then, the mean HU inside the polyethylene insert is less than that of water (background). This fact explains the negative signs in the calculated CNR in Figure A-5d for 10^8 to 10^{10} .

The CNR values for water (Figure A-5e) are close to zero (from -0.7 to 0.5). This behaviour is expected as both ROIs involved in the calculation of the CNR contain the same material (representing a uniform water phantom). Then a CNR approximately zero is expected.

It is possible to conclude that the CNR increase as increasing the number of histories for materials with attenuation coefficient greater than water, and the simulated CNR is greater as a material with greater attenuation coefficient is used. On the other hand, CNR negatives are obtained for materials of attenuation coefficient similar or smaller than water (polyethylene), as expected.

Figure A-6 shows the results for the SNR as a function of the number of initial histories. The behaviour of SNR for bone (Figure A-6a) is to increase as increasing the number of histories. A similar behaviour was found for SNR of PMMA (Figure A-6b) and Nylon (Figure A-6c) inserts from 10^8 to 10^{10} number of histories. Greater SNR means increased detectability of structures (Bushberg et al., 2011). It is also possible to see how the SNR value is greater for materials with greater attenuation coefficient, such as bone. SNR of bone is almost an order of magnitude greater than the other materials.

The SNR for Polyethylene (Figure A-6d) are close to zero from 10^6 to 10^9 numbers of histories and then for 10^{10} it presents clearly negative values. The negative values are expected as Polyethylene attenuates less than water. For the water insert (Figure A-6e), the SNR do not present a clear increasing or decreasing behaviour. As can be observed in Figure A-6e, the range of values the SNR of water takes is smaller than the other materials. Thus, water presents the SNR closest to zero. Then, also for polyethylene and water the obtained results agree with the expected behaviour.

It is possible to conclude that the SNR increase as increasing the number of histories for materials with attenuation coefficient greater than that of water. And SNR is greater as a material with greater attenuation coefficient is imaged. For lower attenuators than water SNR close to zero or negative were obtained.

Table A-1 presents the mean HU values of the material inserts obtained for the images of 10^9 and 10^{10} initial histories. Compact bone presents a wide range of HU values, from 200 to more than 2500 (Kalender, 2011). Then, the HU obtained for bone agree with the expected values. It is possible to note how the mean CT number of bone has lower values for higher energies, which is expected as the attenuation coefficient of bone decrease with energy. Materials in Table A-1 are organized from higher to lower attenuation coefficient μ , the less attenuating material is polyethylene and the higher attenuator is bone.

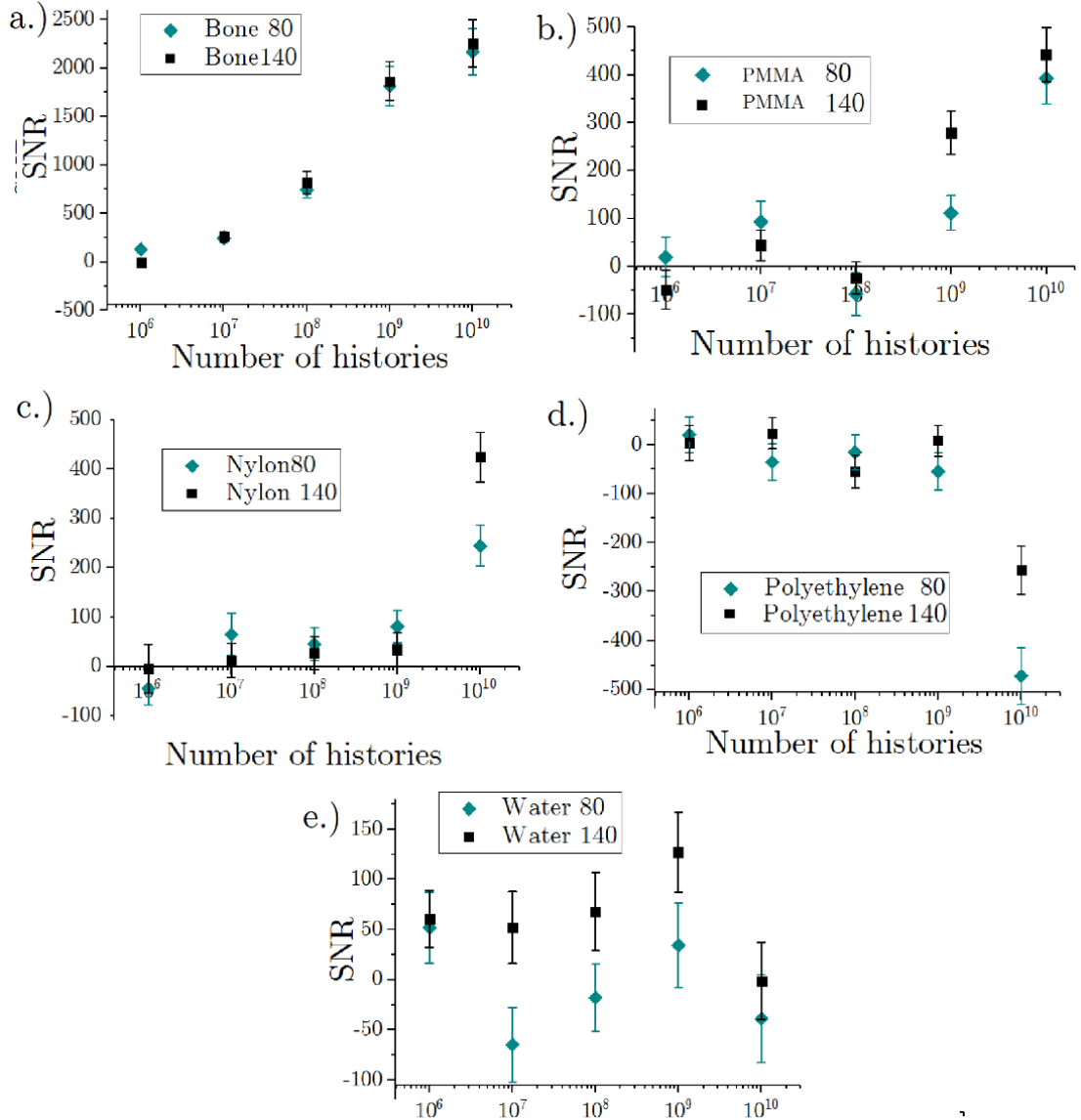


Figure A-6. SNR as a function of the number of simulated histories in a water phantom with a material insert. The materials were a.) Bone, b.) PMMA, c.) Nylon, d.) Polyethylene and e.) water (representing a uniform phantom). The SNR was calculated as presented in equation(15), with the ROIs defined in Figure A-1. It is important to remark that the vertical axis is different in the figures.

Table A-1. Mean HU obtained in the central inserts of the phantom. The mean HU values were measured in a region inside the material insert using Matlab®. The HUs were obtained for both 80 and 140 kV spectra, and for the number of histories of 10^9 and 10^{10} .

Tube Voltage	80 kV		140 kV	
Number of Histories	10^9	10^{10}	10^9	10^{10}
Bone	2838±104	2758 ± 93	1787± 56	1776 ± 60
PMMA	194 ± 27	121 ± 9	131 ± 25	145 ± 6
Nylon	130 ± 19	53 ± 8	97 ± 12	121 ± 7
Polyethylene	-75 ± 37	-157 ± 18	-32 ± 21	-83 ± 6

The user’s manual of the Catphan phantom (The Phantom Laboratory, 2014), include HU ranges of Acrylic(PMMA) of 92 to 137 HU and Low-Density Polyethylene(LDP) of –121 to –87 HU. Such ranges presented in the Catphan manual were obtained in a sample of 94 CT scans protocols, and as stated in the manual (The Phantom Laboratory, 2014), values outside such ranges are not unusual. Then, comparing the mean values obtained in PMMA of Table A-1 with the range of the Catphan manual, is possible to identify that two of the values obtained from the simulation belong to such range. For the Polyethylene, it is possible to note that even when most of the HU values are negative, they do not belong to the range presented in the Catphan manual. The range of HU for nylon was compared to the ones presented by Sookpeng et al. (Sookpeng et al., 2016). In this case, the authors found CT numbers for nylon from 60 HU to 117 HU for different phantom sizes and energies. Then, two of the mean grey values presented in Table A-1 for nylon belong to the interval.

Even when the simulations were performed using the single projection reconstruction, various mean HU values presented in Table A-1 are similar to those obtained in clinical procedures.

In the simulations of sections 3.2 and 3.3 (not using the single projection reconstruction), the number of histories used was 10^9 . At such number of histories, both CNR and SNR present the expected behaviour of increasing as the number of histories increases, for materials with attenuation coefficient greater than water. The materials used in the simulations and measurements of sections 3.2 and 3.3 follow the feature of having attenuation coefficient greater than water.

A.2.2 Reconstructed images of bone and water

A preliminary study of the DECT algorithms was performed using single projection images. As explained in previous section, both BMD methods were implemented as shown in section 1.3. Even when 10^{10} number of histories will not be used in the next section simulations, the BMD methods are applied to images of both 10^9 and 10^{10} number of histories just to present how the number of histories affects the different types of images when DECT methods are used. The different kinds of images that are mentioned in this section are explained in Figure 20.

The simulated standard images of the water phantom with the bone insert are shown in Figure A-7. Such images were simulated for 10^9 and 10^{10} histories and both spectra of 80 and 140 kV. In such figure, the simulated standard images obtained with the 80 kV spectrum present a “whiter” bone insert, which is consistent with the average values of HU presented in Table A-1. There is also possible to observe the hardening artefacts of the bone insert. The artefact can be seen as a soft shadow near the insert.

Such artefact is clearest in the 80 kV images. The 140 kV images present the material insert with less attenuation. The 140 kV image of 10^{10} number of histories presents a smoother grey colour un the region of water, the rings attributed to the single projection reconstruction are harder to see in this image than in the 140 kV image of 10^9 number of histories.

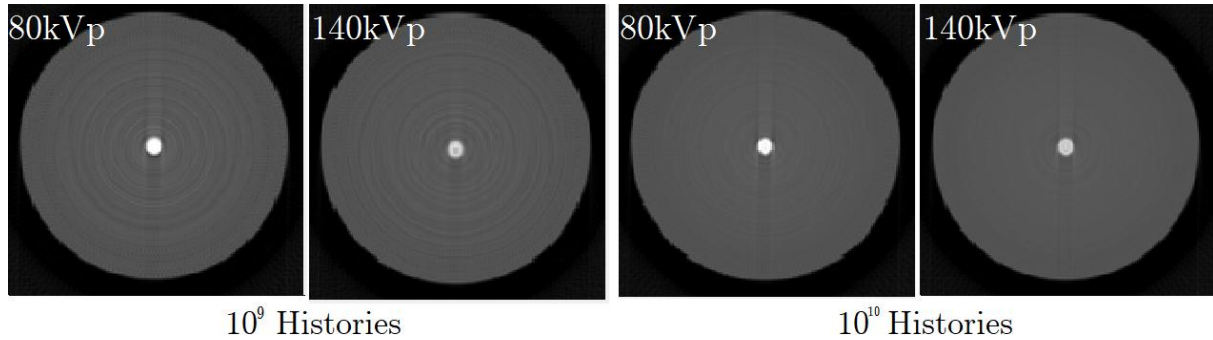


Figure A-7. Standard images for 80 and 140 kV for both numbers of histories. Image size is 160x160 pixels, L/W: 500 HU/1500 HU.

The standard deviation of the Background ROIs of the images of Figure A-7 are presented in Table A-2. This is an estimative of the noise, then it is possible to see that noise decrease for greater number of histories and for the higher kV. Then the image with less noise is the 140 kV image of 10^{10} number of histories.

Table A-2. Standard deviation on the region defined as background in the images of Figure A-7. The ROI correspondent to the Background is presented in Figure A-1.

	10^9		10^{10}	
	80 kV	140 kV	80 kV	140 kV
σ_{BG} (HU)	69	49	58	40

Material concentration images

Figure A-8 and Figure A-9 represent the materials images for both BMD methods (section 1.3) and for 10^9 and 10^{10} number of histories. Material decomposition methods create two images containing the spatial distribution of the effective concentration of each material. In a material concentration image, the pixel value is an indicator of the effective concentration of the material. The white regions indicate a high concentration of the material and the dark regions indicate a low concentration of the material.

Image-Based BMD method

Figure A-8 presents the material concentration images of water and bone obtained with the Image-Based BMD method. The “water” images represent the water concentration. Both 10^9 and 10^{10} water concentration images presented black zones in the centre, where the bone insert is located, and the water concentration is null. The size of the hole is greater for the 10^9 histories water concentration image.

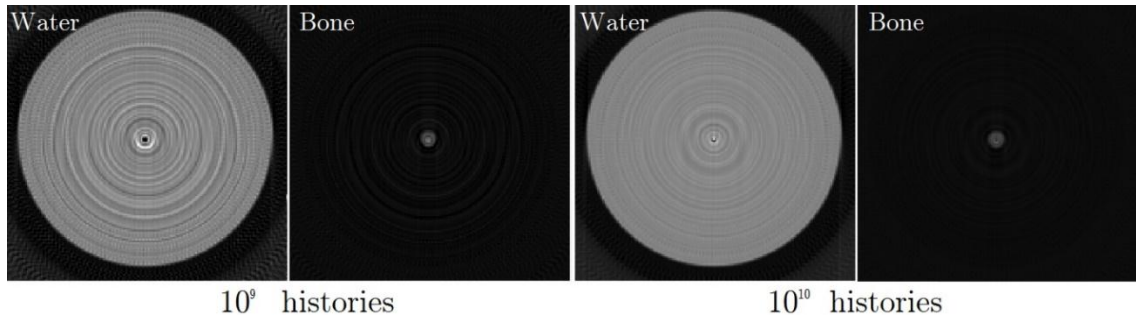


Figure A-8. Reconstructed images using the Image-Based BMD method, for 10^{10} and 10^9 histories. The reconstructed materials were water and bone. Each figure represents the spatial effective concentration of each material. Image size is 160 x160 pixels, L/W: $0.89 \text{ g cm}^{-3}/1.01 \text{ g cm}^{-3}$.

Both bone concentration images of Figure A-8 present black in the non-bone regions. The definition of the insert is similar in both bone concentration images. The difference is that the 10^9 image presents a white point in the centre, such point can be attributed to the presence or rings in the single projection images.

As presented in section 1.1.5, the noise is estimated as the standard deviation of the background. In Figure A-8 the noise was measured in the water concentration images, the noise obtained in the water concentration image of 10^{10} number of histories was the 35% of the noise obtained in the water concentration image of 10^9 number of histories.

Projection-Based BMD method

Figure A-9 presents the material images obtained with the Projection-Based BMD method (section 1.3.1). In this case, the images present some reconstruction artefacts outside the phantom region, close to the borders of the images. Such artefacts can be ignored as such region was not irradiated during the image acquisition, Figure 25 shows the detectors and the phantom, just a few detectors not belonging to the “phantom shadow” are irradiated.

The water concentration images in Figure A-9 present the hole corresponding to the bone insert. In this case, the hole size coincides with the actual size of the bone insert. It represents an improvement over the results obtained with the Image-Based BMD method (Figure A-8). The size of the holes in Figure A-8 are smaller than the actual size of the insert.

In Figure A-9, the noise obtained in the water concentration image of 10^{10} number of histories represents 40% the noise obtained in the water concentration image of 10^9 number of histories. Then, the images obtained with 10^{10} histories presents lower noise for both BMD methods.

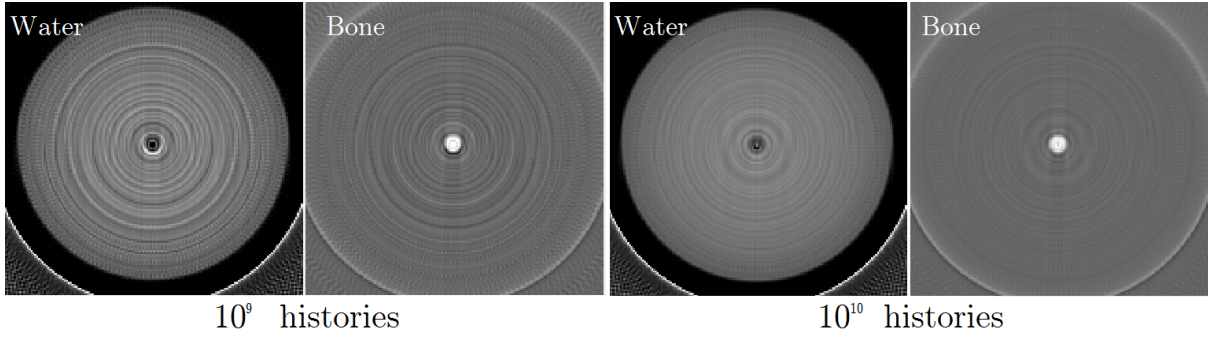


Figure A-9. Reconstructed images using the Projection-Based BMD method, for 10^{10} and 10^9 histories. The reconstructed materials were water and bone. Each figure represents the spatial effective concentration of the materials. Image size is 160 x160 pixels, L/W: $0.45 \text{ g cm}^{-3}/1.75 \text{ g cm}^{-3}$.

Monoenergetic images

The monoenergetic images are shown in Figure A-10. The images were reconstructed for 80 keV. The images obtained for 10^{10} histories seem smoother than the images obtained using 10^9 histories.

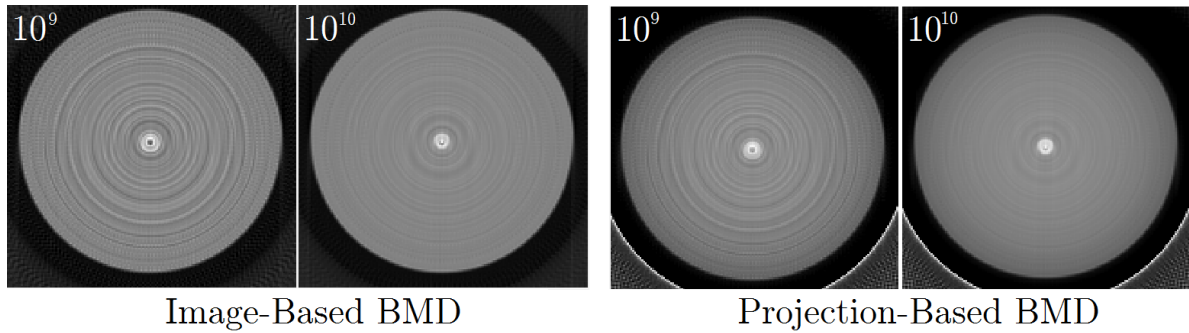


Figure A-10. Monoenergetic images for both number histories and both BMD methods. The images were reconstructed for 80 keV. L/W: $-200 \text{ HU}/1000 \text{ HU}$ for the Projection-Based BMD method, and $-64 \text{ HU}/1049 \text{ HU}$ the Image-Based BMD method.

Table A-3 presents the standard deviation computed in the monoenergetic images of Figure A-10 using the ROI defined as background in Figure A-1. The monoenergetic images obtained for 10^{10} histories presented the lower noise. The noise obtained from both methods are almost equal, but the Image-Based images presented noise a little lower than the Projection-Based images.

Table A-3. Estimative of the noise in the monoenergetic images.

	Image-Based		Projection-Based	
	10^9	10^{10}	10^9	10^{10}
σ_{BG} [HU]	81	40	84	41

It is possible to conclude that the number of histories improves the image definition of the monoenergetic and the material concentration images (Figure A-8, Figure A-9 and Figure A-10). For the water phantom with the bone insert the method

that exhibited better material differentiation images was the Projection-Based BMD. The monoenergetic images obtained from both BMD methods present almost the same noise.

A.3 Uncertainties of CNR and SNR

The CNR is defined as equation (14). To estimate the uncertainty of CNR the relations presented in equations (A1) are used to obtain the equation (A2).

$$\text{If } z = \frac{x}{y}, \text{ then } \sigma_z = z \sqrt{\frac{\sigma_x^2}{x^2} + \frac{\sigma_y^2}{y^2}} \quad \text{If } z = x + y, \text{ then } \sigma_z^2 = \sigma_x^2 + \sigma_y^2 \quad (\text{A1})$$

$$\sigma_{CNR} = CNR \sqrt{\frac{\sigma_{\bar{x}_s}^2 + \sigma_{\bar{x}_{bg}}^2}{(\bar{x}_s - \bar{x}_{bg})^2} + \frac{\sigma_{\sigma_{bg}}^2}{\sigma_{bg}^2}} \quad (\text{A2})$$

The uncertainty of the noise of the background σ_{bg} is expressed as equation (A3) (Helene et al., 1991) where N_{bg} presents the number of pixels in the region defined as background.

$$\sigma_{\sigma_{bg}} = \frac{\sigma_{bg}}{\sqrt{2(N_{bg} - 1)}} \quad (\text{A3})$$

Then, the uncertainty of CNR was calculated using (A4).

$$\sigma_{CNR} = CNR \sqrt{\frac{\sigma_{\bar{x}_s}^2 + \sigma_{\bar{x}_{bg}}^2}{(\bar{x}_s - \bar{x}_{bg})^2} + \frac{1}{2(N_{bg} - 1)}} \quad (\text{A4})$$

The SNR was calculated as in equation (15). It is possible to simplify (15) as (A5) where N represents the number of pixels in the ROI defined for measure the signal as in Figure 10.

$$SNR = \frac{N(\bar{x}_s - \bar{x}_{bg})}{\sigma_{bg}} \quad (\text{A5})$$

Following similar steps as the presented for the CNR the uncertainty of SNR is presented in equation (A6). Again N_{bg} presents the number of pixels in the region defined as background.

$$\sigma_{SNR} = SNR \sqrt{\frac{\sigma_{\bar{x}_s}^2 + \sigma_{\bar{x}_{bg}}^2}{(\bar{x}_s - \bar{x}_{bg})^2} + \frac{1}{2(N_{bg} - 1)}} \quad (\text{A6})$$

B. CHEMICAL FEATURES OF THE SIMULATED MATERIALS.

This appendix presents the composition features of the materials used to fill the phantoms presented in this text. Section B.1 describes the iodine inserts of the phantom mentioned in sections 2.2 and 3.2. Sections B.2 present the composition of the calcium and iodine inserts of the phantom mentioned in sections 2.3 and 3.3.

B.1 Simulated water-iodine phantom

As mentioned in section 2.2 the simulated phantom shown in Figure 27, contained inserts containing iodine concentrations. The simulated contrast agent material for iodine was the Ultravist® 300 (Bayer, 2012). This section contains two parts, the first one explains the composition assume for the Ultravist® 300 and the second explains the composition of the materials of the phantom of Figure 27.

Iopromide

Ultravist® 300 contains $C_{18}H_{24}I_3N_3O_8$ (iopromide) as active ingredient, each ml(cm^3) of Ultravist® 300 contains 623 mg of iopromide and a 20° C has a density of 1.33 g/ cm^3 (Bayer, 2012). The following assumptions were taken:

- As the density of Ultravist® is 1.33 g/ cm^3 it was assumed that 0.623 g of each cm^3 were iopromide and the rest, 0.707g, water.
- The molar mass of iopromide is 791.11 g/mol and the molar mass of water 18.02 g/mol. Then, the total mass of each element in a cm^3 of Ultravist® can be calculated using the following formula:

$$T_x = \frac{M_{Xiopromide}}{M_{Iopromide}} \times 0.623 \frac{g}{cm^3} + \frac{M_{Xwater}}{M_{Water}} \times 0.707 \frac{g}{cm^3} \quad (B1)$$

Where T_x represents the total mass of the element x in a cm^3 of Ultravist®, $M_{Xiopromide}$ and M_{Xwater} represent the molar mass of the element X in iopromide or water. I.e., M_{Xwater} corresponds to the multiplication of the number of atoms of the element X in water times the molecular mass of the element X. $M_{Xiopromide}$ is calculated in an equivalent way. $M_{Iopromide}$ and M_{Water} the molar masses of iopromide and water respectively previously mentioned.

Table B-1, presents the number of atoms of each element in water and iopromide, the molar mass of each element and T_X in the column “Elemental mass per $\text{cm}^3(\text{g})$ ”. It is possible to observe in bold font the total mas of iodine per cm^3 is 0.3 g (300 mg), it coincides with the Ultravist® 300 in which each ml of solution contained the 300 mg of iodine. Table B-1 also presents the sum of the “Elemental mass per $\text{cm}^3(\text{g})$ ” such sum coincides with the nominal density of the Ultravist® 300, $1.33 \text{ g}/\text{cm}^3$.

Table B-1 The assumed chemical composition of pure Ultravist® 300. The Iopromide and water quantities columns present the number of atoms of the element in water or iopromide

Element	Iopromide quantity	Water quantity	Molar mass(g/mol)	Elemental mass in a $\text{cm}^3(\text{g})$
C	18	0	12.01	0.170
H	24	2	1.01	0.098
I	3	0	126.90	0.300
N	3	0	14.01	0.033
O	8	1	15.99	0.729
Total	—	—	—	1.33

Composition of materials of the iodine-water phantom

Three volume solutions of Ultravist® 300 were simulated I-45 (15% of Ultravist® 300), I-30 (10% of Ultravist® 300) and I-15 (5% of Ultravist® 300). The assumed solute was water. The percentage in braces represented volume percentage, as an example, one ml of the solution of I-30 will contain 10% of volume of Ultravist® 300, it will contain 0.1 ml of Ultravist® and 0.9 ml of water. The percentages of each element were calculated as presented in equation (B2). It shows the percentage of the element X (%X) present in a solution of 10% of Ultravist, T_X represents the elemental mass of such element in the Ultravist® 300 or water (as calculated in the previous section), and ρ the density. The percentages of each element for each solution are presented in Table B-2.

$$\% X = \frac{T_{X\text{Ultravist}} \times 0.1 + T_{X\text{water}} \times (1 - 0.1)}{\rho} \quad (\text{B2})$$

Table B-2. Element percentages for the solutions I-45, I-30 and I-15.

Element	Element Percentage (%)		
	I-45 solution	I-30 solution	I-15 solution
C	2.4	1.6	0.8
H	10.5	10.7	10.9
I	4.3	2.9	1.5
N	0.5	0.3	0.2
O	82.3	84.4	86.6

The density values of the I-45, I-30 and I-15 solutions were obtained as 1.050 g/cm³, 1.033 g/cm³ and 1.017 g/cm³ respectively. Along with the density, the element percentage shown in Table B-2 were used to simulate the materials presented in Figure 27. The iodine equivalent concentration of each insert can be calculated by multiplying the percentage iodine value (as number between 0 and 1) times the density. For example, the iodine concentration in the insert I-45 is: 0.043*1.050 g/cm³=45 mg/cm³. Then, the effective iodine concentration coincides with the number in the insert label. The inserts I-30 and I-15 have iodine concentration of 30 mg/cm³ and 15 mg/cm³ respectively.

B.2 Real phantom

This section describes the composition of the materials used in the phantoms shown in Figure 29 and in Table 8. These phantoms include two groups of materials, the ones representing iodine concentration and the ones representing calcium concentration.

In this case, the mixtures of iodine were obtained mixing Ultravist® 300 and saline solution. The saline solution is an aqueous solution of sodium chloride with a concentration of 9g/L (Farma, 2017). The concentration and percentages of each element were calculated in a similar way as described in the previous section.

The element concentrations and percentages are presented in Table B-3, the total concentration represents the density (sum of individual concentrations), density is found in the last row of the table in bold font. It is also possible to see the concentration of iodine in bold font, this is to show that the concentration of iodine coincides with the material label.

Table B-3. Element concentration and percentage for each iodine concentration.
Conc: Concentration, %: percentage.

Element	I 25 mg/ml		I 20 mg/ml		I 12.5 mg/ml		I 10 mg/ml	
	Conc. (g/cm ³)	%						
C	0.014	1.4	0.011	1.1	0.007	0.7	0.006	0.6
H	0.110	10.7	0.110	10.8	0.111	10.9	0.111	10.9
I	0.025	2.4	0.020	1.9	0.0125	1.2	0.010	1.0
N	0.003	0.3	0.002	0.2	0.001	0.1	0.001	0.1
O	0.871	84.4	0.873	85.1	0.877	86.2	0.879	86.5
Na	0.003	0.3	0.003	0.3	0.003	0.3	0.004	0.3
Cl	0.005	0.5	0.005	0.5	0.005	0.5	0.005	0.5
Total	1.032	100.0	1.026	100.0	1.018	100.0	1.015	100.0

The calcium inserts were prepared and simulated using Calcium carbonate (CaCO_3) following composition properties found in (Carbonates, 2015). The simulated content of CaCO_3 was 82.65% with 17.35% of MgCO_3 (Carbonates, 2015). The carbon black was assumed to be pure C as there was no information about its purity (Anastacio, 2017).

The process to obtain the percentage of the elements is different as the density was determined afterwards the mixture of the powders. In this case, quantities of each powder were mixed in controlled proportions and after that the percentage of each element was estimated using the known composition of each powder. Once the cavities were filled the density were determined using the mass and volume of the phantom cavities. The measured densities were 0.52 g/cm^3 for Ca 56 and 0.90 mg/cm^3 for Ca 163. The percentage of each element is presented in Table B-4. The mass concentration of calcium is obtained as the product of the density times the percentage associated with calcium in Table B-4.

Table B-4. Concentration and percentages per element for each calcium concentration.

Element	Ca 56 mg/ cm^3		Ca 163 mg/ cm^3	
	Conc. (g/cm^3)	%	Conc. (g/cm^3)	%
Ca	0.056	10.9	0.164	18.1
C	0.292	56.5	0.249	27.5
O	0.134	26.0	0.392	43.4
Mg	0.034	6.6	0.099	11.0
Total	0.52	100	0.90	100

C. T-TEST

T-test is a hypothesis test used to validate hypothesis taking into account the number of data used and the significance level (Helene & Vanin, 1991). It is assumed that data follow a Gaussian distribution.

The test is useful to compare the measured and the expected data. The objective is to formulate a statistical hypothesis to infer of their compatibility. Having a set of N data with mean \bar{x} , and standard deviation of the mean σ_m . The t random variable defined in equation (C1) has Student t-distribution function with N-1 degrees of freedom. With such Student t-distribution the hypothesis test is performed.

$$t = \frac{(\bar{x} - x_0)}{\sigma_m} \quad (C1)$$

In this work the t-test is used to infer the equivalence of values, then, the hypothesis considered here can be written as:

$$\text{Hypothesis: } x_0 = \bar{x} \text{ or as Hypothesis: } x_0 - \bar{x} = 0$$

If the hypothesis is true, the most probable values for t are close to zero. This work t-tests evaluate equivalence, so, the test performed were always two tailed. Then, the rule to be applied is to reject the hypothesis if |t| is big, and not reject it if |t| is small. How big |t| must be to reject the hypothesis is defined by the significance level and the degrees of freedom (Helene & Vanin, 1991). The significance level, the degrees of freedom, and the type of test (one or two tailed) define a critical value, t_{crit} . If the t value obtained from equation (C1) is greater than t_{crit} the hypothesis is rejected. The values of t_{crit} can be found in tables for different. Further information and examples can be found in (Helene & Vanin, 1991).

A slightly different approach is used when comparing two means which come from a different data sets with different number of elements. In this case, t is defined as presented in equation C2.

$$t = \frac{(\bar{x}_1 - \bar{x}_2)}{\sigma_{\bar{x}_1 - \bar{x}_2}} \quad (C2)$$

Where $\sigma_{\bar{x}_1 - \bar{x}_2}$ is defined as in equation C3, an estimative which include the standard deviation of both sets of data.

$$\sigma_{\bar{x}_1 - \bar{x}_2} = \sqrt{\sigma_1^2 + \sigma_2^2} \quad (\text{C3})$$

The number of degrees of freedom is estimated as in equation C3 (Helene & Vanin, 1991).

$$\nu = \frac{(\sigma_1^2 + \sigma_2^2)^2}{\frac{\sigma_1^4}{n_1 - 1} + \frac{\sigma_2^4}{n_2 - 1}} \quad (\text{C3})$$

The critical value of t , t_{crit} , must be interpolated for non-integer values of ν .

D. MONOENERGETIC IMAGES

In this section are presented the monoenergetic images used to obtain the CNR on the virtual monoenergetic images described in section 3.3.3.

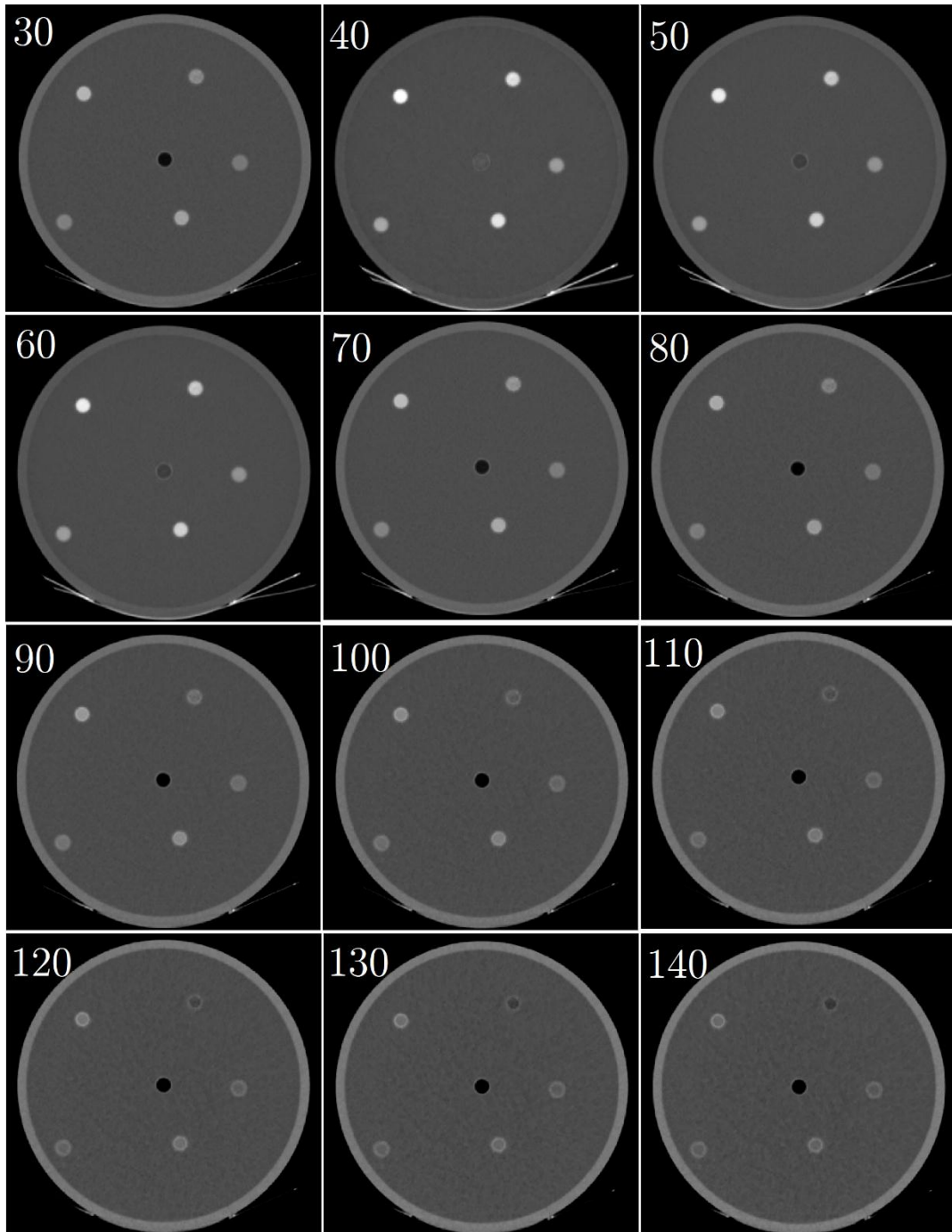


Figure D-1. Virtual monoenergetic images obtained from the real device. The images were used to measure the CNR in each cylinder. L/W: 100 HU /250 HU.

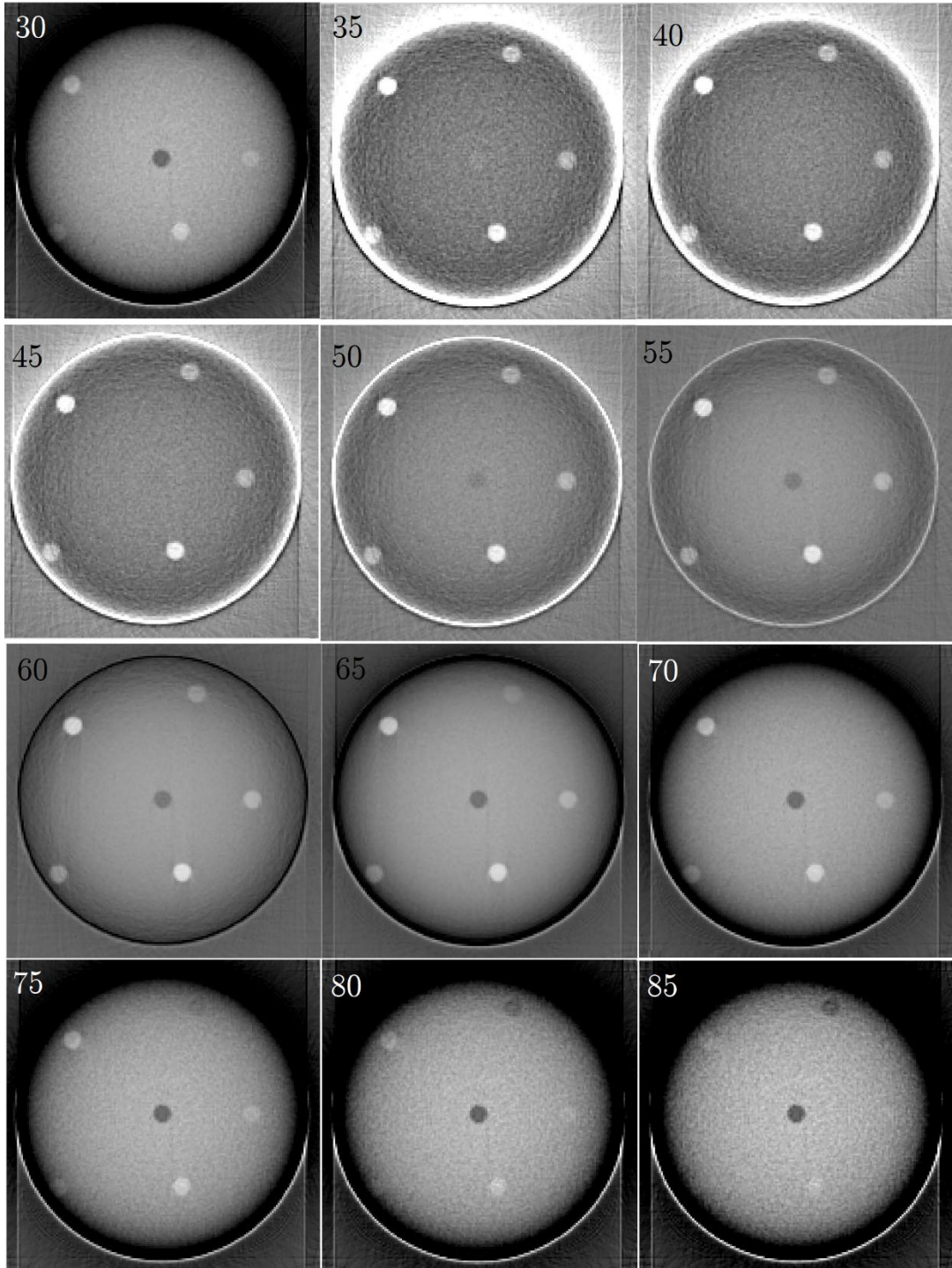


Figure D-2. Virtual monoenergetic images obtained from simulations. The images were used to measure the CNR in each cylinder. L/W: 250HU /7250 HU.